

**Design Modeling and Analysis of Compliant and Rigid-Body DNA Origami
Mechanisms**

DISSERTATION

Presented in Partial Fulfillment of the Requirements for the Degree Doctor of Philosophy
in the Graduate School of The Ohio State University

By

Lifeng Zhou

Graduate Program in Mechanical Engineering

The Ohio State University

2017

Dissertation Committee:

Dr. Hai-jun Su, Advisor

Dr. Carlos E. Castro, Co-Advisor

Dr. Jonathon W. Song

Dr. Hanna Cho

Copyright by

Lifeng Zhou

2017

Abstract

Scaffolded DNA origami is a recently emerging technology that allows the construction of complex nanostructures via molecular self-assembly driven by Watson and Crick base-pairing, i.e. A-T, C-G. In the past decade, this approach has been successfully used to construct complex 2D or 3D static structures. Complex dynamic DNA origami mechanisms (DOM) have been fabricated and can achieve 1D, 2D and 3D motions. However, thermal fluctuation can dramatically influence the performance of these dynamic DNA nanostructures in solution. The function of DOM always suffers significant variation due to the random motion of flexible joints constructed by flexible single-strand DNA (ssDNA) connections. Verification of these DOM depends heavily on the projection configurations of the nanostructures on two-dimensional transmission electron microscopy (TEM) images, which cannot always provide the accurate information of the actual configuration if the shape of the nanostructure is not planar. In addition, much more design and control of multiple degree-of-freedom is still difficult.

This research expanded scaffolded DNA origami nanotechnology to design dynamic nanomechanisms by following a design framework that parallels macroscopic compliant mechanism design. We refer these compliant DNA origami mechanisms as CDOM. The compliant components can be built by ssDNA connections or double-strand (dsDNA)

bundles with small bending stiffness, which can be easily realized within DNA origami. Firstly, Pseudo-rigid-body models were developed for the application of DNA nanostructures analysis. Then, a compliant hinge and a four-bar bistable mechanism were fabricated to demonstrate the design methodology. In addition, projection kinematics analysis was developed for obtaining the actual configurations of DNA origami nanomechanisms in space from the projection configurations on TEM images. This provides an efficient and economic approach for verification of dynamic DNA origami nanostructures. Finally, a waterbomb base was designed and fabricated by scaffolded DNA origami. Folding of the waterbomb base first demonstrated the control of multiple degree-of-freedom nanostructures. Moreover, higher-order dynamic nanostructures can be fabricated from the polymerization of folded waterbomb base.

Dedication

This document is dedicated to my family and my wife, Jie Xu.

Acknowledgments

During my PhD study and research, I got so many helps and supports from so many people. This is an important journey in my entire life and will have profound and lasting influence to my future career and life. I would like to express my sincere thanks to all of them at this moment.

I am always feeling lucky to have Prof. Hai-jun Su and Prof. Carlos E. Castro as my advisors since I came to The Ohio State University. Both of them provide invaluable supports and suggestions to my research. Prof. Hai-jun Su taught me how to modeling and solving kinematics problems of rigid-body or compliant mechanisms. Prof. Castro showed me how to design, conduct, verify and analyze experiments of DNA nanotechnology. Both of them showed me how to be a qualified teacher and scientist. In addition, thanks so much to my partner big Alex, he trained me to conduct DNA nanotechnology and together we shared so many exciting and disappoint moments during my research. Without their help support and help, I can't make this.

Thanks to my committee members, Dr. Jonathon Song and Dr. Hanna Cho, for their inspiration suggestions to my work. Dr. Jonathon Song has always provided timely help my research and study. This research is supported by the National Science Foundation under Grant No: CMMI-1235060, CMMI-1536862, Ahuja Endowed Graduate Fellowship and Presidential Fellowship.

Also, I would like to thank all of the members in Design innovation and simulation lab and Nanoengineering and biodesign lab. With their help and company, I really enjoy my study and life in OSU and Columbus. May our friendship last forever and Go buckeyes! In addition, thanks to the MAE and CMIF staff for all of their great support.

Special sincere thanks to my master thesis advisor Prof. Qizheng Liao and his wife for their irreplaceable and invaluable help and support for my study and life.

Finally, I always want to express my profound thanks and gratefulness to my parents, my wife and family for the many sacrifices they have made during my study. Their love provided me courage and confidence to pursue my own life and always gave me power to face the challenges in my life.

Vita

Jun 25 1987Born – Hunan, China

10/2005 – 06/2009B.S. Mechanical Engineering and
Automation, Beijing University of Posts and
Telecommunications

09/2009 – 04/2012M.S. Mechanical Engineering, Beijing
University of Posts and Telecommunications

08/2012 to presentPhD student, Department of Mechanical and
Aerospace Engineering, The Ohio State
University

Publications

- [1] **Zhou, L.**, Marras A. E., Castro, CE, Su, H., 2017, “Thick Panel Origami at Nanoscale Demonstrated by a Waterbomb Design”. *In preparation*.
- [2] Su, H.-J., and Castro, C. E., Marras, A. E., **Zhou, L.**, “The Kinematic Principle for Designing DNA Origami Mechanisms: Challenges and Opportunities”, Accepted, 2017.
- [3] Marras, A. E. and **Zhou, L.** and Kolliopoulos V., Su, H.-J, and Castro, C. E., 2016, “Directing folding pathways for multi-component DNA origami nanostructures with complex topology,” *New J. Phys.*, **18**(5).
- [4] **Zhou, L.**, Marras, A. E., Su, H.-J, and Castro, C. E., 2015, “Direct design of an energy landscape with bistable DNA origami mechanisms,” *Nano Lett.*, 15 (3), pp. 1815–1821.
- [5] Marras, A. E., **Zhou, L.**, Su, H.-J., and Castro, C. E., 2015, “Programmable

- motion of DNA origami mechanisms,” Proc. Natl. Acad. Sci., 112, pp. 713–718.
- [6] Castro, C. E., Su, H.-J., Marras, A. E., **Zhou, L.**, and Johnson, J., 2015, “Mechanical design of DNA nanostructures,” *Nanoscale*, 7, pp. 5913–5921.
- [7] **Zhou, L.**, Marras, A. E., Su, H.-J., and Castro, C. E., 2013, “DNA Origami Compliant Nanostructures with Tunable Mechanical Properties,” *ACS nano*, 8, pp. 27–34.
- [8] **Zhou L.**, Marras A. E., Castro, CE, Su, H., 2016, “Pseudorigid-Body Models of Compliant DNA Origami Mechanisms”. *ASME. J. Mechanisms Robotics*, 8(5):051013-051013-11. doi:10.1115/1.4032213.
- [9] Su, H.-J., and Castro, C. E., Marras, A. E., **Zhou, L.**, “The Kinematic Principle for Designing DNA Origami Mechanisms: Challenges and Opportunities”, The ASME 2015 International Design Engineering Technical Conferences & Computers and Information in Engineering Conference, Boston, MA, USA, August 2-5, 2015.
- [10] **Zhou, L.**, Marras, A. E., Castro, C. E. and Su, H., “Pseudo-rigid-body Models of Compliant DNA Origami Mechanisms”, The ASME 2015 International Design Engineering Technical Conferences & Computers and Information in Engineering Conference, Boston, MA, USA, August 2-5, 2015.
- [11] Su, H.-J., **Zhou L.** and Zhang, Y., "Mobility Analysis and Type Synthesis with Screw Theory: From Rigid Body Linkages to Compliant Mechanisms". In “Advances in Mechanisms, Robotics and Design Education and Research”. pp.67-81. *Mechanisms and Machine Science Series Vol.14*, Edited by: Vijay Kumar, James Schmedeler, S.V. Sreenivasan, Hai-Jun Su. Springer. 2013.

Fields of Study

Major Field: Mechanical Engineering

Table of Contents

Abstract	ii
Acknowledgments.....	v
Vita.....	vii
List of Tables	xiii
List of Figures	xv
Chapter 1: Introduction.....	1
1.1. Background	1
1.1.1. Nanomachines and nanorobots	2
1.1.2. DNA nanotechnology	4
1.1.3. DNA origami mechanisms (DOM).....	9
1.1.4. Compliant mechanism	10
1.1.5. Analysis of compliant mechanism	12
1.2. Compliant DNA origami nanomechanisms	13
1.3. Contributions.....	15
1.4. Organization of this thesis.....	16
Chapter 2: Mechanical Modeling of Compliant DNA Origami Mechanisms	18
2.1. Background.....	18
2.2. Design of compliant DNA origami joints and mechanisms	21
2.3. Mechanical models of ssDNA and dsDNA	24

2.4.	Pseudo-rigid-body models of compliant DNA links	28
2.5.	Conclusions	43
Chapter 3: DNA Origami Compliant Nanostructures with Tunable Mechanical Properties		44
3.1.	DNA origami compliant mechanisms	45
3.2.	Design of DNA origami compliant joint	47
3.3.	Experiment results	49
3.4.	Theoretical model of balanced bending and entropic tension	52
3.5.	Pseudo-rigid-body model of DNA origami compliant joint.....	67
3.6.	Materials and methods.....	70
3.7.	Summary.....	71
Chapter 4: Direct Design of an Energy Landscape with Bistable DNA Origami Mechanisms		73
4.1.	Background	74
4.2.	Design of Four-bar Bistable DNA Origami Mechanism	76
4.3.	Experiment results.....	80
4.3.1.	Initial data	80
4.3.2.	Actuation analysis.....	84
4.4.	Modeling analysis	90
4.5.	Materials and methods	108
4.5.1.	Structure purification and imaging	108
4.5.2.	DNA displacement actuation	109
4.6.	Summary and discussion	109
Chapter 5: Projection Kinematic Analysis of DNA Origami Mechanisms Based on a Two-Dimensional TEM Image		112

5.1.	Background	113
5.2.	Projection analysis of kinematic joints.....	116
5.2.1.	Revolute joint.....	118
5.2.2.	Prismatic joint.....	123
5.2.3.	Cylindrical joint	125
5.2.4.	Spherical joint.....	125
5.3.	Projection kinematics of planar mechanisms.....	129
5.3.1.	Planar four-bar linkage	129
5.3.2.	Planar five-bar linkage.....	136
5.4.	Algorithm of the projection kinematics analysis.....	140
5.5.	Application on DNA origami nanomechanisms	141
5.5.1.	Application to the DNA origami quasi universal joint TEM image analysis 143	
5.5.2.	Application of projection kinematics analysis on the DNA origami Bennett linkage 147	
5.6.	Summary and discussion.....	152
Chapter 6: Origami Inspired Design of Reconfigurable Nanostructures with DNA		
	Origami	154
6.1.	Background and motivation	154
6.2.	The modeling and analysis of the waterbomb base.....	159
6.2.1.	Kinematic analysis	159
6.2.2.	Projection kinematics analysis	162
6.3.	Fabrication of the waterbomb base	164
6.4.	Actuation of the waterbomb base.....	166
6.4.1.	Triangular configuration folding at room temperature	167

6.4.2.	Rectangular configuration folding at room temperature.....	170
6.4.3.	Final compact configuration folding at room temperature	172
6.5.	Actuation of the waterbomb base by thermal annealing.....	176
6.6.	Higher-order DNA origami structures based on polymerization.....	177
6.7.	Experimental procedure	179
6.8.	Summary and conclusion	181
Chapter 7: Conclusions and Future Work.....		182
7.1.	Conclusions	182
7.2.	Future work	185
References.....		188

List of Tables

Table 2.1: Basic parameters for Pseudo-rigid-body model.	31
Table 3.1: Design parameters of the ssDNA springs.	48
Table 3.2: Basic parameters used in the analytical model.	59
Table 3.3: Equilibrium angles obtained from experiment and analytical model.	60
Table 4.1: Summary of experimental angle distributions and model.	90
Table 5.1: Initial, rotated, projected and measured points that define the structure of the revolute joint	119
Table 5.2: Numerical example for projection kinematic analysis of revolute joints	120
Table 5.3: Numerical example for projection kinematic analysis of a prismatic joint ...	125
Table 5.4: Initial, rotated, projected and measured points that define the structure of the spherical joint.....	127
Table 5.5: Numerical example for projection kinematics analysis of a spherical joint ..	127
Table 5.6: Initial, rotated, projected and measured points that define the structure of planar four-bar linkage.....	131
Table 5.7: Equations and solutions of four kinds of projection kinematic analysis for the four-bar linkage.....	134
Table 5.8: Numerical example of projection kinematic analysis of a four-bar linkage..	135
Table 5.9: Solutions of case 1, 2, 3 and 4 of the projection kinematics analysis of planar four-bar linkage. The values of $(\theta_{01}, \theta_{02}, \alpha, \beta)$ is shown at the bottom of each 3D subfigure.	135
Table 5.10: Initial, rotated, projected and measured points that define the structure of planar five-bar linkage	137

Table 5.11: Numerical example of projection kinematics analysis of a five-bar linkage	139
Table 5.12: Initial, rotated, projected and measured points that define the structure of quasi universal joint	145
Table 5.13: Projection kinematic analysis of a DNA origami quasi universal joint	146
Table 5.14: Initial, rotated, projected and measured points that define the structure of DNA origami Bennett linkage	149
Table 5.15: Measurements, projection kinematics solution and projection results from the model, errors of link lengths between the experiment measurements and projection kinematics analysis of DNA origami Bennett linkage (examples 1, 2, and 3 corresponding to the three examples in Figure 5.17 from top to bottom respectively), unit for length: nm.	151
Table 6.1: Detailed design parameters of joints	157
Table 6.2: Detailed Denavit–Hartenberg parameters and obtained screws for all joints	161

List of Figures

Figure 1.1: A molecular robot by Lund et al.[1].....	1
Figure 1.2: Scaffolded DNA origami. (a) Geometrical parameters of single dsDNA and two parallel dsDNA connected with two crossovers [20]. (b) Sketch of the scaffolded DNA origami: the single-stranded scaffold is folded by the ssDNA strands based on the base-pairing (A-T, G-C). (c) An example of the blueprint export from caDNAno: the scaffold (blue line) is folded and hold by a bunch of staples (color ones).	5
Figure 1.3: Examples of 2D and 3D DNA origami nanostructures.[19,20,22,23].	8
Figure 1.4: DNA origami mechanisms and machines (DOM).[31].....	9
Figure 1.5: Examples of compliant mechanisms, a clamper (left) and a compliant hinge (right).	11
Figure 1.6: Pseudo-Rigid-Body model of a complaint cantilever beam.....	12
Figure 2.1: (a) The cylinder model of single dsDNA helix. (b) Two parallel dsDNA helices.	21
Figure 2.2: Basic elements for the joints design of CDOM.....	23
Figure 2.3: Design links and mechanisms. (a) Rigid parts with different cross sections. (b) A four-bar bistable mechanism. (c) Expandable mechanism.	24
Figure 2.4: Sketch of single polymer.....	25
Figure 2.5: The cross section of a bundle of six dsDNA helices, each circle represents a dsDNA helix.	27
Figure 2.6: PRBM for cantilever beam with a non-rigid-fixed end.....	29
Figure 2.7: Comparison between PRBM (red dots or lines) and beam model (blue dots or lines) for non-rigid-fixed end cantilever beam.	32
Figure 2.8: Three segments cantilever beam.	33

Figure 2.9: One revolute joint PRBM for the three segment cantilever beam. (a) Sketch of the PRBM. (b) Test of different segment length ratios. (c) Comparison of end tip position and energy between PRBM and beam model.	36
Figure 2.10: PRB-3R model for non-uniform cross section beam. (a) Sketch of the model. (b) Test of different segment length ratios. (c, d, e) Comparisons of end tip position, end tip angle, energy and their relative errors and average errors.	39
Figure 2.11: Test the PRB-3R model for different bending stiffness of different segment. (a) Sketch of the model. (b) Test of different segment length ratios. (c, d, e) Comparisons between PRB-3R model and beam model.	40
Figure 2.12: PRB-3R model applied on the non-rigid-fixed multi-cross section cantilever beam. (a) Sketch of the model. (b, c) End tip position, stored energy calculated by the PRB-3R model and the beam model.	43
Figure 3.1: 3D model and function of DNA origami compliant nanostructure.	47
Figure 3.2: TEM experimental results. (a) Gel electrophoresis reveals geometric differences between design versions. (b to f) TEM images of the five design versions. Scale bars, 50nm.	50
Figure 3.3: Angle measurement error analysis.	50
Figure 3.4: Conformational analysis of the TEM experiment results. (a to e) Typical particles and histogram distribution of versions with 0, 11, 32, 53, and 74 bases in the ssDNA springs. All scale bars are 20 nm.	51
Figure 3.5: Analysis based on the Bernoulli-Euler beam model and WLC model. (a) The cylinder model (b) the deformed compliant joint (c) right half of the compliant joint (d) force needed to bend the joint.	53
Figure 3.6: Theoretical model of the compliant joint. (a) Beam model of the curved segment. (b) Energy stored in the 6-helix layer (red). (c) The total energy of the compliant joint. (d) Boltzmann distribution of the thermal fluctuations in angle.	61
Figure 3.7: Theoretical model captures angular distribution. (a) The analytical model and (b) the trend of increasing width, characterized by the FWHM. (c) Analytical energy landscape captures the asymmetry of the experimental distributions.	62
Figure 3.8: Designing joint angle and stiffness with the theoretical model. (a) Predict the width of the joint angle distribution and (b) control the equilibrium angle.	65
Figure 3.9: Sensitivity analysis. (a) the length of a ssDNA base, (b) the persistence length of ssDNA, (c) the length of a dsDNA base pair, (d) the persistence length of dsDNA and (e) the offset distance e.	66

Figure 3.10: PRBM of the CDOM hinge joint.	67
Figure 3.11: (a) TEM images of CDOM hinge joint and (b) comparison of experiment and model results, scale bar = 20 nm.	69
Figure 4.1: A bistable beam and a bistable compliant four-bar mechanism.	77
Figure 4.2: Design sketch and stable equilibrium configurations of the bistable nanomechanism. (a) 3D model. (b) Energy variation of this nanomechanism.	78
Figure 4.3: Gel purification and TEM images.	81
Figure 4.4: TEM experimental results and analysis. (a) Typical TEM images, scale bars are 50 nm. (b) Conformational distribution.	82
Figure 4.5: Actuation with DNA strand inputs.	85
Figure 4.6: Reversible actuation of bistable nanomechanism. (a) Actuation process. (b) Conformational distributions. Scale bars = 100 nm.	86
Figure 4.7: Effects of temperature on the reverse actuation. (a) Initial TEM image and angle distribution. (b) Closed configuration actuation. (c) Re-opened experiment at room temperature. (d) Re-opened experiment at 32°C. (e) Re-opened experiment at 37°C.	88
Figure 4.8: Measuring the stiffness of the fixed joint between the compliant and frame links. (a) Sketch of the fixed joint. (b) The 3D sketch of the model used to measure the fixed joint stiffness, scale bars are 100 nm.	91
Figure 4.9: The PRB model for the bistable mechanism. (a) Deformed shape of a cantilevered beam. (b) The PRBM for a cantilever beam (c) PRB-1R model of bistable compliant nano-mechanism, dimension unit: nm. (d) Simplified model.	93
Figure 4.10: Comparison of the energy landscapes obtained from experiment and theoretical model.	96
Figure 4.11: Variation of PRB parameters and sensitivity of the potential energy landscape of the theoretical model.	98
Figure 4.12: Comparison between theoretical PRB model and experimental results for the geometry of the unstable position.	99
Figure 4.13: Modified model of the bistable nano-mechanism. (a) Dimension details of the modified model. Unit is nm. (b) Simplified modified model. (c) Comparison of energy landscapes.	100

Figure 4.14: Tune the stiffness of the bistable mechanisms. (a) Add more connections at the right angle junction. (b) Modify the shape of the compliant link.	103
Figure 4.15: Conformational distribution analysis during depositing and drying process.	106
Figure 5.1: Kinematic parameters of revolute, prismatic, cylindrical and spherical joints (from left to right) are 3D (top) in nature.	117
Figure 5.2: Projection of a revolute joint formed by two links.....	118
Figure 5.3: Configuration solutions of the projection kinematic analysis of a revolute joint.	121
Figure 5.4: Explanation of symmetrical (mirrored) configurations distinguished by a designed feature (red box on the purple link). (a) Positive and negative revolute joint angles. (b) Symmetrical configurations of planer four-bar linkage.....	122
Figure 5.5: Projection kinematic analysis of prismatic joint and a numerical example. (a). The coordinate frame of prismatic joint. (b). Sketch of the projection of prismatic joint. (c). Projected configuration of the prismatic joint. (d). Solutions of a numerical example of projection kinematics analysis of prismatic joint.	124
Figure 5.6: Projection kinematics analysis of spherical joint. (a). The local coordinate frame of spherical joint. (b). Sketch of the projection of spherical joint. (c). Projected configuration of the spherical joint.	126
Figure 5.7: Configuration solutions of the projection kinematic analysis of a spherical joint. θ_{01} , β and $\alpha+\phi_0$ for each solution is shown under the figure as $(\theta_{01}, \beta, \alpha+\phi_0)$	128
Figure 5.8: Projection kinematic analysis of a planar four-bar linkage. (a). The local coordinate frame of planar four-bar linkage. (b). The original and projected planar four-bar linkage. (c). The projected configuration.....	130
Figure 5.9: Projection kinematic analysis of a planar five-bar linkage. (a) The local coordinate frame is defined. (b) The planar five-bar linkage in space and its projection onto xy plane. (c) The detailed projected configuration.	137
Figure 5.10: Solutions of the projection kinematics analysis of planar five-bar linkage. The $(\theta_{01}, \theta_{02}, \theta_{03}, \alpha, \beta)$ for each solution is shown at the bottom of each subfigure.....	139
Figure 5.11: Measurements on TEM image.	142
Figure 5.12: Dimension of the universal joint, unit: nm.....	143

Figure 5.13: Projection kinematics analysis of quasi universal joint. (a, b, c) are the local coordinate frame, sketch of the projection configuration and projected configuration of the quasi universal joint respectively.	144
Figure 5.14: Projection kinematics analysis of the quasi universal joint based on the TEM image. (a) A typical TEM image of the DNA origami universal joint. (b) The projection information that can be measured from the TEM image. (c) 3D projection solution of the TEM image sample. (d) The detailed projected configuration of the solution.	146
Figure 5.15: Dimension of the Bennett linkage.	147
Figure 5.16: Projection kinematics analysis of the Bennett linkage. (a, b and c) are the local coordinate frame, sketch of the projection configuration and projected configuration of the Bennett linkage respectively.	148
Figure 5.17: Analysis of the projection kinematic of the Bennett linkage based on the TEM image.(a) Typical TEM images of the Bennett linkage. (b) The projection information measured from the TEM image. (c) 3D projection solution of the TEM image sample. (d) The detailed projected configuration of the solution.	150
Figure 6.1: Design procedure. (A) Waterbomb base designed by a single paper. (B) Thick panel design of Waterbomb base. (C) Modified waterbomb base design with a square portion was removed at center. (D) Cylinder model of our waterbomb base design. (E) Dimensions and cross section of the waterbomb base.	155
Figure 6.2: Construction of joints. Detailed length for each connection can be found in Table 6.1.	157
Figure 6.3: 3D folding design of waterbomb base. (A) The waterbomb base folded by a single thin paper and its square, triangle, rectangle, intermediate, compact configurations (from left to right). (B) Thick panel Waterbomb base design. (C) Cylinder model of DNA origami Waterbomb base.	158
Figure 6.4: Coordinate frames and parameters for kinematics analysis.	160
Figure 6.5: Projection kinematics analysis. (A) Top view of the waterbomb base. (B) Bottom view of the waterbomb base. (C) Relationship between the real joint angle θ_1 and projection joint angle $\bar{\theta}_1$	163
Figure 6.6: Experiment of waterbomb base. (A) Agarose gel electrophoresis purification image. (B) Transformation paths among the square, triangle, rectangle and compact configurations. (C) A transmission electron microscopy images and represents of folded configurations, scale bar: 100 nm. (D) Projection kinematics analysis (cite MMT paper) and equilibrium configuration. Black line is the theoretical relationship between projection angles $\bar{\theta}_1$ and $\bar{\theta}_2$, red dots are the measured projection information from TEM	

images and five typical TEM particles are shown. The distribution of the measured projection angle $\bar{\theta}_1$ is shown at the right bottom, and the equilibrium configuration is pointed out at the highest probability position.....	164
Figure 6.7: 3D cylindrical model of waterbomb base and its transformations.....	166
Figure 6.8: Triangle configurations actuation of waterbomb base.	168
Figure 6.9: Rectangle configuration actuation of waterbomb base.	171
Figure 6.10: Final folded configuration actuation of waterbomb base.....	173
Figure 6.11: Folds of waterbomb base by thermal annealing control. (A) Folding of different configurations. (B) Obtain square configuration by increasing the magnum concentration and a TEM image shows the result. (C) Gel purification image of the annealing controlled folding of square, triangular, rectangular and compact configuration. (D, E, F, G, H) TEM images of the folded square, triangle, rectangle and compact configurations. Scale bars: 100 nm.....	176
Figure 6.12: Higher-order nanostructures based on waterbomb base. (A) Polymerization based on the folded compact configuration along its lateral sides. Theoretically, straight filament can be obtained if no clearances exist and curved filament or even circular structure can be achieved if the clearances introduced by the design are taken into account, a circular structure has nine folded waterbomb bases is shown as an example. TEM images show the examples of linear, circular and curved structures obtained in the polymerization. (B) TEM images show the reopen example of the polymerized structures based on folded configuration. (C) Polymerization along the normal direction of lateral surface based on square configuration. Scale bars: 100 nm.	178

Chapter 1: Introduction

1.1. Background

Nanotechnology opened the door of the world at the nanoscale, through which humans can visualize, inspect, construct, and manipulate molecules and atoms. Even the direct manipulation of individual atoms was realized at the end of last century, but the technology used to achieve this was very complex and expensive. It is imperative and worthwhile to develop nanotools to conduct the work at nanoscale, such as atomic rearrangement, nanoparticle delivery and nanomanipulator actuation.

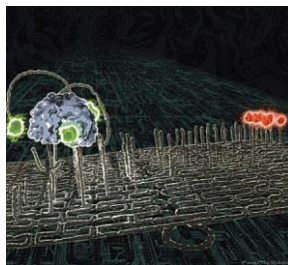


Figure 1.1: A molecular robot by Lund et al.[1]

The design and fabrication of nanomachines or nanorobot is one of the greatest scientific and technological challenges of the near to medium term future [2]. The ability to create and control nanorobots will inspire creation of new technologies and bring enormous welfare to human. Figure 1.1 shows a nanorobot built by protein and DNA molecules and it can follow the planned path on a track sheet built with DNA. As the booming of nanotechnology, engineering design is placed to a more and more important position because nanoscale devices with much more complex operations and multiple-functions are urged by necessitated applications, such as targeted drug delivery, controlled drug release and nanoparticles fabrication.

1.1.1. Nanomachines and nanorobots

Mechanisms and machines are the devices that can transmit force, motion or energy from the input joystick to the output effector through the intermediate components [3]. Usually, they consist of several links connected by kinematical joints, such as revolute, prismatic and spherical joints. The design and fabrication face huge challenges as the size of machine goes to nanoscale, but the abundant experience accumulated in macroscopic machine design can still provide plentiful valuable and feasible experiences for the nanomechanisms and nanomachines design. In recently years, kinds of protein are chosen by researchers to develop nanomachines. Proteins always consist of a bunch of amino acids whose properties have been investigated in detail, such as the stiffness, folding and unfolding states, stretching behavior, and degradation [4–6]. The polypeptide chain structure promises the stability of protein, which increases the probability of success on fabricating nanostructures. Here, it is intuitive for us to analyze the entire protein by a

chain model which uses the rigid link or part to represent the amino and revolute or hinge joint to represent the connection between the amino acids. Chirikjian and co-workers explained the folding and unfolding of proteins through a statistical kinematics approach [4]. In addition, Kazerounian applied the kinematic linkage model on the protein structure and developed a Matlab program named ProtoFold for predicting protein kinematics . The design and fabrication of bio-nanorobots with proteins and DNA was also on board through the effort of Mavroidis et al.[2]. Their research showed that many biological elements, such as kinesin, RNA polymerase, myosin, dynein, adenosine triphosphate (ATP) synthase, and DNA can function as nanoscale linear, oscillatory or rotary motors.

Recently, several hybrid protein-DNA nanomachines with functional motion had been achieved. For example, Lund et al. designed a molecular walker, shown in Figure 1.1, with three legs comprised by three individual dsDNA helices extending from a protein core [1]. Single-stranded overhangs were placed on the dsDNA legs and the corresponding complementary ssDNA overhangs were placed on the substrate. The “walk” was driven by thermal fluctuation while the ssDNA overhangs bind and release with the ssDNA strands on the substrate. Directionality was imposed by enzymatically disable the overhangs on the trajectory after the legs moving to the next step. These examples provide a promising proof-of-principle for nanoscale robot that can be controlled to finish prescribed motions and transports. However, they are still far away from the robot in macroscopic world that can be programmed and controlled to finish complex tasks automatically. In addition, the structures of these nanorobots are very

simple and their applications are greatly limited because many of them can only finish single task, such as simple rotation and translation [7–9].

1.1.2. DNA nanotechnology

Except the protein, scientists also pay lots of attention to utilize DNA as basic element to build biomaterials and nanostructures because DNA has a more concise and stable structure [10]. In addition, the DNA strand is constructed by four bases, adenine (A), thymine (T), guanine (G), and cytosine (C), while proteins are always constructed by a bunch of amino acids which have multitude of complex interactions that are difficult to quantify [11]. In addition, scientists have mastered and commercialized the artificial synthesis of arbitrary DNA polymers, which provides infinite possibility for the nanostructure and nanorobot designed with DNA. On the other hand, DNA has the ability of self-assembly based on the Watson and Crick base pairing principle, A-T & G-C. During the growing of cell, DNA can duplicate and unzip and zip to express the gene to make RNA, and RNA can unzip and zip to make proteins. Most of the complex biology activities are controlled by DNA molecules, which shows us that DNA is not only a very promising material for designing nanomachine or nanorobot, but the self-assembly property of DNA may also be the most practical approach for tuning and controlling of nanostructures.

The initial structural DNA nanotechnology was found by Nadrian Seeman in 1980's and 90's [12,13]. Although the majority of DNA nanostructure applications utilize objects with static geometry, important strides have been made to design dynamic DNA devices (i.e. DNA nanomachines). Early DNA nanomachines [14,15] involved

configurations of DNA strands that could be triggered to undergo conformational changes, usually via DNA strand displacement [16–18], to achieve, for example rotational or translational motion or even measure molecular binding energies [15]. Recently, a new type of DNA nanotechnology called scaffolded DNA origami has developed and it enabled the construction of nanostructures with unprecedented 2D or 3D structural complexity by self-assembly [19–22].

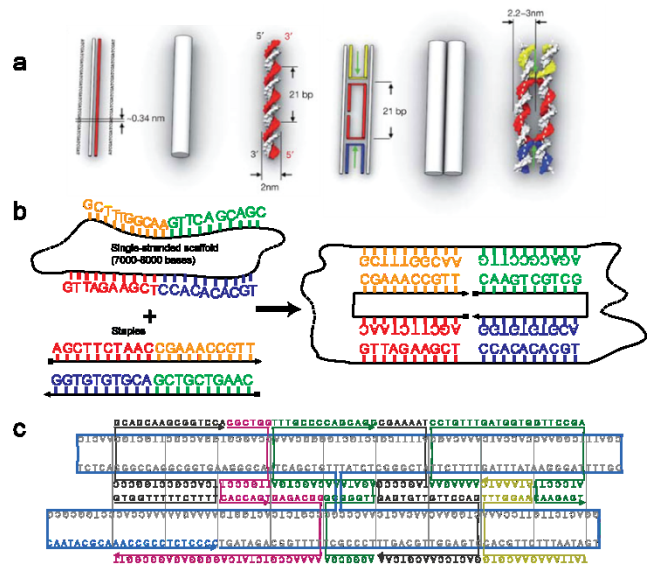


Figure 1.2: Scaffolded DNA origami. (a) Geometrical parameters of single dsDNA and two parallel dsDNA connected with two crossovers [20]. (b) Sketch of the scaffolded DNA origami: the single-stranded scaffold is folded by the ssDNA strands based on the base-pairing (A-T, G-C). (c) An example of the blueprint export from caDNAno: the scaffold (blue line) is folded and hold by a bunch of staples (color ones).

Scaffolded DNA origami is a bottom-up self-assembly fabrication method which can be explained concisely by Figure 1.2. Single dsDNA strand consists of two ssDNA strands

coiled into double helix structure by following the Watson-Crick base-pairing rules, A-T and G-C. From the top to the bottom, Figure 1.2(a), one ssDNA strand starts from the 5' end to the 3' end and the complementary ssDNA strand starts from the 3' end to the 5' end. Single dsDNA has a diameter close to 2~2.5 nm and the length of one base pair (bp) is about 3.4nm. The helix pitch of single dsDNA is 21 base-pair (bp). Usually, during the conception design, dsDNA can be presented by a single uniform cylinder with a diameter equal to 2-2.5 nm. When two dsDNA strands are arranged parallel together, the ssDNA strand on one dsDNA strand can routing to the other dsDNA strand through the tangent positions where their rotation directions are coincident. This is the key feature of the DNA origami, and the position that has the ssDNA strands span on two dsDNA strands is called crossover. Based on this, the scaffolded DNA origami is driven by DNA base-pairing between a long (~7000-8000 bases) single-stranded DNA (ssDNA) named “scaffold” and a bunch of shorter (~30-50 bases) ssDNA named “staple” strands (Figure 1.2(b)). The sequence of the scaffold has been identified and the popular method to obtain the scaffold is extracting from the M13MP18 bacteriophage virus genome [22]. The sequences of the staples are designed to be piece-wise complementary to sections of the scaffold that may be distant in primary sequence. That is, one staple strand may bind separate sections of the scaffold that may be several thousand bases away. All of the crossovers on the complementary ssDNA can be figured out by following the helix rotation of the dsDNA. Usually, more crossovers between adjacent dsDNA strands, more stable and stiffer the structure will be. When all of the staples and scaffold are mixed at specialized concentration ratio in buffer, the staples will bind to the scaffold and force the

scaffold to fold to the pre-designed nanostructure. This process is also called as self-assembly folding and the entire experiment process is controlled by an optimized thermal ramp. As the folding progress, the staples zip to the scaffold and form double-stranded DNA (dsDNA) and finally the entire scaffold will be stabilized into close-packed bundles of dsDNA by the staples. Structures are designed so that these bundles arrange into the desired 3D structure. Then the complementary ssDNA strands can be figured out easily by following the sequence of the scaffold.

Figure 1.2(c) shows that how a bunch of ssDNA strands (color ones) is used to fold the entire scaffold (blue line) into a four dsDNA strands plate. Currently, several computer-aided design tools of DNA origami are available to facilitate the design process. The most popular one is caDNAno which provides a fast and flexible design optimization of DNA origami scaffold, staple routing and sequence determinations.

Usually, the scaffold is derived from the M13MP18 bacteriophage virus and staple oligos are ordered from a commercial supplier. Complete and detailed protocol of scaffolded DNA origami was presented by Castro et al [22]. Briefly, the concentration of scaffold used to folding is 10-20 nM and the concentration of the mixed staples is 10-fold excess of each staple. Then the self-assembly process will happen in a buffer containing 5mM TRIS, 1Mm EDTA, 5 mM NaCl, 20 mM MgCl₂ and be controlled by a thermal annealing ramp with initial heating to 65 °C and subsequent slow cooling down to 4 °C over a typical timescale of 2-5 days.

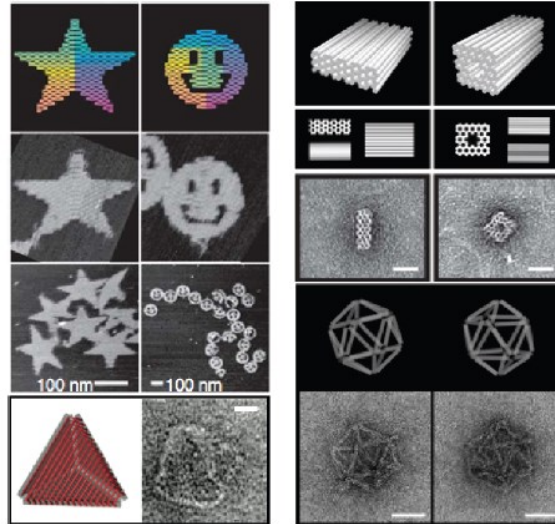


Figure 1.3: Examples of 2D and 3D DNA origami nanostructures.[19,20,22,23].

During the actual experiment, we need to screen the buffer conditions, especially the concentration of $MgCl_2$, and thermal annealing ramps to optimize self-assembly of the desired 3D nanostructures. Gel-electrophoresis is followed to purify the folded nanostructures and best folding condition can be figured out by evaluating the gel image. Then the purified samples will be deposited on the negative-stain grids of transmission electron microscopy (TEM). During the depositing process, the self-assembled nanostructures will drop and be absorbed to the surface of the grids. Finally, images will be taken under TEM. Lots of complex 2D and 3D nanostructures have been fabricated successfully by scaffolded DNA origami, such as stars and smiley faces[19], cuboid[20,24], tensegrity[25], sphere[26], polyhedron[27], and nanopores[28,29] (Figure 1.3).

1.1.3. DNA origami mechanisms (DOM)

DNA origami has been successfully used to design and fabricate hinge, prismatic, universal joints and furthermore, a spatial Bennett four-bar mechanism, a crank-slide mechanism and a scissor (Figure 1.4) [30,31].

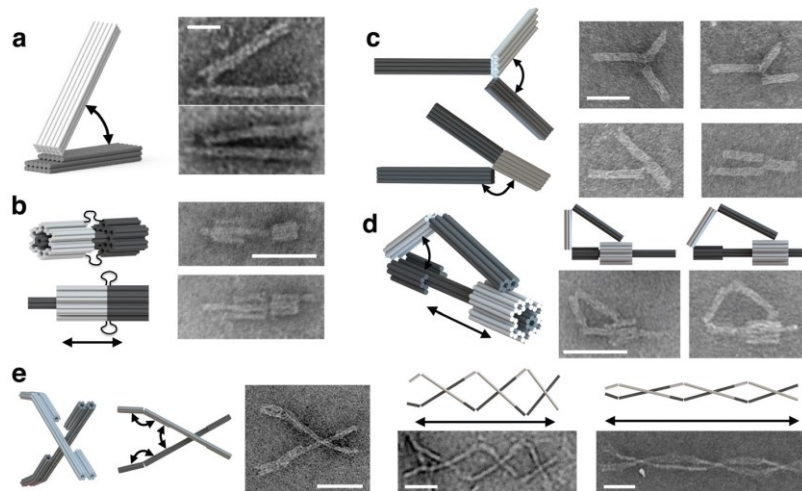


Figure 1.4: DNA origami mechanisms and machines (DOM).[31]

These joints and mechanisms were built by following the methodology of classic mechanical design and they are cataloged to the DNA origami mechanisms (DOM). These work proof that it is feasible to design mechanisms which can achieve 1D, 2D and 3D motions with DNA origami nanotechnology. Based on the achievement of DOM, more complex and powerful nanomachines can be built. But our current DOM is ad hoc, very inefficient and error-prone, especially can be dramatically influenced by the thermal

fluctuation. In addition, the control of the DOM is difficult due to the high flexibility of the joints.

Mechanical engineers also face great challenges when try to design and fabricate micromechanical devices. One challenge is the assembly of components can't be achieved according to the traditional machine assembly approach. Another big challenge is the micro devices can't suffer long time work and low fatigue bearing ability is a fatal weakness. However, compliant mechanism provides feasible and reliable ability to overcome these faults. Different from general machines, compliant mechanism can transmit energy, motion and forces by the deformation of the integrated compliant components. These compliant components always have smaller stiffness which can be achieved by using softer material or varying the geometry design parameters, such as a neck placed between two rigid segments. The design methodology of compliant mechanism has been successfully used on the micro-devices design and fabrication. It is worthy and valuable to apply the design and analysis methodology of compliant mechanism on the DNA origami mechanisms and machines.

1.1.4. Compliant mechanism

Different from rigid mechanism, compliant mechanism can transfer or transform the motion, force and energy through the deformation of the flexible elements that have relative smaller stiffness comparing with the other rigid portions [32–35]. Usually, mobility of compliant mechanism is obtained and determined by the range of deformation of the flexile elements that can made with either flexible material or the same material as the rigid portion but has small bending or torsional stiffness proving necessary

deformation in the needed motion direction. One advantage is that the entire compliant mechanism can be fabricated from a single sheet or a bulk material without assembling individual parts, which reduce the cost and increase the throughput. In addition, the accuracy of the compliant mechanism is pretty high because there is no clearance and lubrication problem caused by the assembly, which enable it as a significant choice for the design of high performance microscale and precision machines.

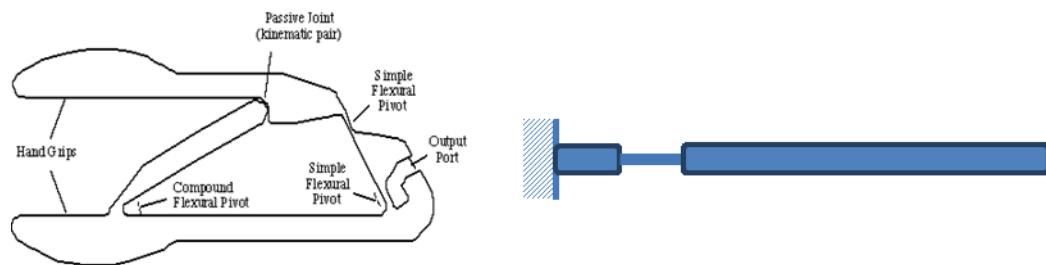


Figure 1.5: Examples of compliant mechanisms, a clammer (left) and a compliant hinge (right).

Figure 1.5(left) shows a clammer, an example of compliant mechanism. The entire clammer is fabricated from a single plastic sheet and its hinges or pivots have relative small bending stiffness about the rotation axes. A conception design of compliant hinge is shown in Figure 1.5(right). Most of deformation will exist at the hinge segment when a distal force is applied because the hinge segment has a much lower bending stiffness comparing with other portions.

These advantages of compliant mechanism can be integrated to the design and fabrication of microscale and even nanoscale machines, such as the microscale flipping robots, high precision XY nanopositioner [36]. In addition, compliant mechanisms also appear in the design of functional material that has special thermal expansion properties or negative Poisson's ratio [37].

1.1.5. Analysis of compliant mechanism

Due to the intrinsic nonlinear properties of deformation of flexible components, it is inefficiency to obtain the entire picture of the motion based on the stress and strain analysis or finite element simulation of compliant mechanism. Pseudo-rigid-body model (PRBM) provides a concise and easy-to-use approach for the kinematics and dynamics analysis of compliant mechanism [32–34]. Figure 1.6 shows the detailed PRB model application on a cantilever beam with a distal force.

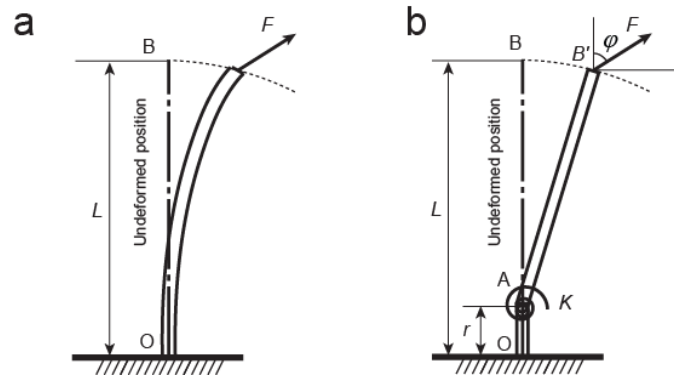


Figure 1.6: Pseudo-Rigid-Body model of a compliant cantilever beam.

Different from obtain solutions from the nonlinear deformation equations, PRBM treats the flexible component by torsional or linear springs and rigid component connected with traditional revolute or prismatic joint. The springs function as energy store element that is the same as the strain energy storage, the rigid component replace the flexible element and satisfy the geometry constraint and the joint provides the needed mobility for the mechanism. Then, traditional analysis methods for rigid body mechanisms can be applied on the compliant mechanism with acceptable accuracy.

Also, PRBM can be employed to analyze structures constructed by anisotropic materials, such as rubber and plastic[32]. As energy analysis is always important in biological system analysis, PRBM provides a useful approach for estimating the energy stored or transferred in structures of biological materials on which complex finite element methods or molecular simulations are always difficult to be conducted [35]. For instance, molecular simulation costs too much computation sources to obtain the deformation of DNA bundles under bending or twisting loads [38]. However, with the well-established relationship between persistence length and bending stiffness of DNA, PRBM can be applied to quantify the deformation and energy storage of DNA bundles [39–41].

1.2. Compliant DNA origami nanomechanisms

As mention previously, the development of scaffolded DNA origami enabled greater control over geometry and stiffness of nanostructure components, which has expanded the possibilities to design complex mechanical behavior. Furthermore, in recent years design and analysis tools have sped up the development DNA origami and enabled consideration of properties beyond geometry, such as stiffness, which play a critical role

in the function of many DNA origami nanodevices [42,43]. Prior work to design and quantify the mechanical behavior of DNA origami nanostructures has revealed that they exhibit mechanical deformations such as bending, stretching, and compression, similar to macroscopic structures [25,39,44]. Furthermore, some dynamic nanostructures fabricated with scaffolded DNA origami shown that it is feasible to design more complex nanorobots [24,45–47]. For example, Shown et al. designed a logic-gated nanorobot to delivery drugs to cells[45]. However, we can find that these designs are ad hoc and can only perform simple single task. More powerful, efficient and automatic nanorobots are still urgent needed. Because the fabrication process happens in the pre-set solution, it is still pretty difficult to obtain the fabrication result information from the solution directly. While the thermal fluctuation may dramatically influence the deformation of the flexible elements and the configuration of the entire nanomechanism, a big difference will be generated between the initial design and the experiment results.

In order to overcome those issues, this dissertation introduced the design of dynamic DNA origami nanostructures by employing the macroscopic compliant mechanism design. This work combined the methodology of macroscopic compliant mechanism design with scaffolded DNA origami to design and fabricate self-assembled DNA nanostructures which have tunable mechanical properties, robust performance and programmable motions. Different from the previous research and initial conception of DNA origami mechanisms (DOM), the introduction of compliant components to the DNA nanostructure design raises a novel concept which is termed compliant DNA origami mechanisms (CDOM). In this research, mechanical properties of compliant joint

and beam is been quantified and examples of compliant DNA origami mechanism have been fabricated.

1.3. Contributions

The overall theme of the research presented in this dissertation is to resemble concepts of compliant mechanism with the nanostructure design of DNA origami to solve the two challenges: quantification of mechanical properties and suppressing thermal fluctuations in solution. The design of CDOM will be considered as an assembly process of basic components, such as rigid links and compliant joints.

Three major achievements have been obtained: developed a design methodology for compliant joints, links and mechanisms with DNA origami, established the modeling and analysis procedure of CDOM based on PRB model and experiment verification and successfully demonstrated the application of paper origami design on DNA origami nanostructures. The accomplishments of this dissertation pave the road for designing much more complex nanomachines, broaden the applications of DNA nanostructures, provide comprehensive modelling and analysis procedures and establish detailed experiment protocols and efficient control and actuation approaches. Specially, the contributions of this thesis are summarized as follows.

1. PRB models are firstly used on the compliant mechanisms fabricated by DNA origami.
2. Nanoscale compliant hinges were fabricated by DNA origami and its mechanical properties can be tuned by adjusting its geometry design.

3. A nanoscale four-bar bistable mechanism was fabricated by DNA origami and it can be actuated to transfer between two stable configurations.
4. Projection kinematics analysis conception was established and applied on the analysis of DNA origami mechanisms based on two-dimensional transmission electron microscopy.
5. Paper origami methodology was successfully applied to design complex DNA origami mechanisms, which was demonstrated by the design and fabrication of Waterbomb base.

1.4. Organization of this thesis

The rest of this thesis is organized as follows.

Chapter 2 proposed detailed PRB models for compliant DNA origami mechanisms. With the parameters of DNA, such as diameter, single base length and persistence length, related to moment of inertia and Young's modulus, traditional material mechanic analysis can be applied on DNA nanostructures. And furthermore, much more accurate PRB models are provided for future analysis of DNA nanostructures.

Chapter 3 presents the design of DNA origami compliant hinges whose deformation can be controlled by the imbedded single strand DNA springs at the compliant segment. As the length of ssDNA springs shorten, the angle of the compliant hinges declines. In addition, Euler-Bernoulli beam equation was used to model the deformation and Worm-like chain model was employed to obtain the force introduced by the ssDNA springs. The models capture the experiments results well.

Chapter 4 introduced a four-bar bistable mechanism whose configurations can be controlled and transferred between the two stable positions. In addition, the energy landscape describing the transformation can be expected by the well-established PRB model. Controlled transformation between the two stable configurations is experimentally achieved via DNA displacement approach.

Chapter 5 established the concept of projection kinematics that analyzes nanoscale mechanisms or machines only based on two-dimensional images including electron microscopy and atomic force microscopy images. This analysis approach is built on kinematics analysis of the nanoscale mechanisms and their spatial transformations. It can be applied not only on DNA origami mechanisms, but also on macroscopic linkage analysis and control based on videos or pictures.

Chapter 6 introduced the design and fabrication of waterbomb base by DNA origami, which mimicked the methodology of paper origami. Waterbomb base is a complex dynamic DNA origami mechanism that has multiple configurations. Detailed kinematics model was presented. Multiple configurations were achieved by controlling the folding of corresponding joints via DNA strand displacement. In addition, several high-order nanostructures based on different configurations of waterbomb base were obtained.

Chapter 7 summarized all achievements and discussed the future directions of research about DNA origami mechanisms and machines. Moreover, potential and promising applications of dynamic DNA nanostructures were presented.

Chapter 2: Mechanical Modeling of Compliant DNA Origami Mechanisms

In this chapter, computational analysis of compliant DNA origami mechanisms (CDOM) is introduced and explained in detail. The rigid, compliant and flexible parts are constructed by bundles of many double-stranded DNA (dsDNA) helices, bundles of a few dsDNA helices or a single dsDNA helix, and single-stranded DNA (ssDNA) strands, respectively. Similar to its macroscopic counterparts, a CDOM generates its motion via deformation of at least one structural member. During the motion, strain energy is stored and released in the compliant components. Therefore, these CDOM have the advantage of suppressing thermal fluctuations due to the internal mechanical energy barrier for motion. Here, it is demonstrated that classic Pseudo-rigid-body (PRB) models for compliant mechanism can be employed to the analysis of these DNA origami nanomechanisms and can serve to guide the design and analysis method.

2.1. Background

DNA origami is a kind of bottom-up nanotechnology that uses DNA as material to create complex 3D nanostructures based on programming base-pairing interactions to control self-assembly. More specifically, the scaffolded DNA origami approach [19,20] uses short ssDNA strands (~30-50 bases), referred to as staples, to fold a long ssDNA

loop (~7000-8000 bases), referred to as a scaffold, into a desired geometry. The scaffold is usually derived from the M13MP18 bacteriophage virus and staples can be ordered from commercial vendors. Castro et al. [22] reported the process of design and experimental protocols of DNA origami in detail and also introduced the computational tools for predicting the folded shape of DNA origami structures [42]. In recent years, many complex 2D and 3D structures have been designed and fabricated successfully, such as smiley faces [19], bent and twisted bars [21], and spheres [26]. Besides these static nanostructures with arbitrary geometries, dynamic structures are also designed and investigated carefully. For example, Liedl et al. [25] designed 3D prestressed tensegrity structures to inspect the mechanical properties of DNA bundles, and Andersen et al. [24] reported an approach to construct a nanoscale box with a controllable lid. Recently, the concept of DNA origami mechanisms (DOM) has been introduced [48,49] to fabricate nanostructures with complex and programmable motions, such as a four-bar Bennett linkage, which consists of four rigid links connected by four hinge joints, and a crank-slider linkage, which consists of three hinge joints coupled to a sliding joint. These kinematic joints that form the basis of DOM are designed by exploiting the flexibility of single-stranded DNA (ssDNA). Due to the extremely low stiffness of ssDNA strands, the motion of a DOM is subject to thermal fluctuations if no active actuation or control mechanism is present, yielding random motion along the designed motion path.

In order to simplify DNA origami design, computer-aided design tools have been developed, such as caDNAno [20]. It provides a design interface for two popular cross sections, honeycomb and square, used for DNA origami nanostructures design. When the

design is finished, the sequences of the staples can be determined and exported easily from caDNAno. Kim et al. [42] explained the fundamental principle of CanDo—a FEA software for structure prediction and stiffness analysis of the DNA origami nanostructures. These two tools have greatly improved the ability to efficiently design with DNA origami.

Although plenty of advances have been made on the geometric design of DNA origami nanostructures, the mechanical properties, such as bending and torsional stiffness, are still not well studied. It is still difficult to model the behavior of DNA nanostructures under various environments, especially the thermal fluctuations in solution. Usually, in the context of stiff dsDNA bundles, a single dsDNA helix can be modeled as a uniform elastic cylinder with appropriate material properties. The mechanical properties of the dsDNA bundle can be quantified by following the classic principles of mechanics of materials [21,25]. For example, the bending stiffness of a bundle of dsDNA is decided by the elastic modulus and inertial moment of the cross section. The elastic modulus of one dsDNA helix has been characterized by experiments and the inertial moment of a bundle of dsDNA helices can be calculated by following the parallel axis theorem. Figure 2.1 shows the double helix structure of DNA and how the cylinder model is used to represent the dsDNA helix. While the diameter of dsDNA is 2 nm, in the context of DNA origami nanostructures the diameter of each dsDNA swells to around 2.5 nm [20]. In the following sections, the 3D model of the design will always be shown as the cylinder model instead of the molecular model.

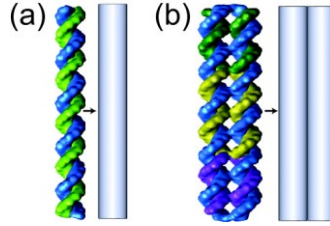


Figure 2.1: (a) The cylinder model of single dsDNA helix. (b) Two parallel dsDNA helices.

2.2. Design of compliant DNA origami joints and mechanisms

Currently, several kinematic joints, including revolute (hinge) and prismatic joints, have been fabricated with scaffold DNA origami [48]. These joints can be combined to form more complicated mechanisms, termed DNA origami mechanisms (DOM). In the design of DOM, hinge joints are designed by several ssDNA strands with 2-4 bases and rigid links by bundles of dsDNA helices [48,49]. Each hinge joint has at least two such ssDNA strand connections between the edges of the assembled links. In this way, the two connected links can rotate about the axis determined by the line passing through the ssDNA connections. However, these ssDNA based joints are subject to significant thermal fluctuations due to their extreme flexibility. It is a challenge to maintain the mobility of the nanomechanism but also achieve enough stiffness to overcome thermal fluctuations.

Fortunately, the methodology of compliant mechanisms [32,33,50] provides a feasible approach to achieve this goal by strategically designing desired stiffness at selected locations in a mechanism. At the nanoscale, it is challenging to assemble traditional kinematic joints from separate parts due to the complexity of topology of scaffold

patterning, which causes a decreasing fabrication yield of self-assembly. However, the fabrication of compliant mechanisms is relatively easy due to a smaller part count. The mobility of the compliant joint can be obtained by the deformation of the compliant component with a relatively low stiffness selectively placed in the mechanism [32,33,50]. DNA origami has the ability to fabricate parts with nearly arbitrarily complex geometry by self-assembly, so it is feasible to control the compliance of the parts. Here, compliant DNA origami mechanisms (CDOM) were introduced in detail.

2.2.1. Design of compliant DNA origami joints

Compliant joints are used to assemble the rigid parts to develop complex compliant mechanism which can achieve the desired motion [32]. Similar to traditional kinematic joints, compliant DNA origami joints can be designed by mimicking the macroscopic counterparts. Figure 2.2 shows six types of compliant joints including compliant wire, blade, hinge, notch, cross-strip R-joint and parallelogram P-joint and their DNA origami conception design respectively. As the fabrication yield of DNA origami depends on the geometrical complexity, actual DNA origami designs of these joints may be different from what depicted here. Sometimes it is necessary to change the design geometrical parameters to avoid the much high inner stress concentration that can fail the construction based on self-assembly. The basic compliant elements, such as the wire, blade, hinge and notch are much easy to be fabricated. Then much more complex compliant joints, such as the cross-strip R-joint and parallelogram P-joint (the bottom two row of Figure 2.2) can be synthesized from those basic compliant elements.

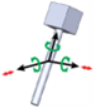

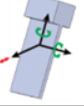

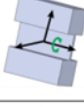

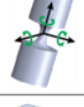

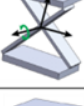
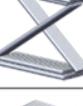
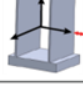

Compliant Joint	Symbol	DOF	Diagram	DNA Origami Design
Wire	W	5		
Blade	B	3		
Hinge	H	1		
Notch	N	3		
Cross straight revolute joint	CRJ	1		
Parralelogram prismatic joint	PPJ	1		

Figure 2.2: Basic elements for the joints design of CDOM.

2.2.2. Design of compliant DNA origami mechanisms

Based on the compliant joints, much more complex compliant DNA origami mechanisms with multiple DOF can be designed and fabricated. The design of links with different cross sections and shapes can be integrated to the CDOM design procedure as separated and customizable modules (Figure 2.3(a)). In addition, classic compliant mechanisms, such as the bistable mechanism and expandable square mechanism may be fabricated (Figure 2.3(b,c)).

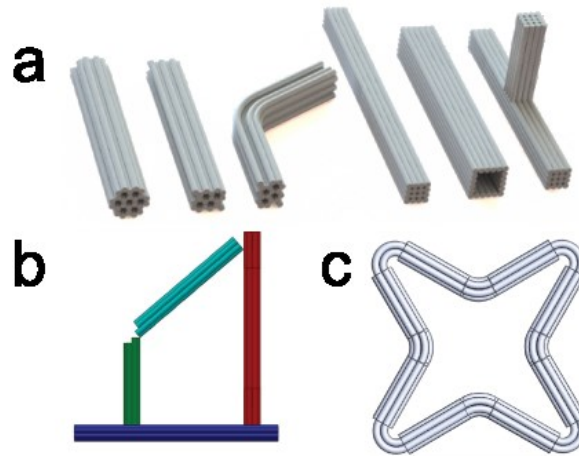


Figure 2.3: Design links and mechanisms. (a) Rigid parts with different cross sections. (b) A four-bar bistable mechanism. (c) Expandable mechanism.

In the following sections, mechanical models of ssDNA and dsDNA polymers will be discussed, and the Pseudo-rigid-body model (PRBM) [32,33,50,51] than can be used in design and analysis of compliant DNA origami links and mechanisms will be introduced.

2.3. Mechanical models of ssDNA and dsDNA

To study the force and deformation of CDOM, first select mechanics models for ssDNA and dsDNA strands are introduced and explained.

2.3.1. Persistence length of polymers and bundles

Persistence length, which is a measure of bending stiffness, is a widely used parameter for quantifying the mechanical properties of biopolymers. If the length of the polymer is much shorter than its persistence length, the polymer can be modeled as a uniform bar.

Experimental measurements [52–54] have shown the persistence length of dsDNA and ssDNA are about 50 nm and 2 nm, respectively. From an engineering analysis point of view, bending stiffness is more commonly used to study mechanics of polymers. In what follows, the relation between the persistence length and the bending stiffness is reviewed.



Figure 2.4: Sketch of single polymer.

In Figure 2.4, the energy stored in the curved short segment, E_0 , whose length is L can be calculated by

$$E_0 = \frac{1}{2} \kappa^2 (EI)L, \quad \kappa = \frac{1}{R} \quad (2.1)$$

Here, E is the Young's modulus, I is the moment of inertia, κ is the curvature, R is the curvature radius.

Based on the theorem of equipartition of energy, E_0 can also be related to thermal energy as:

$$\langle E_0 \rangle = \frac{1}{2} k_B T \quad (2.2)$$

Here $\langle E_0 \rangle$ denotes the expected value of E_0 ; k_B is the Boltzmann constant; and T is the absolute temperature. At room temperature, $k_B T = 4.1 pN \cdot nm$. Combining Eqs. (2.1) and (2.2) and noting that the persistence length, L_P , is defined as the length scale where the polymer length, L , is equal to the average radius of curvature, R , then the relationship between the persistence length and bending stiffness (EI) is obtained from Eqs. (2.1) and (2.2)

$$L_P = \frac{EI}{k_B T} \quad (2.3)$$

Therefore, the stiffness of dsDNA can be quantified by L_P . It follows that the elastic modulus of single dsDNA helix, E_{dsDNA} can be calculated by

$$E_{dsDNA} = \frac{L_P (k_B T)}{I_{dsDNA}} \quad (2.4)$$

Based on the assumption that a dsDNA helix in the design can be modeled as single uniform elastic cylinder and that cylinders in the bundle are securely coupled together, the bending stiffness, k_{BS} of the dsDNA bundles with inertia moment I , can be calculated by

$$k_{BS} = E_{dsDNA} I = \frac{L_P (k_B T)}{I_{dsDNA}} I \quad (2.5)$$

Here, I is the inertial moment of the bundle about its neutral axis. Generally, for a cross section with m dsDNA helices, the inertial moment is

$$I = m I_{dsDNA} + A \sum_{i=1}^m d_i^2 \quad (2.6)$$

Here, m is the number of dsDNA helices, A is the cross section area of single dsDNA helix and d_i is the distance between the center of i th single dsDNA helix and the neutral axis, see Figure 2.5.

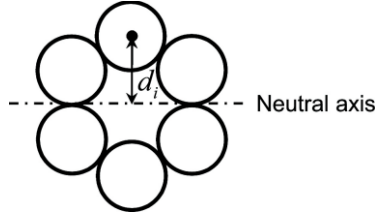


Figure 2.5: The cross section of a bundle of six dsDNA helices, each circle represents a dsDNA helix.

2.3.2. The Worm-like chain (WLC) model

If the polymer is much longer than its persistence length, the Worm-like chain model [54] can be used to determine the relationship between its end-to-end length and extension force as the following equation,

$$F_{WLC}(L_C, x) = \frac{k_B T}{L_P} \left[\frac{1}{4 \left(1 - \frac{x}{L_C}\right)^2} - \frac{1}{4} + \frac{x}{L_C} \right] \quad (2.7)$$

Here x is the end-to-end length of the polymer, and L_C is the contour length. For a DNA strand $L_C = mL_b$, where L_b is the base length, which is about 0.6 nm for ssDNA and 0.34 nm for dsDNA, and m is the number of bases or base pairs.

2.4. Pseudo-rigid-body models of compliant DNA links

Extensive studies on macro and micro compliant mechanisms have been carried out in the past two decades. Among the numerous methods developed for compliant mechanisms, the Pseudo-rigid-body model (PRBM) [32] is a well-studied method which models compliant links and joints as rigid links connected by a revolute joint with torsional springs. As a result, a compliant mechanism is converted into a traditional rigid-body mechanism, and the analysis and design methodology of rigid-body mechanisms can be applied.

However, to apply these PRBMs to compliant DNA origami mechanisms, the following two factors must be taken into account. First, essentially no joint in DNA origami mechanisms is perfectly rigid, it is necessary to consider the compliance even if joints are intended to be fixed ends to improve the accuracy of the PRBM. The second one is the cross section of a link is not always uniform which means beam components may be constructed by multiple segments with each segment defined by a length, cross section and bending stiffness. PRBMs for these two special cases are discussed in detail in the following section.

2.4.1. Effect of a non-rigid-fixed end on the PRBM for a compliant DNA link

To study the effect of the compliance at the non-rigid-fixed end on PRBM, a torsional spring with stiffness K_0 is placed at the fixed end as shown in Figure 2.6. For the design of DNA origami mechanisms, the non-rigid-fixed joint stiffness can be quantified experimentally [40]. Let us denote the rotation angle at the fixed end by θ_0 . For convenience, η is also defined as $\eta = K_0 / K_1$, the ratio of the relative stiffness of the fixed

end and the PRBM of the beam. The value of η depends on the design of the fixed end, in particular, the number and lengths of ssDNA connection that form the fixed joint. The larger the value of η , the closer the fixed end is to an ideal fixture joint.

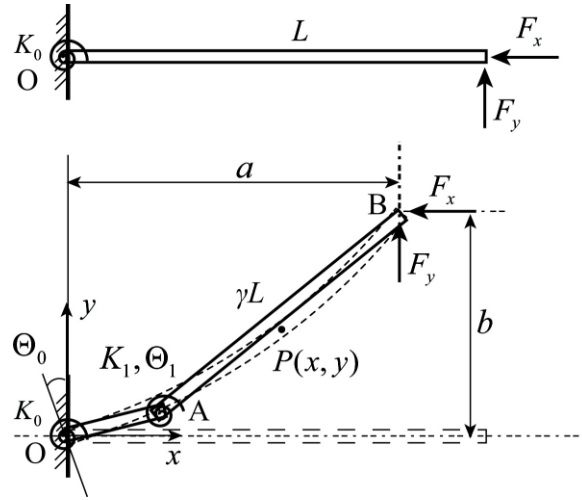


Figure 2.6: PRBM for cantilever beam with a non-rigid-fixed end.

The following steps explain how to determine the values of the PRBM parameters. First, the deformation of the beam is determined by the Euler-Bernoulli beam equation, written as

$$\theta'(s) = \frac{F_y(a-x) + F_x(b-y)}{EI} \quad (2.8)$$

where F_x and F_y are the horizontal and vertical component of the end force F . Eq. (2.8) can be solved numerically to obtain solution $\theta(s)$ with the following two boundary conditions,

$$\theta'(s)|_{s=L} = 0, \quad \theta(s)|_{s=0} = \Theta_0 \quad (2.9)$$

Then the position of the end tip (a , b) can be obtained. By moment equilibrium of the beam about the origin, O, the rotation angle of the torsional spring by can be calculated by

$$\Theta_0 = \frac{F_y a + F_x b}{K_0} \quad (2.10)$$

However the initial angle value at the fixed end Θ_0 is unknown. To determine the value of Θ_0 , iteratively searching is conducted in a range $[\Theta_{0\min}, \Theta_{0\max}]$ until the boundary conditions Eq. (2.9) and the equilibrium Eq. (2.10) are satisfied.

The energy stored in the system consists of two parts: the strain energy stored in the beam itself and the energy absorbed by the torsional spring,

$$E_b = \int_0^L \frac{EI}{2} (\theta'(s))^2 ds + \frac{1}{2} K_0 \Theta_0^2 \quad (2.11)$$

With regard to PRBM, the location of tip point B(B_x , B_y) can be easily computed with the kinematic parameters Θ_0, Θ_1 . And the end tip angle θ_0 is calculated by

$$\theta_0 = \Theta_0 + c_\theta \Theta_1 \quad (2.12)$$

The statics equations of the beam can be derived using the Jacobian of serial chains,

$$\begin{Bmatrix} K_0 \Theta_0 \\ K_1 \Theta_1 \end{Bmatrix} = \mathbf{J}^T \begin{Bmatrix} F_x \\ F_y \end{Bmatrix}, \quad \mathbf{J}^T = \begin{bmatrix} \frac{\partial B_x}{\partial \Theta_0} & \frac{\partial B_y}{\partial \Theta_0} \\ \frac{\partial B_x}{\partial \Theta_1} & \frac{\partial B_y}{\partial \Theta_1} \end{bmatrix} \quad (2.13)$$

Here \mathbf{J}^T is the transpose of Jacobian matrix of the kinematics equation and the potential energy stored in the two torsional springs is

$$E_p = \frac{1}{2} K_0 \Theta_0^2 + \frac{1}{2} K_1 \Theta_1^2 \quad (2.14)$$

In order to test the effect of K_0 on the accuracy of PRBM, η is defined as $\eta=K_1/K_0$ and a list of values are assigned to η , e.g. $\eta \in \{0.5, 1, 2, 4, 8, 20, 80, 200, 400, 1000\}$. Both the deformation (tip position and tip angle) and the energy can be evaluated by the beam model and PRBM. In order to simplify the calculation, the units of all parameter values used in the numerical calculation are bundled in the non-dimensional force index $f = FL^2 / (EI)$ [19].

Table 2.1: Basic parameters for Pseudo-rigid-body model.

n	ϕ	γ	K_Θ	c_θ
-5.0	11.3°	0.8391	2.4987	1.1788
-4.0	14.0°	0.8522	2.5899	1.1971
-3.0	18.4°	0.8669	2.6889	1.2119
-2.0	18.4°	0.8813	2.8016	1.2293
-1.5	33.7°	0.8796	2.7808	1.2322
-1.0	45.0°	0.8707	2.7282	1.2323
-0.5	63.4°	0.8612	2.6932	1.2348
0.0	90.0°	0.8517	2.6762	1.2385
0.5	116.6°	0.843	2.6374	1.243
1.0	135.0°	0.836	2.6126	1.2467
1.5	146.3°	0.8311	2.5929	1.2492
2.0	153.4°	0.8276	2.5971	1.2511
3.0	161.6°	0.8232	2.5674	1.2534
4.0	166.0°	0.8207	2.5651	1.2548
5.0	168.7°	0.8192	2.5625	1.2557
7.5	172.4°	0.8168	2.5598	1.257
10.0	174.3°	0.8156	2.566	1.2578

$$n = -1 / \tan(\phi).$$

First, $\eta=0.5$ and a unit end load force (i.e., $f=1$) are chosen for the calculation and the direction angle of the end load force is shown in the

Table 2.1. Figure 2.7(a) shows the end tip position and three deformed beams, end tip angle and energy calculated by PRBM and beam model. The results show that the PRBM matches the beam model very well. Second, three special cases are studied. Each case has the same end tip unit force but different force directions ($\phi=90^\circ$, $\phi=45^\circ$ and $\phi=135^\circ$) and also different ratio η . Figure 2.7(b, c, d) shows the end tip position, end tip angle and energy calculated by the beam model and PRBM.

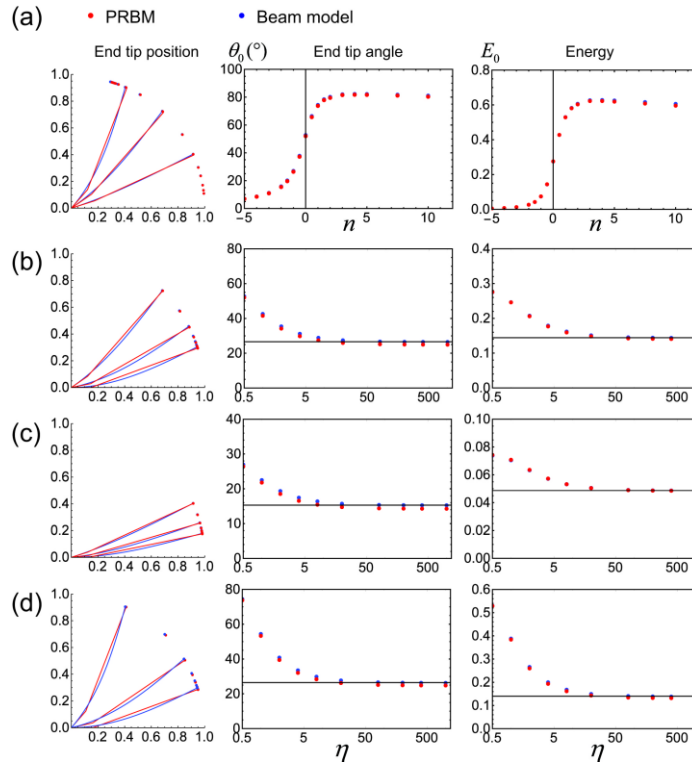


Figure 2.7: Comparison between PRBM (red dots or lines) and beam model (blue dots or lines) for non-rigid-fixed end cantilever beam.

The results show that the effect of the fixed end stiffness to the accuracy of the PRBM is small. This is because the end load force direction angle ϕ relative to the fixed end of the beam is changed during the deformation, but the γ and K_θ were chosen according to the initial force direction angle. The larger the change of the angle ϕ is, the larger the error between the PRBM and beam model will be. Hence, the classic PRBM can be applied to the analysis of this type of DNA origami link if its deformation or the change of the relative force angle ϕ is small.

2.4.2. PRBM for non-uniform cross section cantilever beams

In the design of DNA origami mechanisms, a link may consist of a DNA bundle where the cross section (i.e. number of dsDNA strands in the bundle) varies along the length. For example, it is often necessary to increase the cross section at the ends of links to appropriately design joints. To improve the accuracy of the PRBM model these types of links may be broken down into different segments, which adjusts the overall compliance of the link.

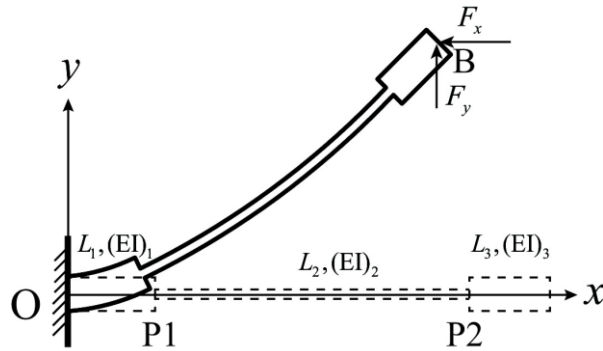


Figure 2.8: Three segments cantilever beam.

Figure 2.8 shows a general three segment beam with larger cross sections on the two ends and smaller cross section on the middle. L is the total length of the beam, L_1 , L_2 and L_3 are the lengths and $(EI)_1$, $(EI)_2$ and $(EI)_3$ are the bending stiffness of each segment.

2.4.3. Euler-Bernoulli beam model for three segments cantilever beam

All three segments L_1 , L_2 and L_3 were treated as three independent compliant links. The bending angles for each segment are defined as $\theta_1(s)$, $\theta_2(s)$, and $\theta_3(s)$. Due to the less of boundary conditions, similar solving strategy as the non-rigid-fixed end beam was used to solve Eq. (2.8) for segment L_1 . The beam equation was solved based on the best $\theta'(0)$ that can satisfy all boundary conditions. The detailed process was listed in below:

1. Search $\theta'(0)$ that satisfies the boundary conditions;
2. Solve the beam equation for segment L_1 ;
3. Solve the beam equation for segment L_2 , The boundary conditions for segment L_2 are:

$$\theta_2(L_1) = \theta_1(L_1) \text{ and } \theta_2'(L_1) = ((EI)_1 / (EI)_2)\theta_1'(L_1);$$

4. Solve the beam equation for segment L_3 , The boundary conditions for segment L_3 are:

$$\theta_3(L_1 + L_2) = \theta_2(L_1 + L_2) \text{ and } \theta_3'(L_1 + L_2) = ((EI)_2 / (EI)_3)\theta_2'(L_1 + L_2);$$

5. Check the value of the $\theta_1'(0)$ that satisfy equation $\theta_1'(0) = (F_y B_x + F_x B_y) / (EI)_1$.

The energy stored in the three segment beam is

$$\begin{aligned}
E_0 = & \int_0^{L_1} \frac{(EI)_1}{2} (\theta_1'(s))^2 ds + \int_{L_1}^{L_1+L_2} \frac{(EI)_2}{2} (\theta_2'(s))^2 ds \\
& + \int_{L_1+L_2}^L \frac{(EI)_3}{2} (\theta_3'(s))^2 ds
\end{aligned} \tag{2.15}$$

2.4.4. One torsional spring PRBM for three segments cantilever beam

A model based on the classic PRBM was introduced here for the analysis of the three segment beam, termed PRB-1R model. The two end segments are treated as rigid parts and only consider the deformation of the middle segment. But the end load on segment L_2 is changed to a combined force and moment because the force is actually applied on the end tip of the beam segment. Hence, a moment is introduced to the end of segment L_2 equal to the force multiplied by the length, L_3 . According to the classic PRBM, the torsional spring stiffness will be changed. Here γ and K_Θ are kept as the same as classic PRBM, but a correction coefficient ρ was introduced to the torsional spring stiffness of PRBM, i.e.

$$K = \gamma K_\Theta \frac{(EI)_2}{L_2} \rho \tag{2.16}$$

A proper ρ is the key to the accuracy of PRBM. Optimized ρ should be obtained to minimize the strain energy difference between the beam model and PRBM as energy is the most important measure for DNA origami nanostructures. The errors of end tip position, end tip angle and energy for each case are defined as

$$\Delta_{tip} = \frac{\sqrt{(B_{xP} - B_{xB})^2 + (B_{yP} - B_{yB})^2}}{\sqrt{(B_{xB} - L)^2 + (B_{yB} - 0)^2}} \tag{2.17}$$

$$\Delta_{\theta_0} = |\theta_{0P} - \theta_{0B}| / \theta_{0B} \quad (2.18)$$

$$\Delta_{E_0} = |E_P - E_B| / E_B \quad (2.19)$$

Here (B_{xP}, B_{yP}) , θ_{0P} , and E_P are the end tip position, end tip angle and energy calculated by PRBM, while (B_{xB}, B_{yB}) , θ_{0B} , and E_B are the corresponding end tip position, end tip angle and energy calculated by beam model. The average errors of end tip position, end tip angle and energy for different load force angles are $\bar{\Delta}_{tip}$, $\bar{\Delta}_{\theta_0}$ and $\bar{\Delta}_{E_0}$.

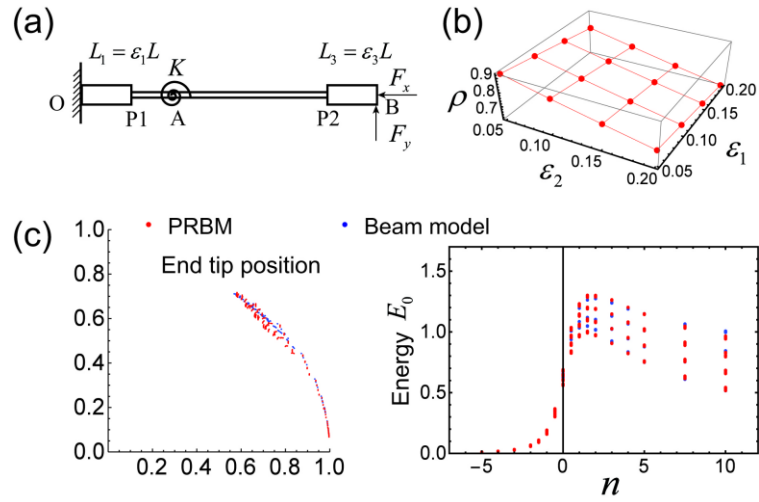


Figure 2.9: One revolute joint PRBM for the three segment cantilever beam. (a) Sketch of the PRBM. (b) Test of different segment length ratios. (c) Comparison of end tip position and energy between PRBM and beam model.

For convenience, relationships of geometrical parameters and bending stiffness are defined as $L = L_1 + L_2 + L_3$, $L_1 = \epsilon_1 L$, $L_3 = \epsilon_2 L$, $L_2 = L - L_1 - L_3$, $(EI)_1 = e_1 (EI)_2$,

$(EI)_3 = e_2(EI)_2$. Here, ε_1 and ε_2 are the ratios of L_1 and L_3 over L respectively, e_1 and e_2 are the ratios of the bending stiffness of two end segments over the middle segment.

To test the effect of $(\varepsilon_1, \varepsilon_2)$ on the accuracy of the PRBM, e_1 and e_2 are assigned as 2 and the value of $(\varepsilon_1, \varepsilon_2)$ is varied as $\{0.05, 0.1, 0.15, 0.2\}$. Here the nondimensional tip force is increased to $f=3$. For each of 16 combinations of $(\varepsilon_1, \varepsilon_2)$, the values of n and ϕ are chosen from

Table 2.1. The optimal value of ρ should be determined as described earlier. Figure 2.9 shows the comparison of the beam model and PRBM. As we can see, the end tip position error is noticeable and ε_2 has a bigger effect to ρ than ε_1 . In addition, the energy predicted by the PRBM has an insignificant error with the beam model. These errors are mostly attributed to the compliance of the two end segments. Of course, further studies are required to verify the conclusion.

2.4.5. Three torsional springs PRBM for three segments cantilever beam

In order to obtain a more accurate PRBM, compliance of the two end segments is included in our modeling process and each segment is treated respectively. For the two short segments, the PRBM for compliant hinge can be used, while for the long segment, PRBM for the cantilever beam should be employed. Finally, the model has 3 revolute joints and torsional springs as shown in Figure 2.10(a), and is referred to as the PRB-3R model. K_1 and K_3 are calculated by

$$K_1 = \frac{(EI)_1}{L_1}, K_3 = \frac{(EI)_3}{L_3} \quad (2.20)$$

and K_2 is calculated by Eq. (2.16). The rotation angles of the corresponding torsional springs are Θ_1 , Θ_2 and Θ_3 . From the new model, the end tip position $B(B_x, B_y)$ can also be easily derived from the kinematics equations. The statics equations of the new model are:

$$\begin{Bmatrix} K_1\Theta_1 \\ K_2\Theta_2 \\ K_3\Theta_3 \end{Bmatrix} = \mathbf{J}^T \begin{Bmatrix} F_x \\ F_y \end{Bmatrix}, \quad \mathbf{J}^T = \begin{bmatrix} \frac{\partial B_x}{\partial \Theta_1} & \frac{\partial B_y}{\partial \Theta_1} \\ \frac{\partial B_x}{\partial \Theta_2} & \frac{\partial B_y}{\partial \Theta_2} \\ \frac{\partial B_x}{\partial \Theta_3} & \frac{\partial B_y}{\partial \Theta_3} \end{bmatrix} \quad (2.21)$$

The end tip deflection angle will be

$$\theta_0 = \Theta_1 + c_\theta \Theta_2 + \Theta_3 \quad (2.22)$$

The energy stored in the PRB-3R model will be

$$E_0 = \frac{1}{2} K_1 \Theta_1^2 + \frac{1}{2} K_2 \Theta_2^2 + \frac{1}{2} K_3 \Theta_3^2 \quad (2.23)$$

The numerical example in the former section is evaluated here again based on the PRB-3R model. Different from the PRB-1R model, the rotation angle of each torsional spring is obtained by implementing Eq. (2.21). Figure 2.10 shows the comparison of the new PRB-3R model and the beam model. As one can see, the range of ρ is between 0.81 and 0.97, which is smaller than that of PRB-1R model. In addition, the relative errors of end tip position, end tip angle and energy are smaller than 4%, 5%, 6% and the corresponding average errors are smaller than 2%, 3% and 4%, respectively. In addition,

ρ and the average errors of end tip position, end tip angle and energy are more sensitive to ε_2 than to ε_1 . It implies that the moment introduced by the segment L_3 must be considered if a PRBM is used for the analysis. Also, for the compliant DNA origami links, the segment L_3 should be designed as short as possible in order to reduce the moment load to the middle compliant segment.

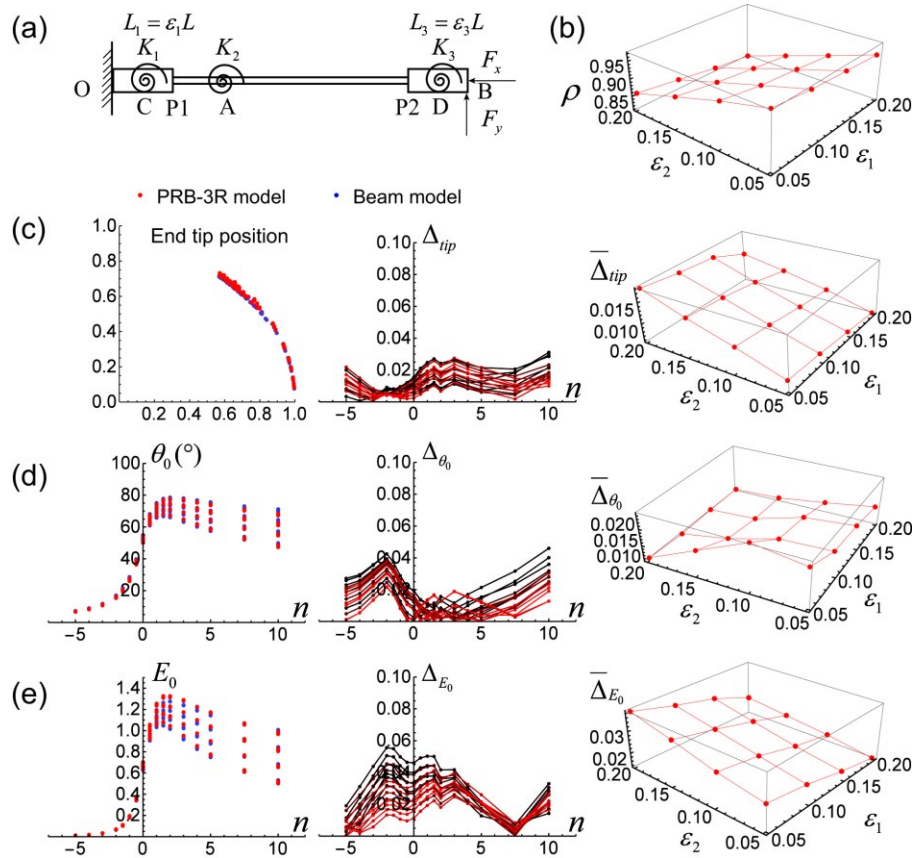


Figure 2.10: PRB-3R model for non-uniform cross section beam. (a) Sketch of the model. (b) Test of different segment length ratios. (c, d, e) Comparisons of end tip position, end tip angle, energy and their relative errors and average errors.

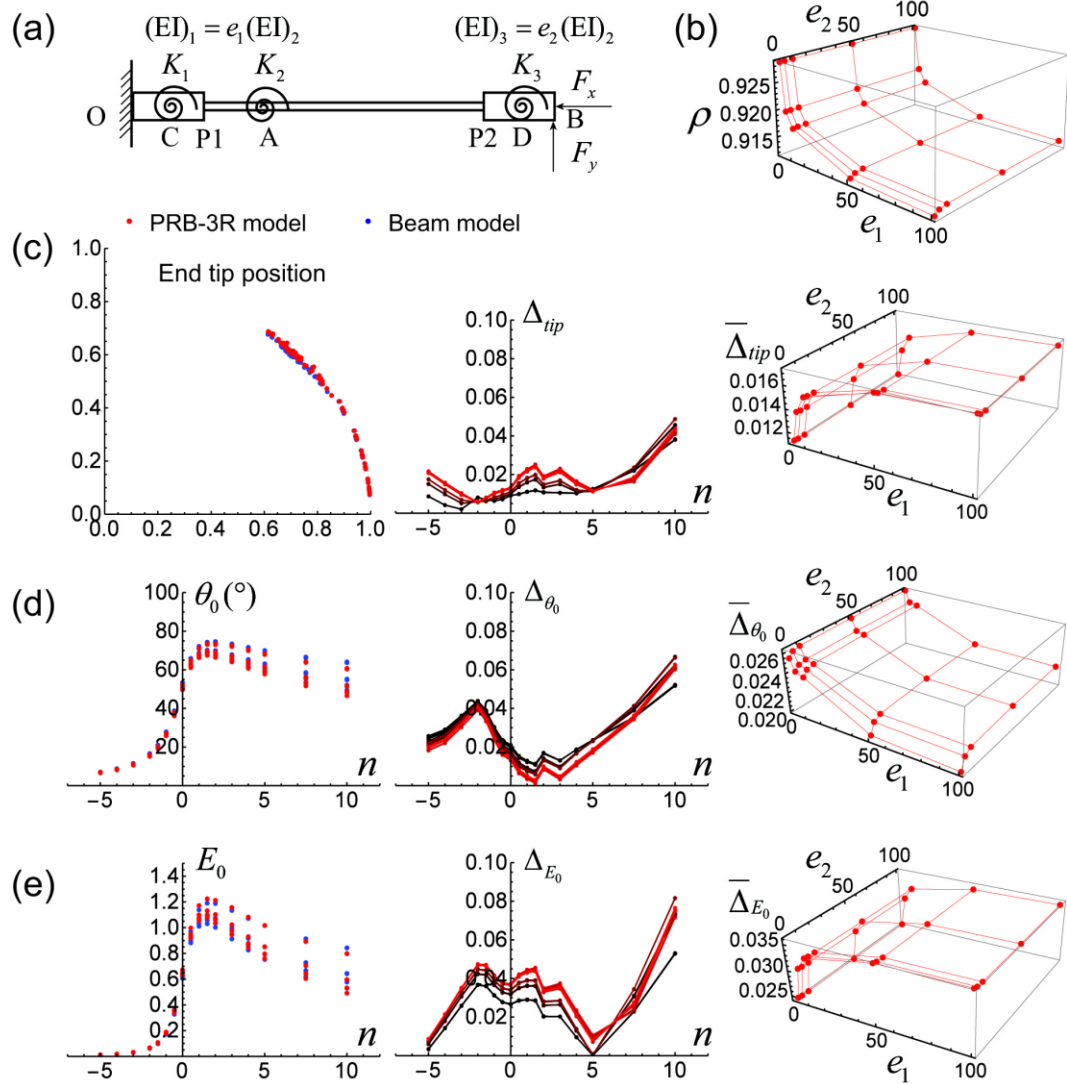


Figure 2.11: Test the PRB-3R model for different bending stiffness of different segment. (a) Sketch of the model. (b) Test of different segment length ratios. (c, d, e) Comparisons between PRB-3R model and beam model.

Similar to the previous case, the effect of e_1 and e_2 on the accuracy of the PRBM is studied. Varying e_1 and e_2 with values in the list of $\{2.0, 5.0, 10.0, 50.0, 100.0\}$, and setting $\varepsilon_1 = 0.1, \varepsilon_2 = 0.1$ and nondimensional force $f=1$, evaluation parameters can be

determined, including the optimal value of ρ as well as errors of tip positions and energy between the PRB-3R model and beam model, as shown in Figure 2.11. The range $\rho \in [0.91, 0.93]$ means it is not sensitive to the bending stiffness of the two end segments e_1 and e_2 . The relative errors of end tip position, end tip angle and energy are also small when $n \leq 7.5$, i.e. $\phi \leq 172.4^\circ$. In addition, all of their corresponding average errors are smaller than 3%. ρ and all of the average errors are more sensitive to e_1 than to e_2 and the effect of e_2 can even be neglected. This means the bending stiffness of the segment L_3 does not affect the flexibility of the whole link significantly especially for large cross sections, which result in larger bending stiffness for the design of end segment in CDOM link.

2.4.6. Apply the PRB-3R model for non-rigid-fixed end three segments cantilever beam

Furthermore, the PRB-3R model is applied to the analysis of non-rigid-fixed cantilever beam (Figure 2.12). The end tip position (B_x, B_y) can be easily derived from the kinematics equations and the statics equations of the model,

$$\begin{Bmatrix} K_0 \Theta_0 \\ K_1 \Theta_1 \\ K_2 \Theta_2 \\ K_3 \Theta_3 \end{Bmatrix} = \mathbf{J}^T \begin{Bmatrix} F_x \\ F_y \end{Bmatrix}, \quad \mathbf{J}^T = \begin{bmatrix} \frac{\partial B_x}{\partial \Theta_0} & \frac{\partial B_y}{\partial \Theta_0} \\ \frac{\partial B_x}{\partial \Theta_1} & \frac{\partial B_y}{\partial \Theta_1} \\ \frac{\partial B_x}{\partial \Theta_2} & \frac{\partial B_y}{\partial \Theta_2} \\ \frac{\partial B_x}{\partial \Theta_3} & \frac{\partial B_y}{\partial \Theta_3} \end{bmatrix} \quad (2.24)$$

And the end tip angle is

$$\theta_0 = \Theta_0 + \Theta_1 + c_\theta \Theta_2 + \Theta_3 \quad (2.25)$$

The energy absorbed by the torsional springs will be

$$E_0 = \frac{1}{2} K_0 \Theta_0^2 + \frac{1}{2} K_1 \Theta_1^2 + \frac{1}{2} K_2 \Theta_2^2 + \frac{1}{2} K_3 \Theta_3^2 \quad (2.26)$$

The detailed solving procedure is described as the following:

1. Search for Θ_0 in a domain that satisfies the boundary conditions of beam equation;
2. Solve the beam model Eq. (2.8);
3. Check the equilibrium angle Θ_0 by Eq. (2.10);
4. Calculate the energy stored in beam (Eq. (2.15)) and the non-rigid-fixed end torsional spring;
5. Find ρ that minimizes the average energy error calculated by Eq. (2.19).

The numerical example in section 4.2.2 is used to test this model. First, model parameters are set as $\eta = K_0 / K_2 = 0.5$, $e_1 = e_2 = 2$, ε_1 and $\varepsilon_2 \in \{0.05, 0.1, 0.15, 0.2\}$ respectively. Figure 2.12(b) compares the end tip position and energy stored between the PRB-3R model and beam model. Secondly, $\eta = K_0 / K_2 = 2.0$ is used and re-solve the beam model and PRB-3R model. The end tip position and stored energy are shown in Figure 2.12(c). For this example, the torsional spring on the fixed end has a negligible effect on the PRB-3R model for relatively small to moderate deformations.

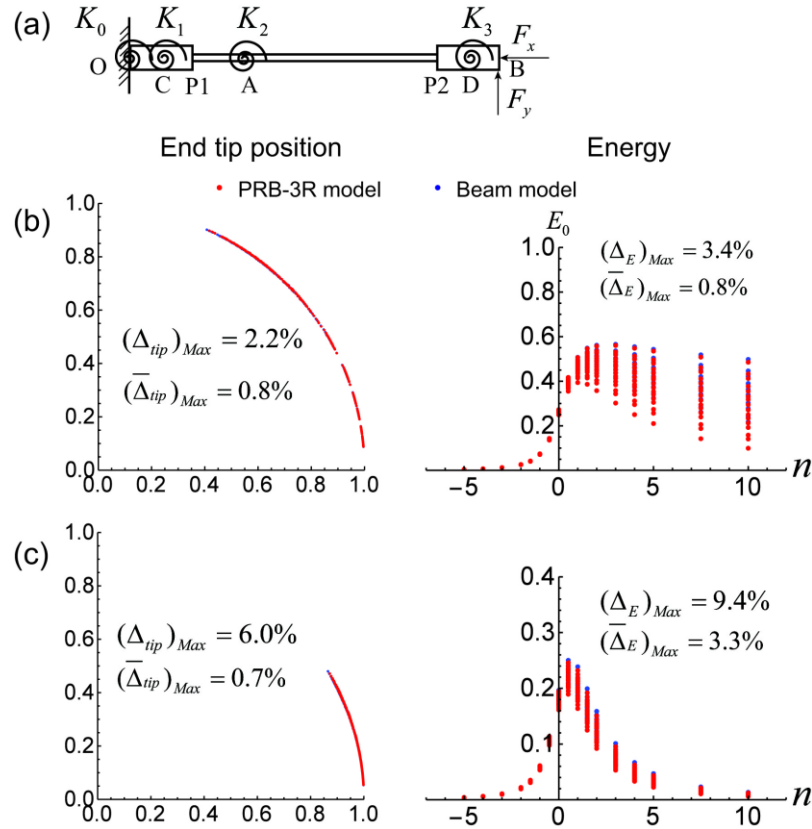


Figure 2.12: PRB-3R model applied on the non-rigid-fixed multi-cross section cantilever beam. (a) Sketch of the model. (b, c) End tip position, stored energy calculated by the PRB-3R model and the beam model.

2.5. Conclusions

The well-studied compliant mechanism theories as well as enormous computational tools provide a useful and convenient avenue to design and analyze these CDOM. More specifically, Pseudo-rigid-body models can be used to design and predict the performance of CDOM, especially for compliant hinge joint and multi-segment compliant link.

Chapter 3: DNA Origami Compliant Nanostructures with Tunable Mechanical Properties

DNA origami enables fabrication of precise nanostructures by programming the self-assembly of DNA. While this approach has been used to make a variety of complex 2D and 3D objects, the mechanical functionality of these structures is limited due to their rigid nature. Here, the fabrication of deformable, or compliant, objects has been explored, which can help establish a framework for mechanically functional nanostructures. This compliant design approach is used in macroscopic engineering to make devices including sensors, actuators, and robots. Compliant nanostructures introduced here is built by utilizing the entropic elasticity of single-stranded DNA (ssDNA) to locally bend bundles of double-stranded DNA (dsDNA) into bent geometries whose curvature and mechanical properties can be tuned by controlling the length of ssDNA strands. The ability to achieve a wide range of geometries by adjusting a few strands in the nanostructure design has been demonstrated here. Furthermore, a mechanical model is developed to predict both geometry and mechanical properties of these compliant nanostructures that agrees well with experiments. The results provide a basis for the design of mechanically functional DNA origami devices and materials.

3.1. DNA origami compliant mechanisms

DNA origami nanostructures contain several thousand base-pairs arranged into objects with typical dimensions of ~10-100nm [19]. Since spatial registry is largely retained over every base-pair in the object, chemical functionalities can be placed on objects with ~nm resolution. Current applications of DNA origami exploit this precise geometric design. Furthermore, computer aided design programs, such as caDNAo[55], have been developed to simplify the sequence design process; and the finite element based software, CANDO, was developed to predict the folded geometry of scaffolded DNA origami structures, which is particularly useful when designing structure that incorporate local stresses to create curved or twisted objects. These computer aided design tools facilitate rapid prototyping of designed DNA nanostructures. And the development of theoretical models has provided effective and convenient methods to analyze the behavior of double helical nucleic-acid structures [52,56–58]. The demonstrated applications have fostered a growing interest in building DNA-based devices, machines, and robots [45,59–61]. However, applications of DNA origami to date have largely focused on geometric design. The fabrication of mechanically functional structures such as springs, actuators, manipulators, which could greatly broaden the scope of DNA nanomachines has remained largely unexplored. Previous work to create controllable curvature in DNA origami nanostructures were either designed on an ad hoc basis, or followed a mechanical model that predicted only geometry. The finite element based software, CANDO, is a useful computational tool to predict the folded geometry and thermal fluctuations of curved or twisted structures; however, it is not currently suited to analyze structures that

incorporate ssDNA components or structures that undergo large deformations in general. Furthermore, a theoretical model provides a more useful design tool where parameters can be quickly optimized for desired structural and material behavior.

In general, mechanical functionality requires two key capabilities: 1) an ability to specifically design mechanical behavior, and 2) the ability to integrate dynamics (i.e. motion). In engineering design, controllable mechanical behavior is achieved by using multiple material components with the desired mechanical stiffness. The stiffness of DNA origami components can vary over several orders of magnitude from highly flexible single-stranded DNA (ssDNA), which exhibits a persistence length of $\sim 2\text{nm}$ [53], up to bundles of double-stranded DNA, which can be 1000-fold stiffer [44]. However, integrating these components to achieve tunable mechanical behavior has not been explored. Furthermore, achieving controlled dynamic behavior in designed DNA systems remains a key challenge in the field. This is usually done in macroscopic systems by integrating flexible elements with constrained motion (i.e. joints), but flexibility in nanoscale systems leads to random thermal motion [62].

One promising approach to achieve controlled mechanical and dynamic behavior with stiff components that has been successfully applied for microscopic machines [63,64] is compliant mechanism design. Compliant mechanisms [32,50] utilize components with varying stiffness and geometry to achieve controlled motion. This approach requires an ability to design components with controllable mechanical behavior and geometry. Here a foundation was established for DNA origami compliant mechanisms by designing,

fabricating, and characterizing a deformable (compliant) DNA origami nanostructure with controllable geometry and mechanical behavior.

3.2. Design of DNA origami compliant joint

The structure was designed to behave as a compliant joint similar to a hinge with a torsional spring [39]. The design was constructed as an eighteen-helix bundle that was organized into three layers of six helices (Figure 3.1). The two ends, which contain all 18 helices, are stiff components that could be integrated into a larger scale mechanism. The central portion, which forms the basis of the compliant joint, consists of the top layer of 6 dsDNA helices (green in Figure 3.1) and 6 ssDNA connections across the bottom layer (blue in Figure 1).

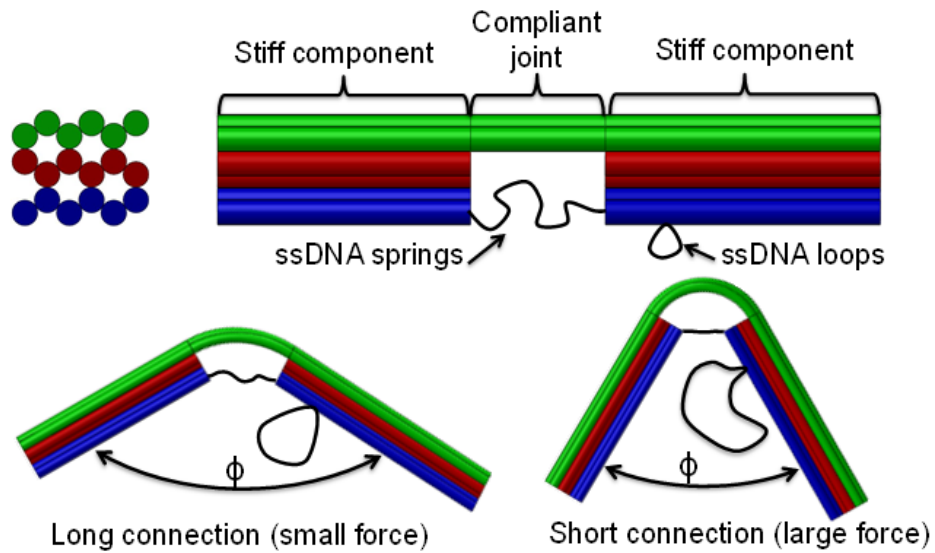


Figure 3.1: 3D model and function of DNA origami compliant nanostructure.

Table 3.1: Design parameters of the ssDNA springs.

Design	Lower three ssDNA springs	Upper three ssDNA springs
Version 1 (0 bases)	0 bases ssDNA+10 bases dsDNA	24 bases ssDNA
Version 2 (11 bases)	11 bases ssDNA +10 bases dsDNA	35 bases ssDNA
Version 3 (32 bases)	32 bases ssDNA +10 bases dsDNA	56 bases ssDNA
Version 4 (53 bases)	53 bases ssDNA +10 bases dsDNA	77 bases ssDNA

The ssDNA connections function as entropic springs that apply a force causing the top layer to bend. The magnitude of the force, and correspondingly the joint angle (ϕ), depends on the length of the ssDNA springs. In a bent configuration, the ssDNA springs connecting the top 3 helices of the blue layer span a larger distance than the ssDNA springs connecting the bottom 3 helices of the blue layer. Therefore, the ssDNA connections between the top three helices were correspondingly made longer. For subsequent definition, it is referred to the length of the shorter ssDNA springs. Complete design details of all versions are given in Table 3.1.

The structure is an 18-helix bundle organized into 3 layers (top left). The two ends that contain all 18 helices are stiff components that could be integrated into a larger mechanism. The central portion balances tension in the ssDNA “springs” with bending of the top 6-helix layer. The joint angle, ϕ , can be adjusted by shifting length of ssDNA between the springs and the loops. A novel approach is developed to modulate the structural and mechanical properties using scaffold loops as a reservoir of additional ssDNA length (Figure 3.1, upper right).

The combined number of ssDNA bases in the springs and loops remained constant. Small joint angles could be obtained by shifting length from the ssDNA springs to the reservoir loops, and in contrast, large angles could be obtained by shifting ssDNA from the loops to the springs. In this way, structures with distinct geometries (joint angles) could be achieved by switching out only the staples located between the loops and the springs. The scaffold routing is optimized to minimize the possibility of secondary structure [65,66] in the ssDNA springs. For cases of small joint angles, where the ssDNA loops were long, short staples (~20 bases) were added to minimize the possibility of multiple structures interacting at the single-stranded loops.

3.3. Experiment results

Agarose gel electrophoresis (Figure 3.2(a)) reveals geometric differences between design versions. The bands from left to right are: DNA ladder, ssDNA scaffold, and five design versions with 0, 11, 32, 53, and 74 bases in the ssDNA springs on the following five columns. TEM images of the five versions (Figure 3.2(b to f)) confirm that longer ssDNA springs result in larger joint angles. In many cases, the details of the compliant joint (6 helix layer and gap between the other two layers) are visible. Aside from the smallest angle version, all of the structures adopt a smooth curvature that depends on the force applied by the ssDNA springs. In the case of the smallest angle, some structures adopt a kinked configuration (Figure 3.2(b)). This can be explained by the existence of nicks that occur at the staple cross-overs in the 6-helix layer of the compliant joint. Kinks occur at nicks due to reduced stiffness [67].

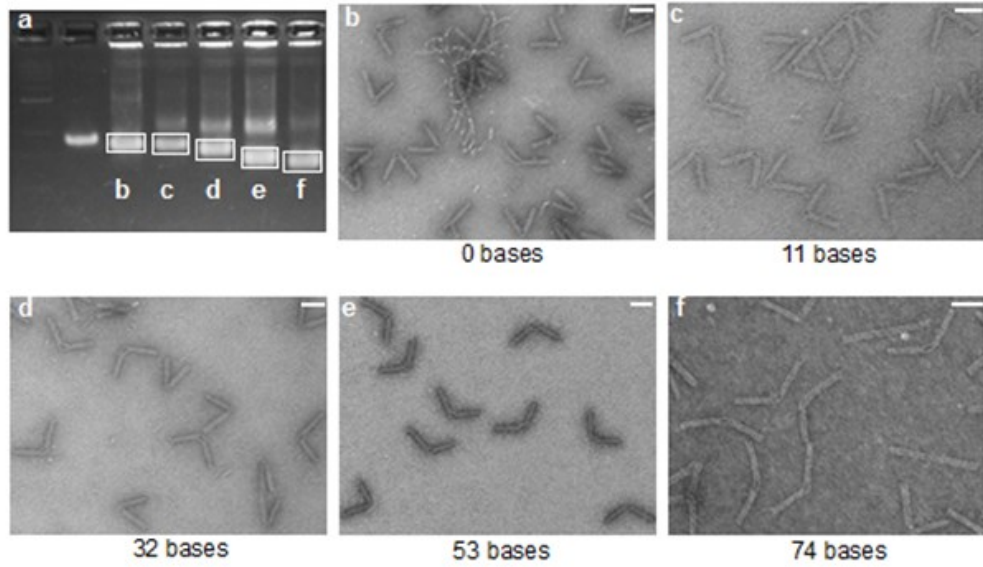


Figure 3.2: TEM experimental results. (a) Gel electrophoresis reveals geometric differences between design versions. (b to f) TEM images of the five design versions. Scale bars, 50nm.

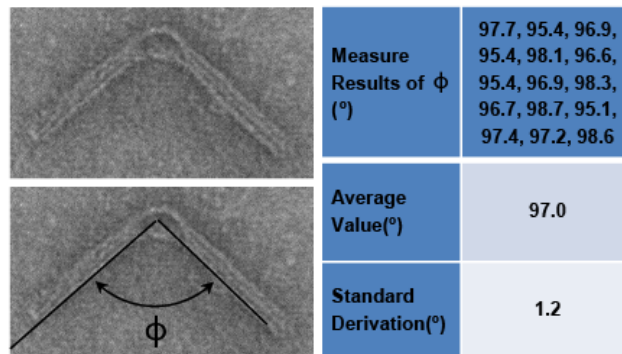


Figure 3.3: Angle measurement error analysis.

The software ImageJ was used to manually measure the angles of each structure from TEM images. Error of manual angle measurement was evaluated by making multiple

measurements on the same structure. The standard deviation of the manual measurement was found to be 1.2° (Figure 3.3). To ensure measurement of properly folded structures, only the particles with smooth curved segment and an obvious gap between the other two layers were included in analysis.

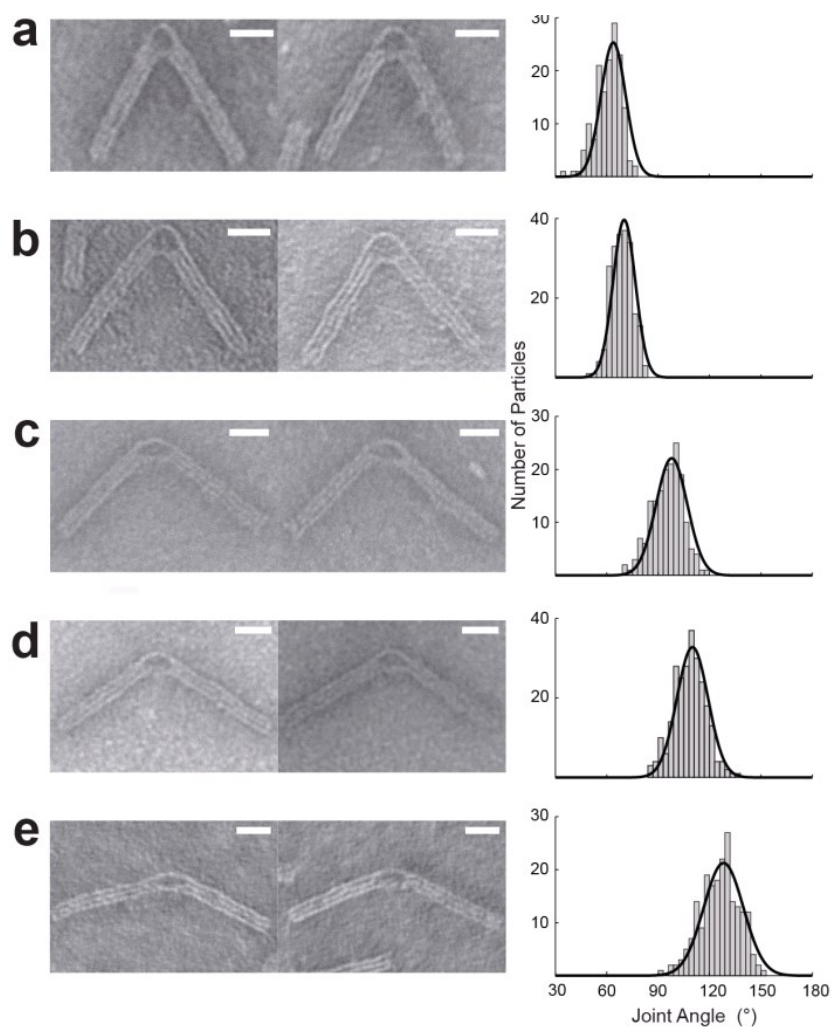


Figure 3.4: Conformational analysis of the TEM experiment results. (a to e) Typical particles and histogram distribution of versions with 0, 11, 32, 53, and 74 bases in the ssDNA springs. All scale bars are 20 nm.

A Gaussian distribution was used to fit the angular distributions of each version (Figure 3.4). (a to e) Typical particles and histogram distribution of versions with 0, 11, 32, 53, and 74 bases in the ssDNA springs. The black lines show Gaussian fits to the data. The angles corresponding to the peak values of Gaussian fits were 56.5° (n=154), 70.2° (n=213), 97.9° (n=169), 110.0° (n=252), 128.2° (n=204) and correspondingly the bending angles of the curved segment range from about $\sim 125^\circ$ to $\sim 50^\circ$. The angular distributions also revealed that longer ssDNA springs resulted in larger variation in the joint angle suggesting a lower joint stiffness (Figure 3.4). Due to thermal fluctuations, the compliant joint fluctuates about the equilibrium angle, which occurs when the extensional energy in the springs balances the bending energy in the 6-helix layer. The entropic elasticity of the ssDNA exhibits higher stiffness at larger extension, or larger angles, resulting in a slight asymmetry of the angular distribution (steeper gradient at larger angles).

3.4. Theoretical model of balanced bending and entropic tension

Previous work to create controllable curvature in DNA origami nanostructures were either designed on an ad hoc basis [26], or followed a mechanical model that predicted only geometry [21]. The finite element based software, CANDO [42], is a useful computational tool to predict the folded geometry and thermal fluctuations of curved or twisted structures; however, it is not currently suited to analyze structures that incorporate ssDNA components or structures that undergo large deformations in general. Furthermore, a theoretical model provides a more useful design tool where parameters can be quickly optimized for desired structural and material behavior.

In this section, the details are provided on the derivation of the theoretical model for predicting the joint angle of the designed compliant nanostructures that are controlled by the tunable length of the ssDNA springs. This model closely captured the equilibrium angle and the angular distributions for the compliant nanostructures.

3.4.1. Theoretical model of bending

The design of these kind of compliant joints is shown detailed in Figure 3.5(a) again. Each cylinder represents a dsDNA helix. The length of the middle compliant segment (joint) is denoted by L_0 . The two end segments are designed with bundles of dsDNA and are considered as relatively rigid since they contain the 18 helices.

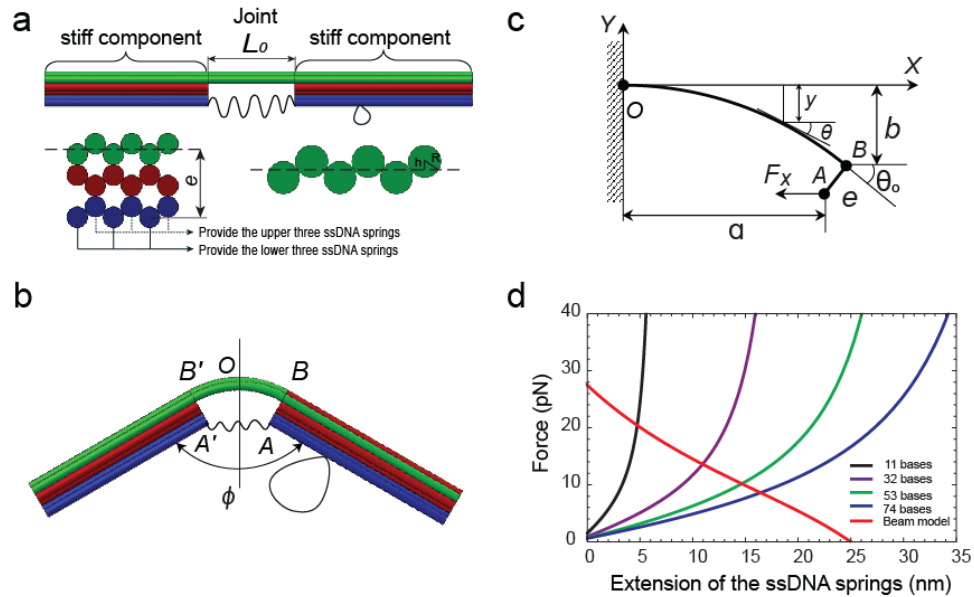


Figure 3.5: Analysis based on the Bernoulli-Euler beam model and WLC model. (a) The cylinder model (b) the deformed compliant joint (c) right half of the compliant joint (d) force needed to bend the joint.

When one or more ssDNA springs are applied to connect the two rigid arms at A and A', they exert an inward force on the connection points and cause the compliant segment to bend (Figure 3.5(b)). For simplicity, the end segments are treated as rigid bodies and the compliant segment as an incompressible beam. The goal here is to calculate the equilibrium angle of deflection of the beam and predict the energy landscape that governs fluctuations about the equilibrium angle.

Due to symmetry, only the right half of the beam needs to be analyzed, schematically shown in Figure 3.5(c). The length of the half-beam model, L , is $L_0/2$. The segment AB is considered a rigid bar of length e . Point B is the tip of the deflected beam. b is the vertical coordinate of point B, and a is the horizontal coordinate of point A in the deformed configuration.

Suppose the internal load by the ssDNA springs is denoted by F_x . Based on the Bernoulli-Euler beam theory¹, the beam slope angle $\theta(s)$ ($0 \leq s \leq L$) is subject to the following differential equation

$$\frac{d\theta(s)}{ds} = \frac{M(s)}{EI} \quad (3.1)$$

where E and I are the elastic modulus and moment inertia of the beam respectively. Here $M(s)$ is the internal moment at any arbitrary point s in the beam caused by the load F_x , calculated as

$$M(s) = F_x(y(s) - b - e \cos \theta_s) \quad (3.2)$$

where $y(s)$ represents the deflection of the beam at the point s and $\theta_s = \theta(L)$ is the tip deflection angle. Differentiating Eq.(3.1) and substituting Eq.(3.2) yield

$$\frac{d^2\theta(s)}{ds^2} = \frac{F_x}{EI} \frac{dy(s)}{ds} \quad (3.3)$$

By using the geometric relationship $\frac{dy(s)}{ds} = -\sin \theta(s)$, Eq.(3.3) becomes the following second order differential equation

$$\frac{d^2\theta(s)}{ds^2} = -\frac{F_x}{EI} \sin \theta(s) \quad (3.4)$$

which is subject to the following two boundary conditions

$$\left. \frac{d\theta(s)}{ds} \right|_{s=L} = -\frac{eF_x \cos(\theta(L))}{EI}, \quad \theta(0) = 0 \quad (3.5)$$

For any given internal load F_x , $\theta(s)$ can be obtained by solving Eq.(3.4). And the joint angle of the compliant nanostructure is

$$\phi = \pi - 2\theta_0 \quad (3.6)$$

By using the geometric relationship $\frac{dx(s)}{ds} = \cos \theta(s)$ and $\frac{dy(s)}{ds} = -\sin \theta(s)$ the position of point A(x_A, y_A) can be calculated as

$$x_A = a = \int_0^L \cos(\theta(s)) ds + e \cos(\theta_0 - ' 2) \quad (3.7)$$

$$y_A = -\int_0^L \sin(\theta(s)) ds + e \sin(\theta_0 - ' 2) \quad (3.8)$$

The strain energy stored in the beam is

$$E_{beam} = \int_0^L \frac{M^2(s)}{2EI} ds = W_{ex} \quad (3.9)$$

W_{ex} represents the work done by the loads applied to the beam, here it is equal to the work done by the force F_x . The total energy in the whole dsDNA layer in the compliant joint is two times E_{beam} .

In the next sections, cylinder model is used for determining the bending stiffness EI of the compliant segment (joint).

3.4.2. Quantify the bending stiffness

Assuming the cylinder model used for dsDNA strands is isotropic and the mass is uniformly distributed, the elastic modulus of dsDNA, E_{DNA} , can be quantified by

$$E_{DNA} = \frac{L_p k_B T}{I_{DNA}} \quad (3.10)$$

I_{DNA} is the area moment of inertia of a dsDNA helix. Approximating the dsDNA as a cylinder, I_{DNA} is equal to $\frac{\pi D^4}{64}$ where D is the diameter of the cylinder. k_B is Boltzman's constant, and T is the absolute temperature. At room temperature $k_B T = 4.1 pN \cdot nm$.

In the design, dsDNA strands are placed adjacent to each other in parallel. The behavior of half beam will be similar to the beam model introduced above (Figure 3.5b, c). The area moment of inertia of the beam segment, I_{6hb} , can be calculated using the parallel axis theorem as:

$$I_{6hb} = 6(I_{DNA} + \frac{\pi D^2}{4} \times (h)^2) \approx 23 nm^4 \quad (3.11)$$

and the bending stiffness, BS , is then:

$$BS = E_{DNA} I_{6hb} \approx 2.46 \times 10^3 \text{ pNnm}^2 \quad (3.12)$$

Substituting stiffness BS in Eq.(3.12) for EI into the Eq.(3.4) gives the relationship between the internal force F_x and deformation that can be solved numerically with the ordinary differential equation solver in Mathematica.

In the next sections, the WLC model is used to determine the internal load F_x of ssDNA springs and use the

3.4.3. Theoretical model of entropic tension of the ssDNA springs

The WLC model[54] is used to calculate the inward force of the ssDNA springs,

$$F_{WLC}(L_C, x) = \frac{k_B T}{L_P} \left[\frac{1}{4 \left(1 - \frac{x}{L_C}\right)^2} - \frac{1}{4} + \frac{x}{L_C} \right] \quad (3.13)$$

Here x is the extension of the ssDNA springs, and L_C is the contour length of the ssDNA springs.

Due to the honeycomb structure, the end-to-end distance of the three upper ssDNA springs of the bottom layer are not the same lengths as the three lower ssDNA springs in the bottom layer (Figure 3.5(a)) in the deformed configuration. In order to balance the length of the six springs, the upper three are 14 bases longer than the lower three except in the last design version, and 10 extra dsDNA base pairs extend from the arms at the connection points of the three lower ssDNA springs to guarantee be consistent with the

DNA helical structure. The lengths of the six ssDNA springs are summarized in Table 3.1.

The force of each of the lower three ssDNA springs can be calculated as

$$F_1 = F_{WLC}(L_{C1}, x) = \frac{k_B T}{L_P} \left[\frac{1}{4 \left(1 - \frac{x}{L_{C1}} \right)^2} - \frac{1}{4} + \frac{x}{L_{C1}} \right] \quad (3.14)$$

Here x represents the extension of the lower three ssDNA springs on the bottom layer. According to the beam model, x is also equal to $2a$, where a is horizontal coordinate of the end of the beam described by Eq.(3.7). L_{C1} is the contour length of the ssDNA springs. Version 1, where the length of the ssDNA springs is zero, is omitted from the following analysis.

Similarly, the force of each of the upper three ssDNA springs can be calculated using the equation:

$$F_2 = F_{WLC}(L_{C2}, x + 10L_b) = \frac{k_B T}{L_P} \left[\frac{1}{4 \left(1 - \frac{x + 10L_b}{L_{C2}} \right)^2} - \frac{1}{4} + \frac{x + 10L_b}{L_{C2}} \right] \quad (3.15)$$

where the term $10L_b$ is due to the additional extension in the upper three ssDNA springs equal to the extra 10 dsDNA base pairs in the lower three ssDNA springs. L_{C2} is the contour length of the upper three ssDNA springs.

The total force of all six ssDNA springs is:

$$F_{ssDNA} = 3(F_1 + F_2) \quad (3.16)$$

And the energy stored in the ssDNA springs can be obtained by calculating the integral of the total force on the interval from zero up to the extension of ssDNA springs:

$$E_{ssDNA} = \int_0^{\Delta x} F_{ssDNA} dx \quad (3.17)$$

The results are plotted in Figure 3.1(d). The red curve represents the force needed to bend the beam according to the beam model to obtain the corresponding extension of ssDNA, which can be derived from the horizontal position of point A; the other four curves (from left, black curve, to right, blue curve) represent the total force vs. extension of the ssDNA springs in design versions 2 to 5 respectively. All the basic parameters used in the calculations are presented in Table 3.2.

Table 3.2: Basic parameters used in the analytical model.

Symbol	Parameter	Values
D	Diameter of dsDNA strands	2.5 nm
L_b	Length of one base pair ³	0.337 nm (dsDNA)
	Length of one base	0.65 nm (ssDNA)
L_0	Nominal length of the beam	$84L_b = 28.31$ nm
L_P	Persistence length	50 nm (dsDNA)
		2 nm (ssDNA)
e	Offset distance of ssDNA springs to the joint	$3.25D = 8.125$ nm
R	Radius of dsDNA	$D/2 = 1.25$ nm
h	Vertical offset from centroid	$D/4 = 0.625$ nm

Table 3.3: Equilibrium angles obtained from experiment and analytical model.

Design	ϕ (prototype samples)	ϕ (beam model)
Version 1(0 bases)	56.5°	N/A
Version 2(11 bases)	70.2°	59.8°
Version 3(32 bases)	97.9°	94.4°
Version 4(53 bases)	110.0°	115.6°
Version 5(74 bases)	128.2°	126.0°

Table 3.3 shows five versions of the compliant nanostructures, which are designed to deform to different joint angles ϕ . It also shows the equilibrium value of the joint angle ϕ , calculated from the theoretical model and measured by TEM. From Table 3.3, we can also conclude that the theoretical beam model agrees well with the experimental results for the large joint angle versions 3, 4, 5 with the percentage error being 3.7%, 5.4% and 1.5% respectively. While for the small joint angle version 2, the error 15.2% is relatively high.

3.4.4. Evaluating and predicting compliant joint stiffness

The deformation of the compliant joint is defined in terms of the end-to-end distance of the ssDNA springs, r ($r = 2a$ in Figure 3.6(a)). The minimum energy configuration of the springs occurs at $r = 0$, and the minimum energy configuration for the 6-helix layer

occurs when r is equal to the length of the 6-helix layer, L_0 . The total energy of the compliant joint, $U(r)$, is obtained by summing the energy of the springs in the 6-helix layer (Figure 3.6(c)) and the energy stored in the bent beam.

$$U(r) = E_{beam} + E_{ssDNA} \quad (3.18)$$

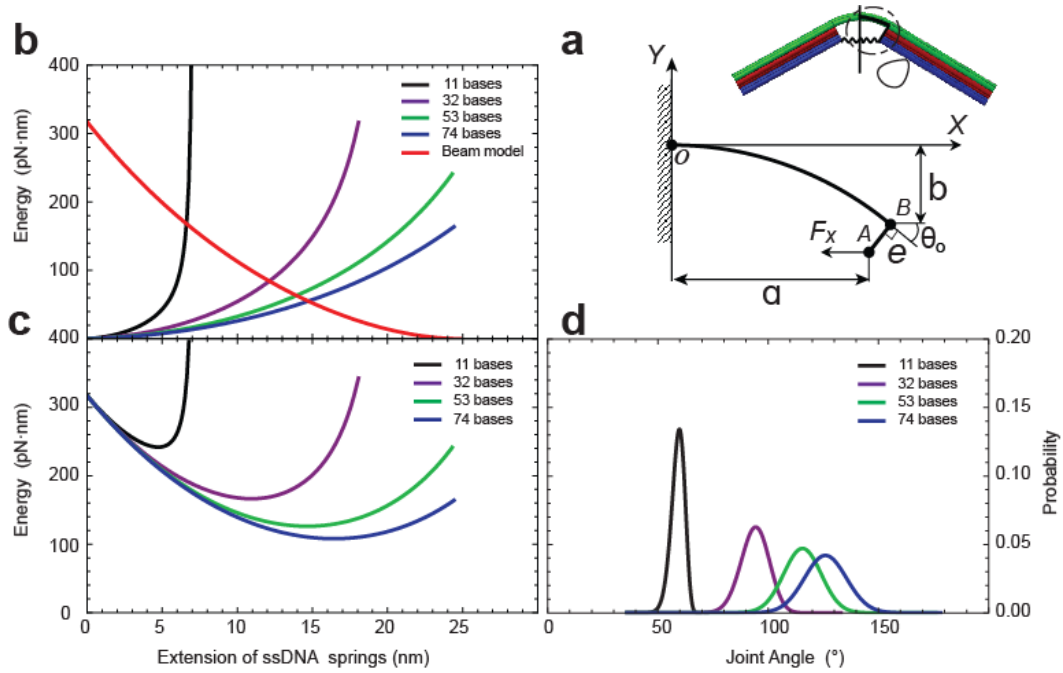


Figure 3.6: Theoretical model of the compliant joint. (a) Beam model of the curved segment. (b) Energy stored in the 6-helix layer (red). (c) The total energy of the compliant joint. (d) Boltzmann distribution of the thermal fluctuations in angle.

Based on the relation between ϕ and a described by Eq.(3.6) and (3.7), $U(\phi)$ could be easily obtained. The equilibrium angle of the compliant joint occurs at the minimum total energy configuration. The equilibrium angles calculated from the analytical model were

59.8°, 94.4°, 115.6°, and 126.0° for the 11, 32, 53, and 74 base long ssDNA springs respectively.

Due to thermal fluctuations, the compliant joint will fluctuate about this equilibrium position. The magnitude of the thermal fluctuations is proportional to the stiffness of the joint. Angular distributions (Figure 3.6(d)) were calculated from the analytical energy landscapes of the compliant joint (Figure 3.6(4)) using Boltzmann distribution, $P(\phi) = \exp(-U(\phi)/k_bT)/Z$, where k_b is Boltzmann's constant, T is the absolute temperature, and Z is the partition function defined as $Z = \int_{-\infty}^{\infty} \exp(-U(\phi)/k_bT) d\phi$. The angular distributions are wider for longer ssDNA springs, which is consistent with the angular distributions shown in Figure 3.4. This implies that the torsional stiffness of the compliant joint decreases while the joint angle increases.

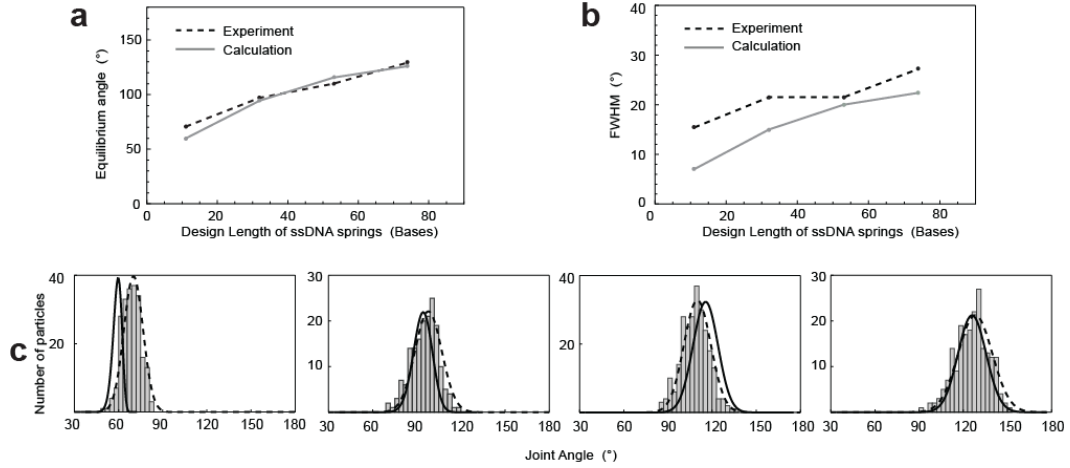


Figure 3.7: Theoretical model captures angular distribution. (a) The analytical model and (b) the trend of increasing width, characterized by the FWHM. (c) Analytical energy landscape captures the asymmetry of the experimental distributions.

Figure 3.7 compares the equilibrium angles predicted by the analytical model to the maximum angles from the experimental distributions. Note that the model is purely predictive and does not contain any fitting parameters. Figure 3.7(b) compares the full-width at half of the maximum value (FWHM) calculated from the analytical energy distributions to the FWHM of the experimental distributions. Figure 3.7(c) compares the full distributions. The full angular distribution (black), calculated using a Boltzmann distribution of the analytical energy landscape, also captures the asymmetry of the experimental distributions (gray). Gaussian fits are also shown in dashed black. Even without any fitting parameters, the theoretical model captures the trend of increasing thermal fluctuations with longer ssDNA springs and also captures the asymmetry of the angular distributions, which results from the asymmetric energy landscape (Figure 3.6(c)).

3.4.5. Modeling of tunable mechanical properties

In order to estimate the torsional stiffness of the compliant joint, it can be approximated as a linear torsional spring that follows the equation $T = \kappa \Delta\theta$, where $\Delta\theta$ is the change in angle from the equilibrium angle, κ is the torsional stiffness, and T is the torque required to deform the angle by $\Delta\theta$. In this case, κ can be related to thermal energy by the theorem of equipartition of energy as $\kappa \langle \Delta\theta^2 \rangle = k_b T$. Based on the joint angle variance, $\langle \Delta\theta^2 \rangle$, calculated from experimental distributions, torsional stiffness is determined ranging from 107 pN·nm/rad for the longest ssDNA spring up to 367 pN·nm/rad for the shortest ssDNA spring. These results indicate that we can design compliant joints with torsional stiffness similar to or stiffer than actin binding proteins such as Arp 2/3 (~80-

130 pN.nm/rad) [68] or Filamin (~50 pN.nm/rad) [69]. Since the persistence length of DNA origami nanostructures is also tunable over several orders of magnitude up to $>\mu\text{m}$, DNA origami could ultimately be used to design biomaterials with mechanical behavior similar to cross-linked actin networks [70–72].

The geometry and stiffness of a DNA origami compliant joint can be tuned with a novel approach of locally shifting single-stranded scaffold DNA within the structure. By this parameter alone, the geometry and stiffness cannot be controlled independently. Longer ssDNA springs results in larger joint angles with lower torsional stiffness. However, the model includes additional design parameters, specifically the length and bending stiffness of the stiff component, here a layer of 6 dsDNA helices. By cooperatively adjusting the three design parameters of the compliant joint (length of stiff dsDNA segment, bending stiffness of the stiff dsDNA segment, and length of ssDNA springs), both the bending stiffness and the joint angle could be independently designed. For example, the theoretical model predicts that an 8-helix layer as the stiff segment with 28 base long ssDNA springs would give a similar equilibrium joint angle but narrower distribution to the 6-helix layer with 32 bases (Figure 3.8(a)). Similarly, different joint angles with the same stiffness can be achieved by cooperatively varying the bending stiffness of the top layer (i.e. number of helices) and the length of the ssDNA springs (Figure 3.8(b)). Tuning the properties of the stiff segment, unlike adjusting the length of the ssDNA springs, would require designing a new structure. But the analytical model presented here could be used as tool to guide the design of compliant joints with a wide range of joint angles and torsional stiffness.

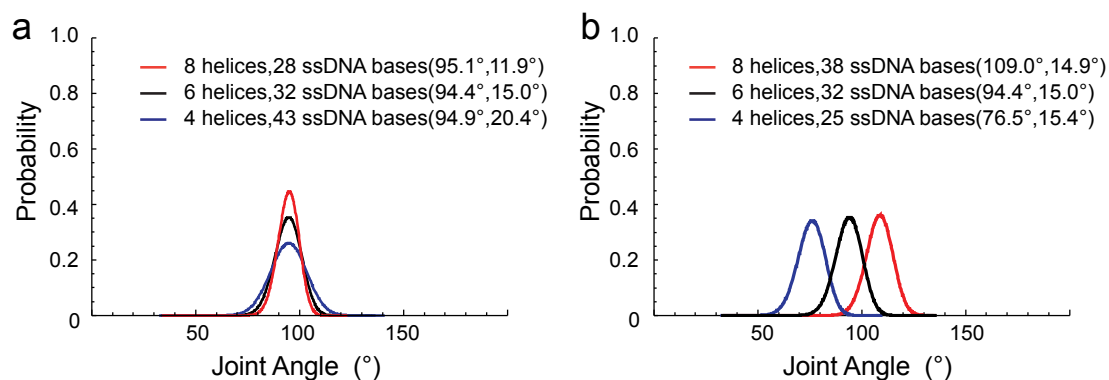


Figure 3.8: Designing joint angle and stiffness with the theoretical model. (a) Predict the width of the joint angle distribution and (b) control the equilibrium angle.

As the model can well predict the behavior of mechanically functional DNA origami nanostructures, probability of reliability still needs comprehensive study. A range of values have been reported in previous literature for some of the parameters used in the model including the length of a ssDNA base [73–75], the persistence length of ssDNA [53,76], the length of a dsDNA base pair [10,52,77], and the persistence length of dsDNA [52,78–80] and the offset distance e . Therefore, the sensitivity of the model to these parameters were checked (Figure 3.9). Variation in the length of ssDNA or dsDNA had minimal effect. Variation within the reported range of values of the persistence length of ssDNA and dsDNA, which largely determine the stiffness parameters in the model, both caused similar variations of $\sim 10^\circ$ - 15° in joint angle and $\sim 2^\circ$ - 4° in FWHM. The offset distance of ssDNA springs from the curved segment also results in a higher sensitivity to the equilibrium angle due to its influence on the moment applied to the curved segment.

While the numerical results are somewhat sensitive to the values used, the qualitative trends and conclusions drawn are not.

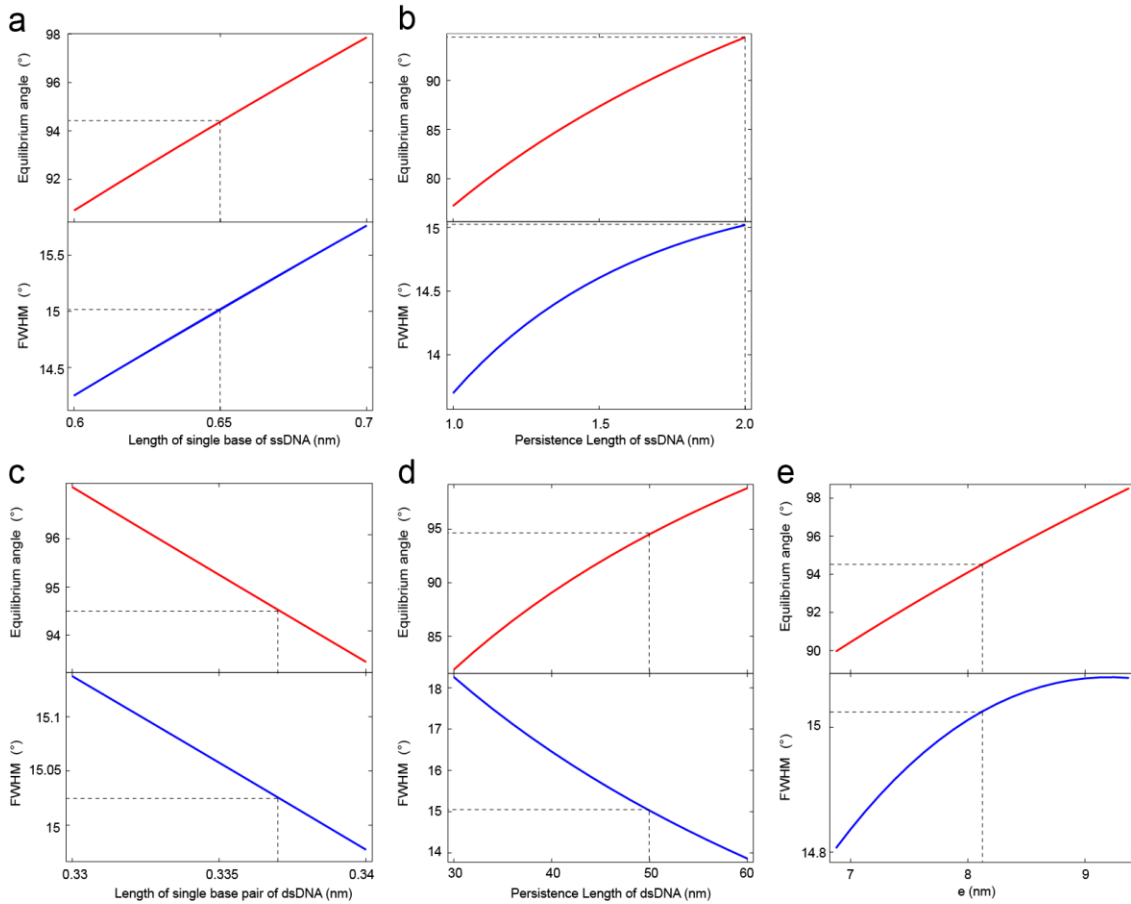


Figure 3.9: Sensitivity analysis. (a) the length of a ssDNA base, (b) the persistence length of ssDNA, (c) the length of a dsDNA base pair, (d) the persistence length of dsDNA and (e) the offset distance e .

3.5. Pseudo-rigid-body model of DNA origami compliant joint

The Pseudo-rigid-body model of the DNA origami compliant joint is shown in Figure 3.10. The compliant segment has a length of $L_0=28.56$ nm or 84 base pairs. The other two dimensions are $L_1=54.74$ nm, $L_2=59.5$ nm and $H=8.125$ nm.

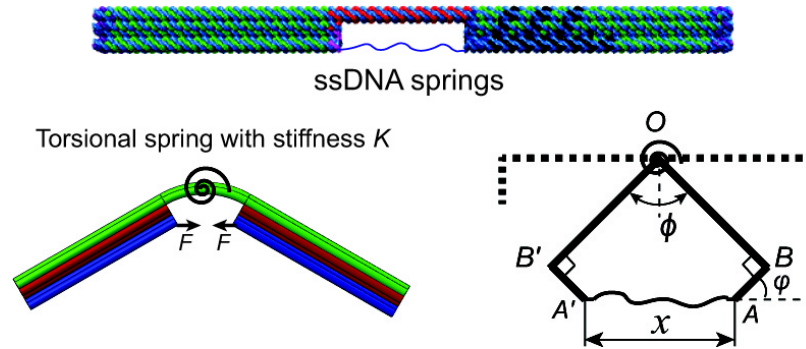


Figure 3.10: PRBM of the CDOM hinge joint.

The deformed configuration of the compliant joint is shown at the bottom of Figure 3.10. Here, the direction and position of the force F added in the 3D model is chosen for our specific design. For general application, the actuation force has no specific location and direction requirements. Because the compliant segment is not very long, it is reasonable to model the compliant joint as a hinge joint with a torsional spring according to PRBM. The torsional spring with stiffness K is placed at the middle of the compliant segment (bottom right of Figure 3.10) and each side is modeled as rigid link. The key point is to find the accurate value of K which depends on the stiffness of dsDNA helix,

the inertial moment of the cross section, and the loading condition. However, the loading condition and the bending stiffness can be affected by the solution condition and temperature. Here, the torsional spring stiffness is given by

$$K = c \frac{EI}{L} \quad (3.19)$$

where c is a correction coefficient, EI and L are the bending stiffness and the length of the compliant segment respectively. We will calibrate the coefficient c using experimental data.

In order to bend the compliant joint, we intentionally left six ssDNA strands (called ssDNA springs) on the bottom layer at the corresponding position of the compliant segment (top of Figure 3.10). The ssDNA strands act like springs where the force is generated due to their entropic elasticity. The force introduced by the ssDNA springs can bend the compliant joint. Shorter ssDNA springs will stretch more, and accordingly a larger force will result in a smaller angle between the two bars. Four design versions with different lengths of ssDNA springs were fabricated and analyzed here.

The six ssDNA springs can be divided into two groups, the upper three and the lower three springs (Table 1). Due to local geometric constraints, the upper three springs are slightly longer than the lower and their end-to-end distance is 3.4 nm longer.

Based on the Eq. (3.13) of Worm-like chain model, the resultant force of the ssDNA springs is

$$F_{SS} = F_1 + F_2 = 3F_{WLC}(L_{C1}, x) + 3F_{WLC}(L_{C2}, x + 3.4) \quad (3.20)$$

Here, L_{C1} and L_{C2} are the contour lengths of the two groups of ssDNA springs.

The equilibrium angle of each design version corresponds to the minimum energy configuration of the compliant joint, which can be determined by the following optimization,

$$\begin{aligned} \min_{\phi \in [0, \pi]} E_0(\phi, x) &= \frac{1}{2} K(\pi - \phi)^2 + \int_0^x F_{SS} dx, \\ \text{s.t. } L_0 \sin(\phi / 2) - 2H \cos(\phi / 2) - x &= 0 \end{aligned} \quad (3.21)$$

The geometric constraint equation is derived from the geometry in the bottom right of Figure 3.10.

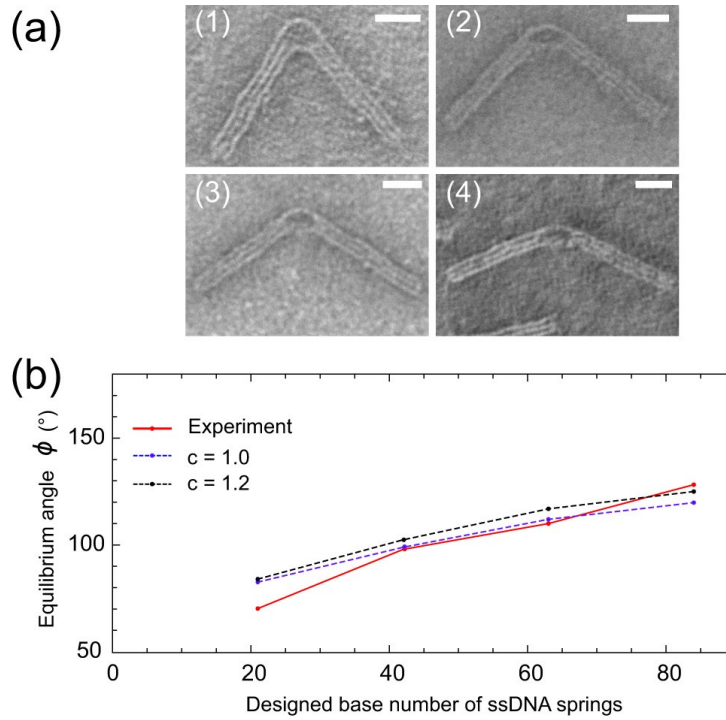


Figure 3.11: (a) TEM images of CDOM hinge joint and (b) comparison of experiment and model results, scale bar = 20 nm.

The experiment results presented in [39] are referred here in Figure 3.11(b). It seems that when the stiffness correction factor c nears 1.0 and 1.2, the PRBM results are close to the experimental results.

3.6. Materials and methods

3.6.1. Producing ssDNA scaffold

The scaffold used in this work is a 7,560 base clone of the M13MP18 bacteriophage virus. The scaffold was produced by following protocols detailed in Castro et al.[22].

3.6.2. DNA origami structure design and fabrication

The structure and staple sequences were designed using the DNA origami computer aided design software caDNAo [55], and fabricated using a 7,560 base clone of the single-stranded M13MP18 bacteriophage viral genome⁵ and 160 single-stranded staples that were ordered from a commercial vendor (Eurofins, Huntsville, AL). Five versions of the compliant joint with varying geometry were designed by varying the length of ssDNA springs. These versions had 0, 11, 32, 53, and 74 ssDNA bases in the springs respectively, which was achieved by changing only the staples positioned between the ssDNA springs and the loops (~15% of total staples). For self-assembly, scaffold was mixed at 20 nM with staples at 10-fold excess (each staple at 200 nM) in a folding reaction containing 5 mM Tris, 5 mM NaCl, 1 mM EDTA, and 14-20 mM MgCl₂ (MgCl₂ concentrations in this range produced similar folding results). The folding reactions was subjected to a thermal annealing ramp where the temperature was quickly increased to 65 °C and then slowly cooled down to 4 °C over a timescale of two and half days.

3.6.3. Structure purification and imaging

DNA origami structures were purified by agarose gel electrophoresis. Gels were mixed with 2% agarose in 0.5× TBE buffer (44.5 mM Tris-borate, 1 mM EDTA) with 11 mM MgCl₂ and 1 μM ethidium bromide. Folded structures were mixed with 6× loading dye (New England Biolabs, Ipswich, MA) and run for approximately 4 hours at 70 V. Structure bands were excised and removed from agarose using freeze and squeeze extraction DNA gel extraction spin columns (Biorad, Hercules, CA). To verify proper folding, purified structures were prepared for transmission electron microscopy (TEM) imaging for structural feedback as described in Castro et al. [22] Briefly, 4 μl of purified structure solution was deposited on a plasma treated formvar coated TEM grid stabilized with evaporated carbon film (Electron Microscopy Sciences, Hatfield, PA) and incubated for four minutes. The structure solution was wicked away, and structures were negatively stained by applying a 20 μl drop of 2% Uranyl formate (SPI, West Chester, PA), incubating for 40 seconds, and then wicking off the stain solution. Sample grids were allowed to dry for at least 30 minutes prior to imaging. Images were taken on a FEI Tecnai G2 Spirit TEM at an acceleration voltage of 80 kV.

3.7. Summary

The geometry and mechanical properties of the compliant joint are determined by a balance of tension in flexible ssDNA components and bending in structurally well-defined dsDNA bundles. In addition, a novel approach is developed to tune the geometry and mechanical properties of the DNA nanostructure by introducing ssDNA scaffold loops that functioned as a reservoir to add or remove length from the ssDNA springs.

Five different structures with joint angles ranging from 56.5° to 128.2° were achieved simply switching out a small subset (15%) of the overall number of staples.

In order to quantitatively understand the behavior of the compliant joint, an analytical model is developed that combined a beam model and an entropic model (WLC) of the stiff (dsDNA bundle) and flexible (ssDNA) segments, respectively, of the compliant joint. This analytical model closely captured the equilibrium joint angles and the angular distributions resulting from thermal fluctuations of the four design versions with appropriate lengths of ssDNA. The analytical model also captured the trend of increasing magnitude of thermal fluctuations with longer ssDNA springs, indicating that the stiffness of the compliant joint is also tunable. To test the validity of the model, a simple alternative is explored, using a torsional spring to replace the beam description in the compliant joint model. The results show the beam model better predicts the experimental results over the entire range of designs.

It is the first demonstration of a compliant (deformable) DNA origami nanostructure with geometry and stiffness that can be designed according to a theoretical micromechanical model. The approach presented here establishes a foundation to design and fabricate DNA-based devices with mechanically functional components such as springs, joints, or actuators. Ultimately, compliant components like the ones presented here can form the basis of compliant mechanisms that can be applied as nanomechanical devices with controllable motion.

Chapter 4: Direct Design of an Energy Landscape with Bistable DNA Origami

Mechanisms

As the fabrication of basic compliant DNA origami joints have been fabricated, much more complex compliant mechanisms can be fabricated by structural DNA nanotechnology. In this chapter, it is demonstrated that DNA origami is a feasible technique for the design and fabrication of complex mechanisms even exhibiting controllable dynamic behavior. In last chapter, compliant hinge was designed and fabricated. Here based on the implementing macroscopic engineering design approaches to construct DNA origami mechanisms (DOM) with programmable motion and tunable flexibility, the design of compliant DNA origami mechanisms is implemented to extend from prescribing motion to prescribing an energy landscape. Compliant mechanisms facilitate motion via deformation of components with tunable stiffness resulting in well-defined mechanical energy stored in the structure. Specifically, a DNA origami nanostructure is designed, fabricated, and characterized and its energy landscape is defined by two stable states (local energy minima) separated by a designed energy barrier. This nanostructure is a four-bar bistable mechanism with two undeformed states. Traversing between those states requires deformation, and hence mechanical energy

storage, in a compliant arm of the linkage. The energy barrier for switching between two states was obtained from the conformational distribution based on a Boltzmann probability function and closely follows a predictive mechanical model. Furthermore, the ability is demonstrated that to actuate the mechanism into one stable state via additional DNA inputs and then release the actuation via DNA strand displacement. This controllable multistate system establishes a foundation for direct design of energy landscapes that regulate conformational dynamics similar to biomolecular complexes.

4.1. Background

Structural DNA nanotechnology[12,13,81,82] has enabled the precise design of 2D and 3D static and dynamic structures including smiley faces[19,83], twisted and bent bars[21], spheres[26,84], linkages with complex motion[30], and nanorobots[45,59,85,86]. Recent studies have demonstrated promising applications that utilize DNA origami nanostructures as templates to organize proteins[83] or nanoparticles[87,88] in 2D and 3D space, vehicles for drug delivery[24,45,89], nanopores[28,90,91], and biosensors[92,93]. Although the majority of DNA nanostructure applications utilize objects with static geometry, important strides have been made to design dynamic DNA devices (i.e. DNA nanomachines). Early DNA nanomachines[14,15,61] involved configurations of DNA strands that could be triggered to undergo conformational changes, usually via DNA strand displacement[18], to achieve, for example rotational[94] or translational motion[95] or even measure molecular binding energies[96]. The development of scaffolded DNA origami[19,20,22] enabled greater control over geometry and stiffness of nanostructure components, which

has expanded the possibilities to design complex mechanical behavior. Furthermore, in recent years design[55] and analysis tools[22,38,42,97] have sped up the development DNA-based design and enabled consideration of properties beyond geometry, such as stiffness, which play a critical role in the function of some DNA origami devices[98]. Prior work to quantify and design the mechanical behavior of DNA origami nanostructures has revealed that they exhibit mechanical deformations such as bending, stretching, and compression[25,39,44], similar to macroscopic structures. Here this mechanical behavior is exploited to design a nanomechanism with a prescribed energy landscape consisting of multiple stable states separated by an energy barrier [40].

In typical engineering design, components gain mobility via kinematic joints, which allow constrained motion between two rigid parts. For example, a revolute joint, which allows relative motion in one rotational degree of freedom, can be constructed by connecting two links with a pin. These joints can be combined to create mechanisms with complex motion. Borrowed from the classical engineering field, the term mechanism is defined as a collection of rigid components, individually called “links”, connected by kinematic joints. Recently, DNA origami mechanisms (DOM) can be constructed by connecting stiff double-stranded DNA (dsDNA) bundles at joints formed by flexible single-stranded DNA (ssDNA) connections[30]. However, in the absence of actuation, these dynamic structures are subject to thermal fluctuations resulting in random configurations along the constrained motion path since they utilize very flexible ssDNA components.

An alternative methodology to develop systems with controlled motion is compliant mechanism design[32,50], which integrates rigid components with high stiffness, and deformable, or compliant components with relatively lower stiffness. The compliant components can either comprise a lower stiffness material or the same material with a smaller moment of inertia resulting in a lower bending stiffness. With DNA origami nanotechnology, rigid, compliant and flexible components can be respectively designed as bundles of many dsDNA helices, bundles of fewer dsDNA helices, and short ssDNA polymers. Then motions in DNA origami mechanisms with compliant component can be facilitated not only by flexible ssDNA[30] but also by deformation of compliant dsDNA helices. Also, the DNA origami mechanism that obtains its mobility based on the deformation of its compliant component is named compliant DNA origami mechanism (CDOM). The use of compliant components affords greater control over nanoscale thermal fluctuations and also allows for direct consideration of the energy landscape governing dynamic behavior through mechanical design (i.e. designing geometry and stiffness).

4.2. Design of Four-bar Bistable DNA Origami Mechanism

Here, stiff, compliant, and flexible components are integrated to construct a compliant DNA origami mechanisms with two stable positions (local energy minima) separated by an energy barrier that results from mechanical strain energy stored in a compliant component. Similar macroscopic engineering systems are referred to as bistable. A simple example of a macroscopic bistable mechanism is a compliant straight beam that has buckled to one side (one stable position) under an axial compressive force. When a

transverse load is applied, the beam can undergo a “snap-through” transition to the other side (second stable position) if the work input is larger than the energy barrier. Figure 4.1(a) shows a beam is buckled to the upper stable equilibrium configuration (solid line) by a load P on the two ends. It can then snap to the other stable configuration (dashed line) after applying a downward force F . Figure 4.1(b) illustrates a 3D model of a bistable compliant four-bar mechanism is shown. One end of the compliant link (red) is fixed on the frame link (blue) and the other end is connected with the coupler link (cyan) with a revolute joint. S2 and S1 are the two stable equilibrium positions of this bistable mechanism.

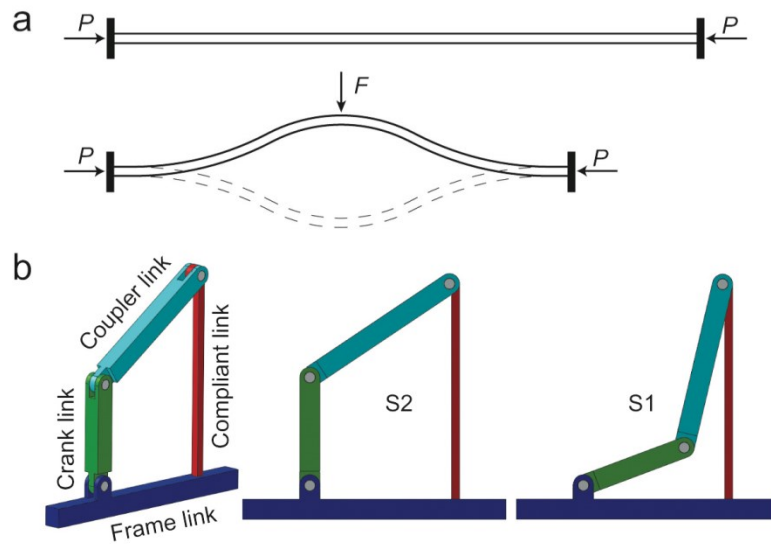


Figure 4.1: A bistable beam and a bistable compliant four-bar mechanism.

The bistable nanomechanism designed here is conceptually similar to this buckled beam example. The design is based on a bistable four-bar mechanism consisting of three relatively rigid links (blue, green, and cyan in Figure 4.2) and one compliant link (red in Figure 4.2). Analogous bistable four-bar mechanisms have previously been implemented in MEMS applications[99,100]. Here the three relatively stiff links consist of a 10 helix bundle (hb), and the compliant link is a 6-hb of dsDNA. At either end of the compliant 6-hb, the cross section is increased to a 10-hb to allow appropriate attachment to other components. These four components are connected into a closed loop with flexible hinge connections at three corners (bottom left, top left, and top right in Figure 4.2) and one fixed connection at the fourth corner (bottom right in Figure 4.2). The hinges are formed by two ssDNA connections 2 or 4 nt long. Additional longer ssDNA connections at the hinges influence the flexibility of the device.

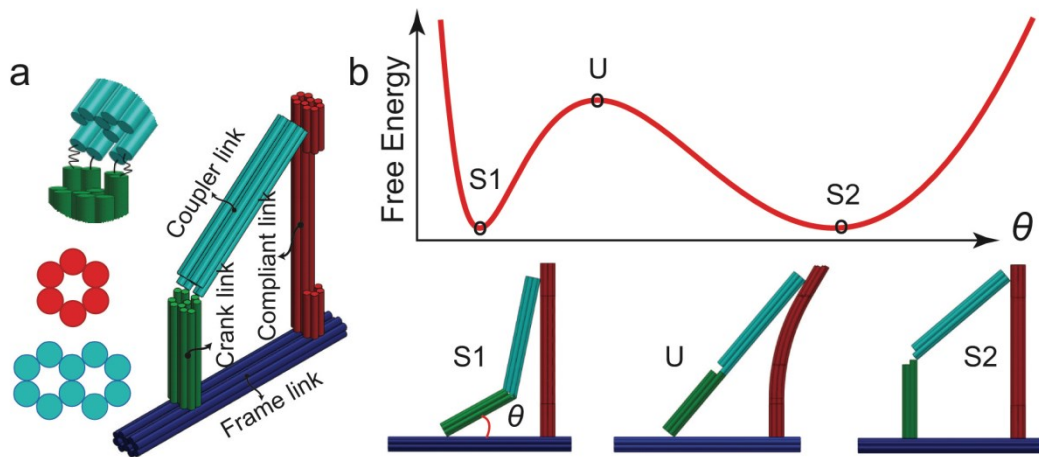


Figure 4.2: Design sketch and stable equilibrium configurations of the bistable nanomechanism. (a) 3D model. (b) Energy variation of this nanomechanism.

Energy variation of this nanomechanism is mainly determined by the deformation of the compliant link, which results in two stable equilibrium configurations (S1 and S2) where there is no deformation of the compliant link and one statically unstable equilibrium configuration (U) where the compliant link reaches its maximum deformation.

The short green link on the left side can be viewed as the input, or crank link for the mechanism. The two stable positions (Figure 4.2(b), bottom) correspond to configurations where the crank link is either at a small angle relative to the frame link (S1) or in a vertical position (S2). Traversing between the two stable positions requires deformation of the mechanism, which largely occurs in the compliant link since it has the lowest stiffness. When the crank and the coupler links are collinear, the compliant link reaches its configuration of maximum deformation (U) and maximum energy. The strain energy stored in the compliant link at this maximum deformation is the energy barrier for the bistable mechanism. In both stable positions, the compliant link is undeformed. The energy landscape of the bistable mechanism can be determined by considering the mechanical deformation of the compliant link. Figure 4.2(b) illustrates the bistable mechanism energy landscape as a function of the crank angle, θ .

In this particular design, the crank link (green), coupler link (cyan) and frame link (blue) have 10-hb cross section organized in honeycomb lattice and lengths of 39.78, 61.88, 92.82 nm, respectively. The red compliant link (red) is constructed by three segments. The end segments are 16.66 nm in length with a 10-hb cross section, and the middle segment, which is the actual compliant component, has a 6-hb cross section 54.74

nm length. For the three hinge connections, the hinge axis is defined by two ssDNA scaffold connections. At the hinges that form inner angles $\lesssim 90^\circ$ (bottom left and top right in Figure 4.2) these scaffold connections are 2 nucleotides (nt) long. At these hinges, the scaffold is at the appropriate helical location closest to the hinge vertex. The third hinge (top left in Figure 4.2(a)) forms an inner angle that is straight (180°) in the unstable position, greater than 180° in the S1 configuration, and less than 180° in the S2 configuration. Since there is a potential for interference between the helices at this hinge, the connections were made slightly longer (4 nt). At each hinge there are also two longer ssDNA connections (Figure 4.2(a) top left). These connections do not define the hinge axis; however they may affect the motion of the mechanism due to entropic elasticity, steric effects, and electrostatic interactions. The fixed right angle connection (fixed joint) was designed by routing scaffold from the bottom end of the compliant link directly into cross-over junctions on the top side of the frame link. With this design, the configurations S1, U, and S2 correspond to crank angles of $\theta = 29^\circ$, 49° , and 90° (θ defined in Figure 1b, bottom), respectively.

4.3. Experiment results

4.3.1. Initial data

The DNA origami bistable mechanism was self-assembled from a single ssDNA scaffold obtained from the M13MP18 bacteriophage virus genome and 189 staples via molecular self-assembly and then purified via agarose gel electrophoresis (see Materials and Methods). Figure 4.3(a) shows Gel purification image, from left to right are 1kb

DNA reference ladder, the scaffold, the bistable nano-mechanism folded at 14, 16, 18, 20 mM MgCl₂ in a 4.5 days annealing ramp. Figure 4.3(b, c) present typical TEM images of the assembled bistable structures, scale bars are 50 nm. All of the angle measurements were conducted in ImageJ and the standard derivation of the angle measurement is 1.35° (Figure 4.3(d)).

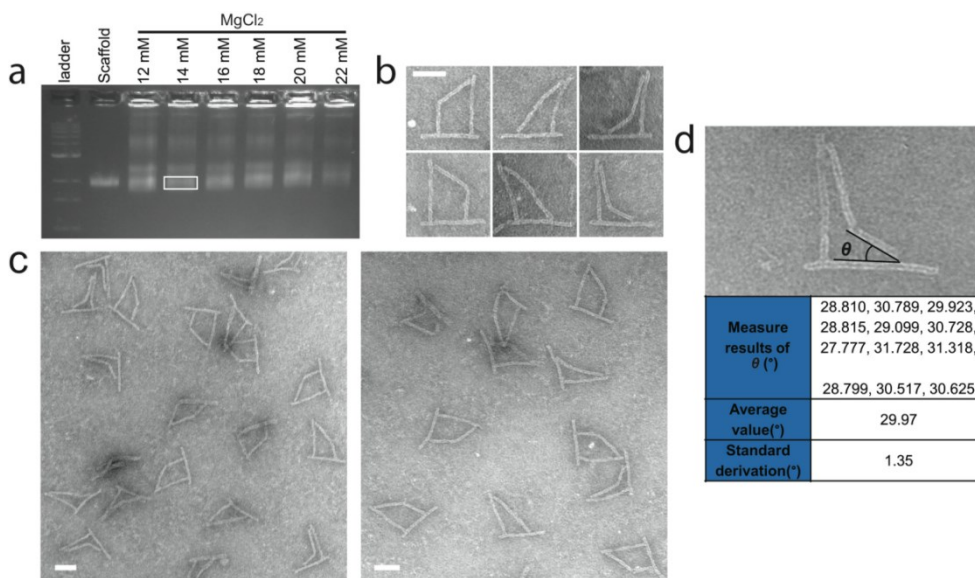


Figure 4.3: Gel purification and TEM images.

TEM images reveal that folded structures adopt both stable configurations and most particles appear at or near the open or closed configurations. Interestingly, some particles appear in the maximum energy configuration (i.e. unstable position, U). This is likely due to base-stacking interactions^{45,46} between the crank link and the coupler link that line up

end-to-end in the unstable position. The deformation of the compliant link can be viewed clearly from particles in this configuration (Figure 4.4(a), middle).

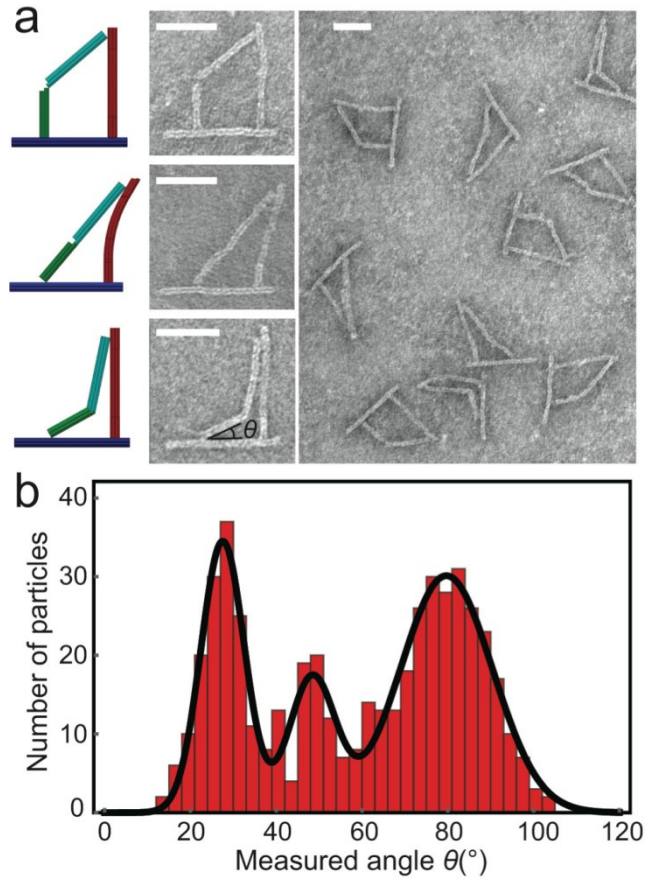


Figure 4.4: TEM experimental results and analysis. (a) Typical TEM images, scale bars are 50 nm. (b) Conformational distribution.

Because the nanostructure is a planar mechanism, 2D TEM images are sufficient to capture the full structure configuration. Figure 4.4(b) shows the configurational distribution of the nanomechanisms (quantified from TEM images) in terms of the angle

θ between the crank link and frame link (sample count $n = 493$). Although the structure may be subjected to some forces during the surface deposition and staining process, variations in the sample prep suggested these forces do not impact the distribution of conformations for this particular structure. The distribution clearly shows the two stable positions of the bistable mechanism and the small population that adopts the unstable configuration. Approximately 31% of the structures adopt the closed configuration ($\theta < 40^\circ$) and ~53% adopt the open configuration ($\theta > 60^\circ$). The fitting function used in the distribution is a combination of three normal distributions, mathematically written as

$$F(x) = \frac{a_1}{\sqrt{2\pi}\sigma_1} \text{Exp}\left[-\frac{(x-\mu_1)^2}{2\sigma_1^2}\right] + \frac{a_2}{\sqrt{2\pi}\sigma_2} \text{Exp}\left[-\frac{(x-\mu_2)^2}{2\sigma_2^2}\right] + \frac{a_3}{\sqrt{2\pi}\sigma_3} \text{Exp}\left[-\frac{(x-\mu_3)^2}{2\sigma_3^2}\right] \quad (4.1)$$

From the multimodal normal distribution fit, the closed population has a peak value at $\theta \approx 27.5^\circ$, the open population has a peak value at $\theta \approx 79.7^\circ$, and the population of particles in the unstable position has a peak value at $\theta \approx 48.4^\circ$. These values are very close to the original design intention except the open stable position is about 10° smaller than the design value of 90° . This deviation is likely due to the mechanics of the ssDNA hinge connections. In the other research, it has been shown that although these types of hinges are quite flexible, they exhibit an equilibrium angle between 60 and 80° .¹⁰ Furthermore, the closed (S1) configuration has a larger stiffness than the open (S2) configuration indicated by the narrower distribution, likely because the S1 configuration is closer to the energy barrier. Hence, small changes of angle θ result in larger energy changes in the S1 configuration compared to the S2 configuration.

The free energy landscape $U(\theta)$ shown in Figure 4.4(b) was determined from the probability density distribution $P(\theta)$, assuming a Boltzmann distribution, $P(\theta) \propto \exp(-U(\theta)/k_B T)$, where k_B is Boltzmann's constant and T is the absolute temperature. Theoretically, the unstable position should correspond to an energy maximum. However, because some particles get stuck in the unstable position, likely due to base-stacking interactions, the small peak on the probability distribution results in a third energy minimum in the free energy landscape. Although this effect is distinct from the mechanical deformation of the compliant link, it still affects the overall mechanical and dynamic behavior of the device.

4.3.2. Actuation analysis

DNA strand displacement^{1,2} is a popular approach to design and control dynamic DNA nanostructures, which is illustrated in Figure 4.5. In this case, in the initial relaxed state (upper left), overhang staples (red) are designed for each of the four links. Initially there is no connection between crank link (green) and frame link (blue), or between the coupler link (cyan) and compliant link (red). The closing staples (green strands) were added and hybridization of closing staples with the red overhangs holds the structure in the closed S1 position (upper middle). The releasing staples (purple strands), which are the full reverse complement of the closing strands, were added to remove the closing strands via DNA strand displacement (upper right). An example of this DNA strand displacement process is shown on the bottom.

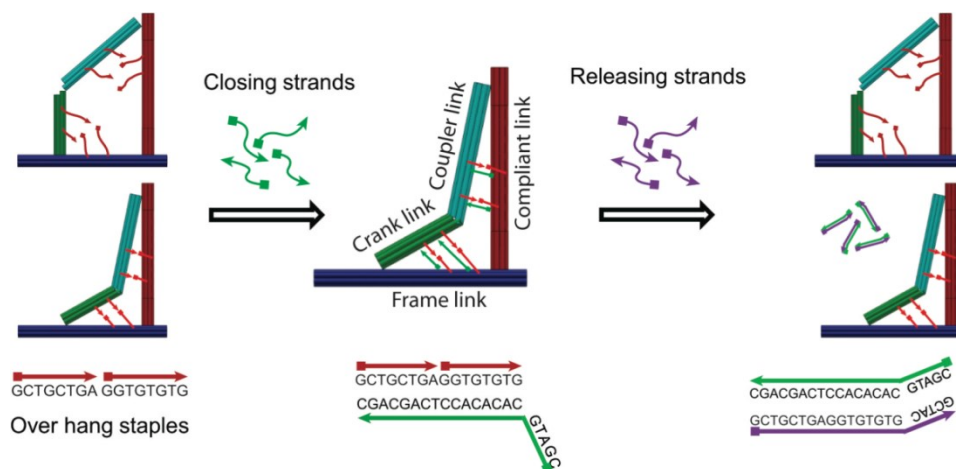


Figure 4.5: Actuation with DNA strand inputs.

To demonstrate control over the configuration of the structure, a distributed actuation approach similar to Marras, et al.'s work¹⁰ is used to transfer and hold all the particles in the S1 state. In this approach, illustrated in Figure 4.6(a), ssDNA input strands added to the purified structure facilitate reconfiguration of the mechanism by binding to ssDNA staple overhangs on adjacent links.

For this bistable mechanism, actuation process utilizes additional ssDNA inputs (closing strands) to fix the structure in the S1 (closed) configuration. The closing strands can then be removed via toehold-mediated DNA strand displacement by adding additional ssDNA inputs (releasing strands), releasing the mechanisms back into the free state. To force the mechanism into the closed configuration (stable position S1), connections were introduced between overhangs on the crank and the frame links and similarly between the coupler and compliant links. These links form a nonzero angle between them in the closed position, and the length of the overhang staples (8 to 23 nt)

was determined accordingly. Five additional bases were added to each ‘closing’ staple to function as a toehold for subsequent strand displacement. All overhang and toehold sequences were optimized to avoid competitive binding to other staples and with the scaffold.

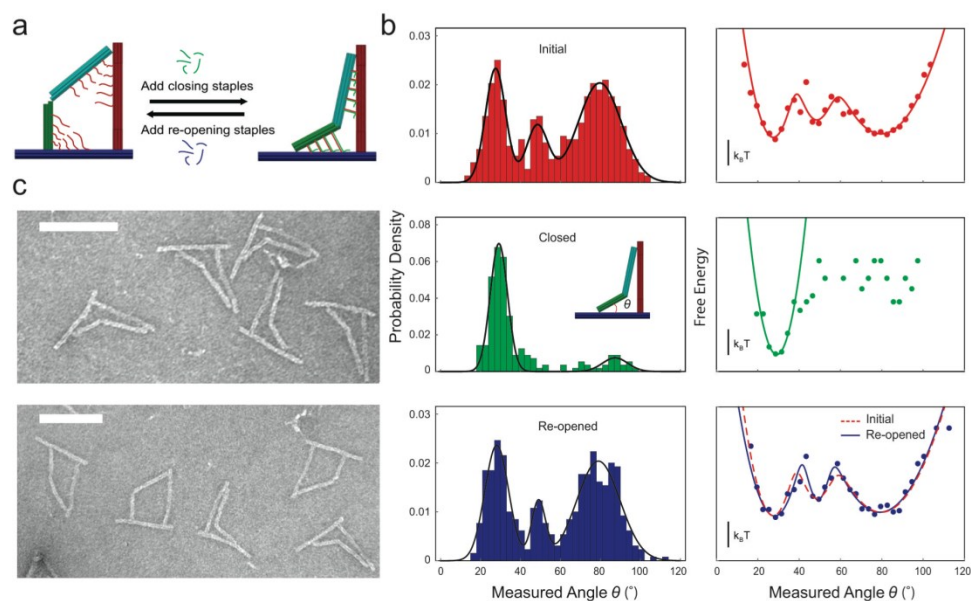


Figure 4.6: Reversible actuation of bistable nanomechanism. (a) Actuation process. (b) Conformational distributions. Scale bars = 100 nm.

Figure 4.6(b) (middle) and 3c (top) depict the angular distribution and representative TEM images after the closing actuation. Approximately 76% of the nanomechanisms were found in the closed (S1) configuration ($\theta < 40^\circ$) compared to 31% prior to actuation (Figure 4.6(b), top, $n = 496$). The energy landscapes are shown on the right of Figure 4.6(b). The open particles were excluded from the energy curve for the S1-actuated

structures because in all likelihood they do not contain the additional connections formed by the input strands and hence are mechanically distinct.

To demonstrate reversible actuation, a second round of ssDNA input strands were introduced, which were the full reverse complement of the closing strands, in order to remove the closing strands via strand displacement. Toehold-mediated strand displacement^{27,47} has been successfully used to actuate a variety of DNA nanostructures.^{22,27,28,48,49} Here DNA strand displacement is used in the context of the distributed actuation approach where the several “closing” strands that hold the structure in the stable position S1 are all displaced to release the structure back into the free state where it can again achieve equilibrium between the multiple conformations. High efficiency of the reverse actuation required a slight elevation in temperature to 37°C. This is attributed to faster reaction rates at elevated temperatures and the possibility of weak secondary structure or binding interactions of the actuation strands that must be melted to allow for efficient toehold binding and strand displacement. Figure 4.6(b) (bottom) and (c) (bottom) depict the angular distribution, the energy landscape, and a representative TEM image after running the reverse actuation at 37°C for 1 h. DNA strand displacement can be effected by temperature and cation conditions. Figure 4.7 shows the influence of temperature to the reverse actuation of this DNA origami bistable mechanism.

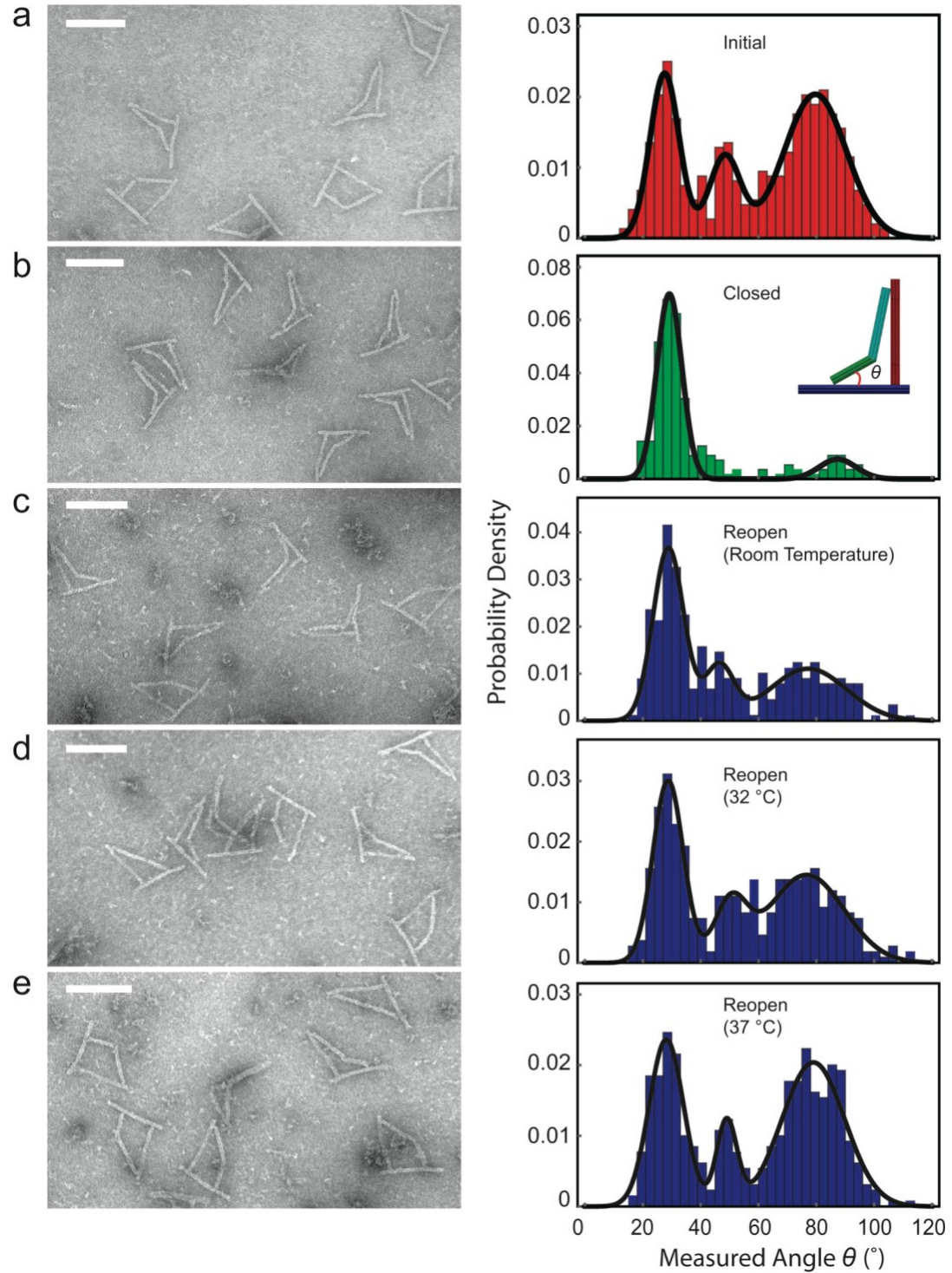


Figure 4.7: Effects of temperature on the reverse actuation. (a) Initial TEM image and angle distribution. (b) Closed configuration actuation. (c) Re-opened experiment at room temperature. (d) Re-opened experiment at 32°C. (e) Re-opened experiment at 37°C.

Figure 4.7(a) presents the initial TEM image and conformation distribution after gel purification. For the closing actuation, closing staples were added at 10-fold excess relative to the structure concentration as measured by a ThermoScientific NanoDrop. The binding reaction was kept at room temperature overnight. Typical TEM image and configuration distribution shown in Figure 4.7(b) demonstrated most of the particles can be switched to the closed state. Then re-open experiment was firstly conducted at room temperature and releasing staples were added at 10-fold concentration relative to the closing staples. But the re-open efficiency is not good shown by typical TEM image and configuration distribution in Figure 4.7(c). Then, temperature of the re-open experiment was increased to 32°C and timescale was limited to 1 hour, TEM image and configuration distribution of the re-opened samples in Figure 4.7(d) indicates the re-open efficiency is increased, but still not high enough. Finally, the re-opened sample kept at 37°C for one hour and then cooled to room temperature and this time the re-open efficiency is pretty good shown in by TEM image and configuration distribution in Figure 4.7(e). All of the percentages of closed, unstable and open configurations and the corresponding equilibrium angles are summarized in Table 4.1.

The distribution and energy landscape of nanomechanisms after the reverse actuation at 37°C is close to the original distribution, suggesting most if not all of the closing strands were removed. These results not only demonstrate control over the stable position of the structure, but also show that the mechanism exhibits passive conformational changes over the energy barrier to reach equilibrium between the two stable configurations. Following the design approach, larger energy barriers could be designed

such that the particles do not switch between the two stable states freely under thermal fluctuation.

Table 4.1: Summary of experimental angle distributions and model.

	Stable position (S1)		Unstable position (U)		Stable position (S2)	
	$\theta \in (0^\circ, 40^\circ)$	Equilibrium angle θ	$\theta \in (40^\circ, 60^\circ)$	Equilibrium angle θ	$\theta \in (60^\circ, 120^\circ)$	Equilibrium angle θ
Design	N/A	29.1°	N/A	N/A	N/A	90.0°
Initial	~31%	27.5°	~16%	48.4°	~53%	79.7°
Closed	~76%	29.2°	~9%	N/A	~15%	N/A
Room temperature	~50%	28.8°	~16%	46.4°	~34%	77.2°
32°C	~39%	28.7°	~19%	50.4°	~42%	76.6°
37°C	~34%	28.1°	~14%	49.0°	~52%	79.0°
Theoretical Model	N/A	29.1°	N/A	49.2°	N/A	90.0°

4.4. Modeling analysis

As introduced in Chapter 2, Pseudo-rigid-body model (PRBM) provides a demonstration of predicting functional mechanical behavior of compliant DNA origami mechanisms. Here, PRBM is applied to analyze the behavior of the bistable mechanism. Both of PRB-1R model and PRB-3R model were employed to study the deformation behavior of the compliant link.

4.4.1. Stiffness measurement of the fixed joint

As mentioned previously, the right angle connection between the compliant link and the frame link was designed to be a rigid connection. Stiffness of the right angle

connection can't be ignored due to the strand connections between these two links are based on the base pairing which can be destabilized by temperature, cation concentration and PH values. To specifically quantify the stiffness of that fixed joint, the structure was folded as an open loop and measured small fluctuations of the joint about the perpendicular position from TEM images (Figure 4.8).

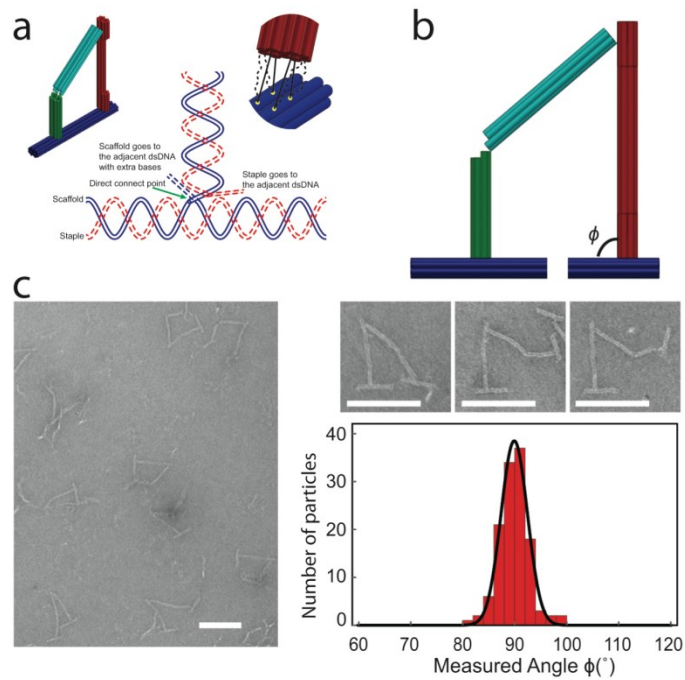


Figure 4.8: Measuring the stiffness of the fixed joint between the compliant and frame links. (a) Sketch of the fixed joint. (b) The 3D sketch of the model used to measure the fixed joint stiffness, scale bars are 100 nm.

Details of the right angle connection are shown in Figure 4.8(a). In Yellow points on the frame link represent the four connection points where ssDNA scaffold connects the frame link (blue) to the compliant link (red). The straight black lines represent

connections where there are no extra bases and the dashed black spline lines represent connections where there are extra bases between them. Connection points are also shown schematically in a double-helix structure. Figure 4.8(b) shows the 3D sketch of the model used to measure the fixed joint stiffness and a small segment in the middle of the frame link was removed so that the whole structure becomes an open loop. TEM images and angle distribution of the fixed joint are shown in Figure 4.8(c). The mean angle is 89.9° and the stiffness is about $1578.9 \text{ pN}\cdot\text{nm}$, calculated by the following equation

$$\kappa \langle \Delta\phi^2 \rangle = k_B T \quad (4.2)$$

where $\Delta\phi$ is the angular displacement of the joint, k_B is Boltzmann's constant and T is absolute temperature.

4.4.2. PRB model

The analysis of rigid body mechanisms has been well studied. However, the analysis of compliant mechanisms (with compliant links), is not a trivial task due to coupling of kinematics and mechanics of solids. Although the finite element method could be used to solve this problem, the fact that it is computationally costly and requires material properties to be known beforehand makes it inconvenient for our study. Here, the so called Pseudo-rigid-body (PRB) model³⁻⁵ is adopted for the design and analysis of compliant mechanisms. Taking a flexible cantilevered beam as an example, the end deformation and energy storing process can be represented by two rigid links connected with a revolute joint which has a torsion spring on it (Figure 4.9 (a, b)).

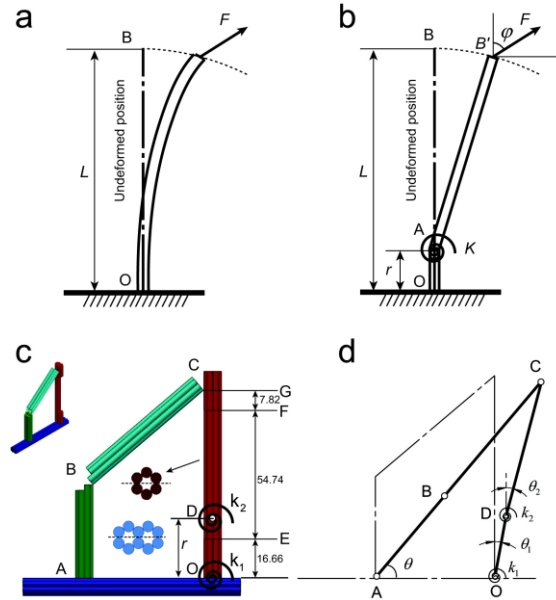


Figure 4.9: The PRB model for the bistable mechanism. (a) Deformed shape of a cantilevered beam. (b) The PRBM for a cantilever beam (c) PRB-1R model of bistable compliant nano-mechanism, dimension unit: nm. (d) Simplified model.

The energy barrier is determined by the maximum deformation of the compliant link. In order to elucidate the energy landscape, a simplified model is developed based on the design of a compliant mechanism. The foundation of this mechanism model is to treat the relatively stiff links as rigid components and replace the compliant link with two rigid links connected by a torsional spring. Several models have been introduced for analyzing the mechanical properties of DNA nanostructures[21,39,101]. Previous studies have also demonstrated that a coupled cylinder model provides a good estimate of the mechanical behavior of designed DNA nanostructures[39,101]. In this model, each dsDNA helix is treated as a cylinder with an effective diameter close to 2.5 nm (DNA origami cross sections tend to swell, so helices exhibit a larger effective diameter)[55]. The compliant

link can then be treated as a beam with a cross section of six double helices in a honeycomb arrangement (Figure 4.9 (c,d)). The deformation of the compliant beam is approximated by two rigid links OD and DC with two torsion springs at the connection points O and D, whose stiffness are k_1 and k_2 , respectively. The position and the stiffness of the torsion spring is given by the following equations

$$r = (1 - \gamma)L_{EG} + L_{OE} \quad (4.3)$$

$$k_2 = \gamma K_{\Theta} \frac{(EI)_{6-hb}}{L_{EG}} \quad (4.4)$$

Here r represents the distance between the revolute joint and the fixed end, L is the beam length, and γ is called the “characteristic radius factor”[32], which is determined by the force angle φ (Figure 4.9(b)).

In this study, OE and FG 10-hb cross section segments are relatively rigid and their deformations are very small. Since FG segment is very short, FG segment is treated as 6 hb cross section for the sake of simplicity. The average value of γ between the two stable configurations is about 0.8654. K is the torsion stiffness and K_{Θ} is called the stiffness coefficient⁵ related to the loading case and geometry, which is also determined by the angle φ (Figure 4.9(b)). The average value of K_{Θ} between the two stable configurations is about 2.6698. E is the Young’s modulus of the material and I is the moment of inertia of the beam cross section. For the compliant link, I can be calculated by

$$I_{6-hb} = 2\left(\frac{\pi D^4}{64} + \frac{\pi D^2}{4}(D)^2\right) + 4\left(\frac{\pi D^4}{64} + \frac{\pi D^2}{4}(D/2)^2\right) \quad (4.5)$$

For the 10-hb cross-section segment, I is calculated by

$$I_{10-hb} = 4\left(\frac{\pi D^4}{64} + \frac{\pi D^2}{4}(D)^2\right) + 6\left(\frac{\pi D^4}{64} + \frac{\pi D^2}{4}(D/2)^2\right) \quad (4.6)$$

Here, $D = 2.5$ nm is the diameter of dsDNA.

The PRB model of the nano-mechanism, the final model is shown in Figure 4.9(c, d). The stiffness of the fixed joint, k_1 , was calculated in Eq. (4.2). And the bending stiffness (EI) of the flexible beam segment was calculated using the equation:

$$L_p = \frac{EI}{k_B T} \quad (4.7)$$

Here, L_p is the persistence length of the bundles of dsDNA. The persistence length of single dsDNA is about 50 nm[102,103]. Here the diameter of single dsDNA is 2.5 nm. This gives a bending stiffness of 11070 pN·nm² or a persistence length of 2700 nm for the 6-hb flexible bundle. Based on Eq.(4.4) and Eq.(4.5) and the average value of γ and K_θ , we can obtain the stiffness $k_2 \approx 408.857$ pN·nm.

The strain energy stored in the two torsion springs can be calculated by

$$SE = \frac{1}{2}k_1(\theta_1)^2 + \frac{1}{2}k_2(\theta_2 - \theta_1)^2 \quad (4.8)$$

In order to solve θ_1 and θ_2 , a kinematic constraint equation of the mechanism is needed.

From the model in Figure 4.9, the edge vectors of the four links (\overline{AD} , \overline{BC} , \overline{AC} , \overline{CD} , \overline{DB}) form a loop which has the follow relationships:

$$\overline{BC} - \overline{AC} + \overline{CD} + \overline{DB} - \overline{AD} = 0 \quad (4.9)$$

$$l_{BC}^2 = \overline{BC} \cdot \overline{BC} \quad (4.10)$$

Here l_{BC} is the length of coupler link. Then, θ_1 and θ_2 can be determined by finding the minimum value of strain energy SE . At the same time the value of strain energy SE at each position will form the energy landscape (Figure 4.10).

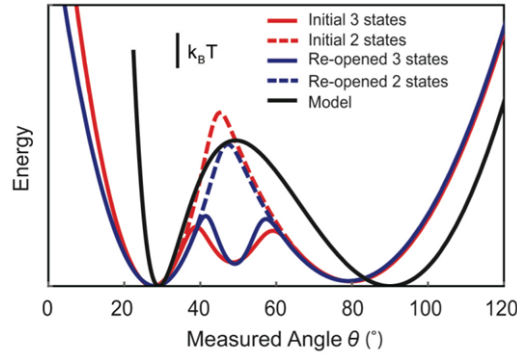


Figure 4.10: Comparison of the energy landscapes obtained from experiment and theoretical model.

In Figure 4.10, red and blue lines show the energy landscape of the nanomechanism in the initial state and the released state after actuation, respectively. The dashed lines show the mechanical energy landscape (i.e. middle energy well removed), which agrees well with the theoretical model (black line). Note that colors are consistent with Figure 4.6, and the red and blue solid lines are identical to those shown in Figure 4.6(b).

In the model, the mechanical energy is completely stored in the two torsional springs. The total energy stored can be calculated using Eq.(4.8). Then the energy landscape of the model is obtained by minimizing the total energy at each position of θ based on the geometric constraint Eq.(4.10). The energy barrier obtained from the model is about 4.12

$k_B T$ occurring at $\theta \approx 49.3^\circ$, whereas the energy barrier showed by the initial and reopened nanomechanisms was approximately $2 k_B T$. However, as previously mentioned, an additional interaction, likely DNA base-stacking between the crank link and the coupler link, creates a decreased local energy at the mechanically unstable position. To determine the energy landscape due purely to mechanical deformation of the compliant link, the energy landscape was calculated from just the normal distribution fits for the two stable positions. In Figure 4.10, the solid red and blue lines show the full energy landscapes for the free and re-opened nanomechanisms, and the red and blue dashed lines show the modified energy landscape purely due to mechanical deformation. The mechanical energy barriers from the free nanomechanism ($4.94 k_B T$) and the reopened nanomechanism ($4.04 k_B T$) resemble the theoretical model ($4.12 k_B T$).

Our pseudo-rigid-body model provides a simple and convenient tool with acceptable accuracy to predict the deformation and mechanical energy storage of compliant nanomechanisms, and demonstrates a feasible approach to model other DNA nanostructures. In addition, the calculated energy landscape is not sensitive to the value of the coefficients (γ and K_\ominus) in the feasible range (sensitivity analysis shown in Figure 4.11). Figure 4.11 shows variation of PRB parameters γ and K_\ominus and sensitivity of the potential energy landscape of the theoretical model. The variation of γ vs. the angle φ is shown in Figure 4.11(a) and the red dashed line represents the average value of γ between the two stable positions. The variation of K_\ominus with the angle φ is shown in Figure 4.11(b) and the green dashed line represents the average value of K_\ominus between the two stable

positions. Energy landscapes calculated using the maximum, average and minimum values of γ between the two stable positions demonstrated negligible sensitivity in the feasible range (Figure 4.11(c)). On the other side, energy landscapes calculated with the maximum, average and minimum values of K_θ between the two stable positions also demonstrated negligible sensitivity in the feasible range (Figure 4.11(d)).

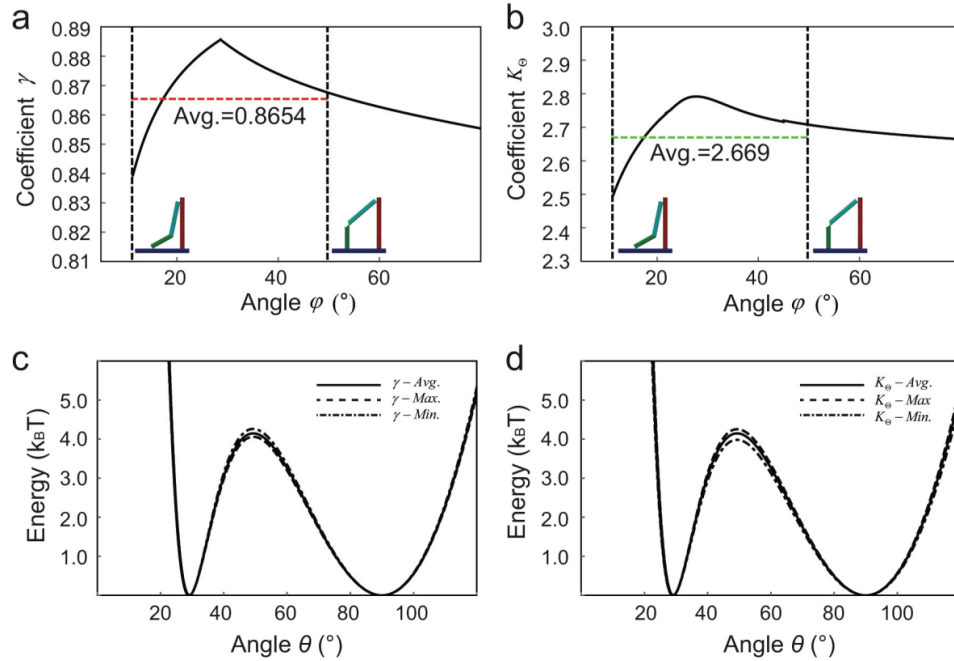


Figure 4.11: Variation of PRB parameters and sensitivity of the potential energy landscape of the theoretical model.

This model also predicts the deformed shape of the nanomechanism very well (Figure 4.12).

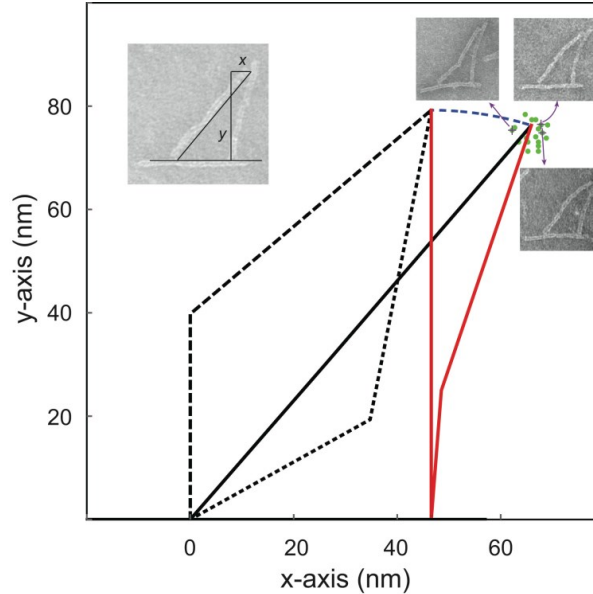


Figure 4.12: Comparison between theoretical PRB model and experimental results for the geometry of the unstable position.

In Figure 4.12, the red line represents the compliant link, the dashed lines are the two stable positions, and the black solid line corresponds to the unstable equilibrium position calculated from the theoretical model. The blue dashed line represents the trajectory of the joint between the coupler link and the compliant link during deformation. The solid red line shows the configuration of maximum deformation for the pseudo-rigid-body model. The green dots represent the compliant link deformation measured from the unstable samples captured from TEM images. The green points are close to the predicted deformed position based on the model. A measured example is shown on the upper left corner.

4.4.3. Modified PRB model

In the previous simplified model, the two 10-hb sections at the ends of the compliant link were ignored. The effect of the 10-hb cross sections at the top and bottom of compliant link needs to be considered. For the sake of simplicity, the top 10-hb cross section is treated as a 6-hb since it is very short, hence has little deformation. The bottom 10-hb cross section is treated as a rigid link since the stiffness is much larger than the 6-hb cross section. If the compliant properties of the 10-hb cross sections are considered in the models, the flexure ability of the entire beam will increase, which means it will be easier to deform the beam and the energy barrier will decrease a little bit.

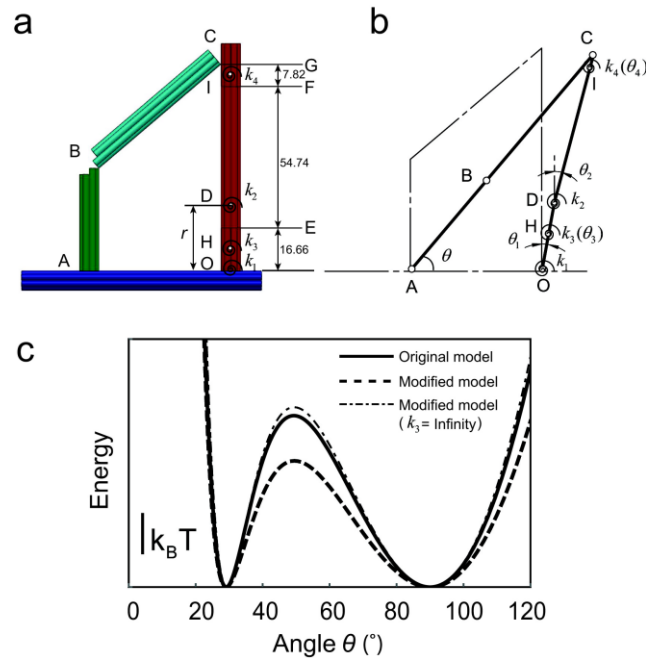


Figure 4.13: Modified model of the bistable nano-mechanism. (a) Dimension details of the modified model. Unit is nm. (b) Simplified modified model. (c) Comparison of energy landscapes.

In order to quantify this, the two 10-hb cross sections are modeled by using two torsion springs placed at the middle of the two segments (positions H and I, Figure 4.13(a,b)). Each of the two 10-hb cross section segments is modeled as two rigid bars connected by a torsion spring. This is based on the fact that the deformations of the two 10-hb cross sections are very small. The torsion spring stiffness is calculated by $(EI)/L$, where EI is the bending stiffness and L is the length of the segment. The entire modified model is shown in Figure 4.13. The stiffness of the 6-hb cross section is calculated by Eq.(4.6), but only considering the length between point E and F. Finally, the stiffness of the four torsion springs are $k_1 = 1578.877 \text{ pN} \cdot \text{nm}/\text{rad}$, $k_2 = 467.10 \text{ pN} \cdot \text{nm}/\text{rad}$, $k_3 = 1205.88 \text{ pN} \cdot \text{nm}/\text{rad}$, $k_4 = 2569.05 \text{ pN} \cdot \text{nm}/\text{rad}$.

The total energy of the modified model is calculated by following equations based on the geometry constrain equations

$$SE = \frac{1}{2}k_1(\theta_1)^2 + \frac{1}{2}k_3(\theta_3 - \theta_1)^2 + \frac{1}{2}k_2(\theta_2 - \theta_3)^2 + \frac{1}{2}k_4(\theta_4 - \theta_2)^2 \quad (4.11)$$

The geometry constrain equations

$$\overline{DC} = \overline{AC} + \overline{CH} + \overline{HD} + \overline{DI} + \overline{IC} - \overline{AD} \quad (4.12)$$

$$l_{BC}^2 = \overline{DC} \cdot \quad (4.13)$$

The result shows that the energy barrier between the original and modified models is about $1.07 k_B T$. In addition, the bottom 10 hb cross section were treated as a rigid link ($k_3=\text{Infinity}$) and find that the obtained energy landscape (dashed line in Figure 4.13) is very close to the initial model. This means the difference between the original and modified model is mainly decided by the bottom 10 hb. The energy barrier (the dashed

line) is slightly off the initial model, which is due to the fact that the model neglected the small geometric difference of the top end (10 hb) and treated the entire flexible link as a 6 hb cross section in the initial model. This also proves that the initial simplified model is acceptable for the nano-mechanism analysis.

4.4.4. Tune the stiffness of the compliant DNA origami bistable mechanism

In previous section, the shape of the energy landscape of the modified model is similar to the initial model, but the energy barrier predicted by the modified model is $\sim 1.1 k_B T$ lower than the initial model. The difference in the height of the energy barrier is mainly caused by some small deformation of the bottom 10-hb cross section segment, where in the initial model, the bottom 10-hb cross section segment were treated as rigid. With this in mind, the accuracy of the simplified model could be improved by making the bottom 10-hb segment of the compliant link more rigid, for example by adding more helices to the cross section. This might also increase the stiffness of the joint between the compliant link and frame link because larger cross section could provide additional positions for joint connections (Figure 4.14(a)). This analysis demonstrates the utility of the theoretical pseudo-rigid-body modeling approach in designing the nanomechanism.

The change of k_1 and k_2 can be realized by varying the geometry design of the compliant link. k_1 is mainly decided by the connections placed between the compliant and bottom links. For example, in order to increase k_1 , more double strands can be put at the bottom end of the compliant link and more connection positions will be provided (Figure 4.14). k_2 is mostly depended on the bending stiffness of the compliant link, the cross section of the compliant link can be changed to vary k_2 . For example, in order to

decrease k_2 , the compliant link can be a 6-hb thin plate (Figure 4.14 (b)). The inertial moment value will be smaller than the honeycomb style 6-hb. The bending stiffness is only $2460 \text{ pN} \cdot \text{nm}^2$ which is about 0.222 of the honeycomb style 6-hb ($11070 \text{ pN} \cdot \text{nm}^2$). In this way, based on Eq.(4.4), the new k_2 will be only 0.222 of the initial design.

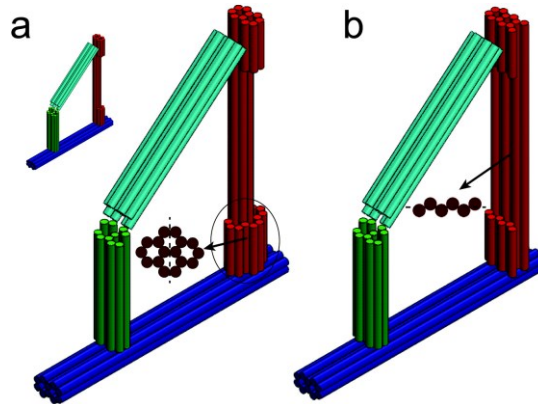


Figure 4.14: Tune the stiffness of the bistable mechanisms. (a) Add more connections at the right angle junction. (b) Modify the shape of the compliant link.

4.4.5. Conformation distribution analysis during depositing and drying process

Generally, it is reasonable to assume that the conformations observed in TEM images are reflective of the conformations in solution. The first reason is that the nano-mechanism is a planar structure. The 2D image is enough to capture the full 3D conformation. Further assumption can be made that once the structure adsorbs on the surface the conformation remains fixed in the conformation the structure attained in solution just when contacting the surface due to the force between the particle and

hydrophilic grid when the particle is adsorbed. Secondly, the design is not a passive structure. The conformational change of the DNA origami nano-mechanism requires a force input to overcome the energy barrier between the open and closed conformations. Therefore, it is not easy for the nano-mechanism to change its conformation during the depositing and drying process. An experimental analysis was performed, detailed here, to test the effects of deposition and drying on the conformational distribution.

During the TEM sample prep, structures may be subjected to a number of forces. First, an important phenomenon during the drying process is called the coffee-ring effect, which may transport many particles to the edge of the grid through a fluid cycle directed from the grid center to the edge[104,105]. A large enough capillary force produced during this process could potentially impact the conformation of the nano-mechanism. In addition to this coffee ring effect, the inter-particle forces may change as particles get concentrated during the drying process and the chance of interactions between particles increases. Finally, particles may experience some additional fluid forces when excess fluid is wicked off the grid prior to applying the negative stain on the grid.

To explore the effect of these or other forces on the conformation of the bi-stable DNA origami nanostructure, variations were tested on the TEM sample prep. The normal sample prep calls for depositing 3.4 μ l of structure solution on the grid and incubating for ~4 min to allow structures to adsorb to the grid surface prior to wicking the remaining fluid off the grid and staining. Two extremes were tested on this prep. First, the sample was allowed to completely dry on the grid surface, which took approximately 17 min. It is assumed that in this “long incubation” case, structures adsorb to the surface prior to

any fluid forces imposed by the wicking process and in the presence of capillary forces that cause the coffee-ring effect (i.e. radially outward flow to replenish liquid evaporated at edges). Secondly, another sample was prepared by depositing the structure solution on a grid and incubating for only ~30 seconds prior to wicking off the remaining fluid and staining. This time, it is assembled that in this “short incubation” case, minimal fluid has evaporated and many of the structures adsorb to the surface in the presence of the fluid forces resulting from the wicking process.

Figure 4.15 shows sample TEM images and angular distributions of both cases as well as the normal sample prep. Specially, Figure 4.15 shows: (a) (Left) TEM images obtained from the center of a grid that had the sample totally dry under room temperature and (Right) the conformation distribution (n=265); (b) (Left) TEM images obtained from the center of a grid made with usual protocol and (Right) the conformation distribution (n=361); (c) (Left) TEM images obtained from the edge of a grid made with usual protocol and (Right) the conformation distribution (n=324); (d) (Left) TEM images obtained from a grid that had the sample deposited for 30 seconds and (Right) the conformation distribution (n=450). Tree energy landscapes of different depositing and drying conditions were compared in Figure 4.15(e). These were derived respectively from initial obtained conformation distribution (red), conformation distribution obtained from the center of a grid that had the sample totally dry under room temperature (orange), conformation distribution obtained from the center of normal grid (purple), conformation distribution obtained from the edge of normal grid (brown) and conformation distribution obtained from the 30 seconds depositing grid (cyan).

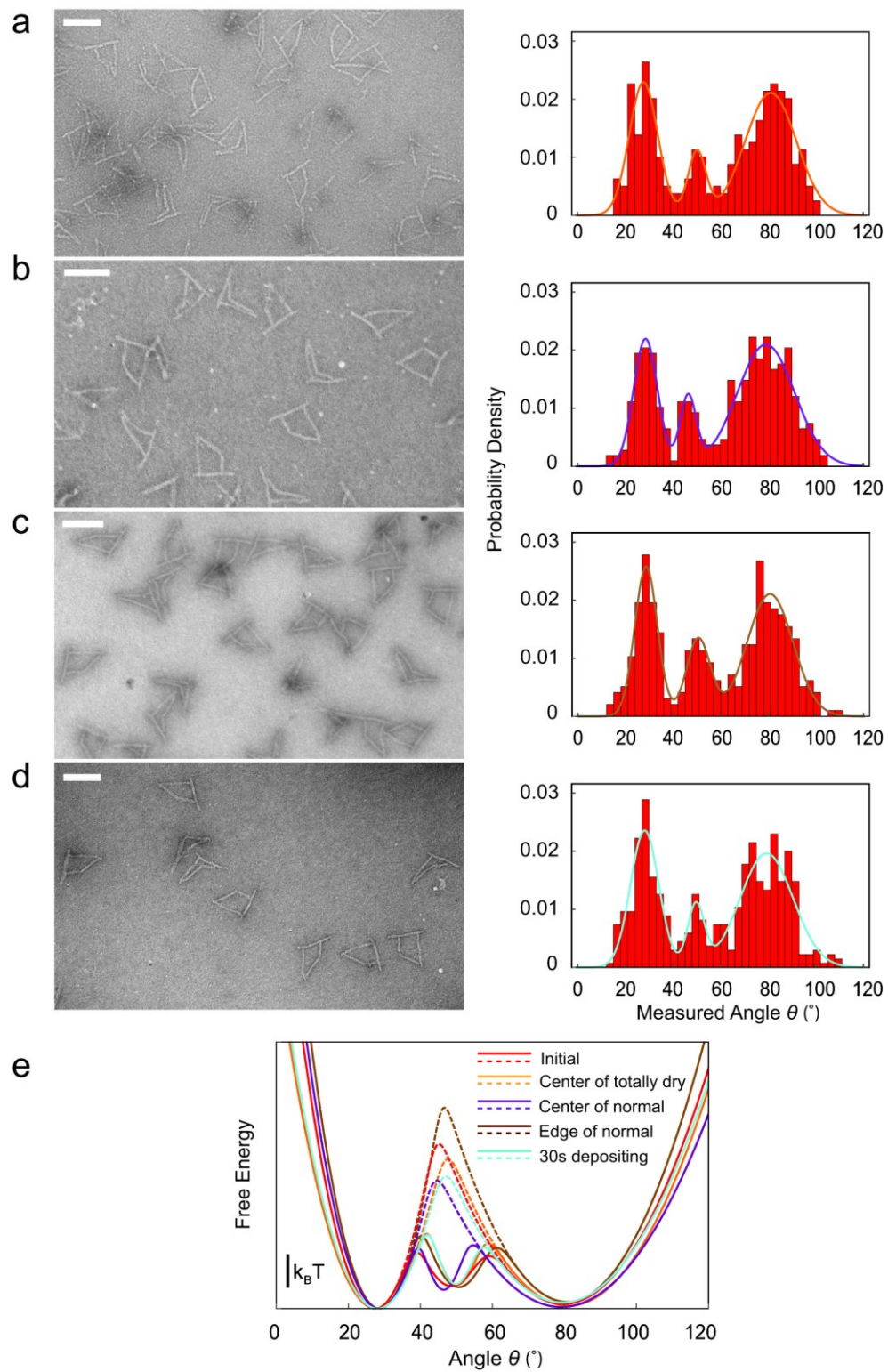


Figure 4.15: Conformational distribution analysis during depositing and drying process.

In the case where the grid was left to dry for 17 minutes, a high density of particles was indeed observed at the edge of the grid confirming the presence of the coffee-ring effect in the sample prep. These images also reveal the presence of structures in both the S1 and S2 configurations both at the center and at the edge. While the angular distribution of structures at the edge is difficult to obtain since many structures overlap, the angular distribution for structures at the center of this “long incubation” case is similar to the normal prep suggesting the fluid forces due to the wicking of excess fluid do not affect the structure conformation. Similarly, structures in both S1 and S2 stable configurations were observed in the “short incubation” case, and the angular distribution again is very similar to the case of the normal prep. Furtherly, re-examined samples was prepared with the normal ~4 min incubation procedure and was compared an angular distribution taken from particles near the center of the grid versus an angular distribution taken from particles near the edge of the grid where capillary forces would be different. Again, differences between these angular distributions were minor.

From what have been discussed above, the original conformation distributions can reflect the real situations in solution. At the same time, depositing and drying processes are really needed to be considered carefully during the analysis especially when the particle is a dynamic structure. Further research is still needed for this topic, since lots of factors can affect the conformation of dynamic nanostructures such as the concentration of particles, concentration of ions, evaporating rate and so on.

4.5. Materials and methods

The DNA origami bistable nanomechanism is self-assembled with the 8064-nt single-stranded scaffold and 189 single-stranded staples (not including actuation staples, Supporting Information Table S2). The scaffold is obtained from the clone of the M13MP18 bacteriophage virus[20] following protocols detailed in Castro et al.[22] The mechanism was designed in caDNAno[55] and the staples were ordered from a commercial vendor (Eurofins, Huntsville, AL). Scaffold was mixed at 20 nM with staples at 10-fold excess (each staple at 200 nM) in a solution containing 5 mM Tris, 5 mM NaCl, 1 mM EDTA, and 14 mM MgCl₂. The self-assembly reactions were conducted in a thermal cycler (Bio-Rad, Hercules, CA) by rapidly heating the solution to 65 °C followed by slow cooling to 4 °C over ~4.5 days.

4.5.1. Structure purification and imaging

DNA origami structures were purified with 2% agarose gels in 0.5× TBE buffer (44.5 mM Tris-borate, 1 mM EDTA) with 11 mM MgCl₂ and 1 μM ethidium bromide. Well-folded samples were separated from agarose using DNA gel extraction spin columns (Bio-Rad, Hercules, CA). Purified structures were imaged on a transmission electron microscope (TEM) for structural feedback as described in Castro et al.[22] Briefly, Formvar coated copper grids stabilized with evaporated carbon film (Electron Microscopy Sciences, Hatfield, PA) were used for TEM imaging. These were prepared by initially depositing 3.4 μl of gel-purified structure solution on a plasma treated grid and incubated for 4 minutes. The structure solution was then wicked away, and a 20 μl drop of 2% Uranyl Formate (SPI, West Chester, PA) was applied to negatively stain the

structures. Next the grid and stain were incubated for 40 seconds and the stain solution was wicked off. Images were taken on a FEI Tecnai G2 Spirit TEM at an acceleration voltage of 80 kV.

4.5.2. DNA displacement actuation

Actuation was achieved using 13 binding staples and 13 releasing staples with lengths ranging from 21 to 51 nt. The concentration of folded particles was measured by UV absorbance on a Nanodrop 2000c (Thermo Scientific NanoDrop Products, Wilmington, DE) after gel purification. The concentration was measured at approximately 1.2 nM. Actuation staples were added so that each staple was at 10-fold excess relative to the structure. For the closing actuation, the sample was kept at room temperature overnight. For the reverse actuation process, the releasing staples were added at 10-fold excess relative to the closing staples, and the sample was kept under 37 °C for about one hour after addition of the releasing staples and then directly prepared for TEM imaging as previously described.

4.6. Summary and discussion

The DNA origami bistable nanomechanism developed here provides a novel technique to design and fabricate a dynamic nanostructure exhibiting multiple stable states separated by designed energy barriers. To our knowledge, this is the first demonstration of direct design of several features (stable states, energy barriers, and distances in between) of a DNA origami nanostructure energy landscape. In comparison to nanomachines built from DNA strands[14,15,61], here the DNA origami approach is

specifically exploited to design components with varying stiffness and anisotropic mechanical properties (i.e. 10-hb has larger bending stiffness preventing out of plane deformations). Furthermore the use of bundles as components enhances our ability to constrain motion because hinges can be defined by multiple connections distributed along a line. The results presented here also establish a foundation for the use of 6-hb and other small DNA origami cross sections to be implemented as compliant or deformable components in DNA-based design with explicit treatment of their strain energy. In the current design, the structure can traverse the energy barrier via thermal fluctuations. However, based on the model, the geometry of the structure or the stiffness of the compliant link could be modified to increase or decrease the height of the energy barrier. Furthermore, this work illustrates the potential for exploiting not just mechanical deformation, but also base-stacking interactions to program local stable states in an energy landscape. These types of structures with multiple stable states and designed energy barriers could provide useful tools for the design of biosensors, mechanical manipulators, or switches whose function is based on specific work inputs.

In the same vein, molecular structures with multistate energy landscapes separated by well-defined energy barriers are ubiquitous in natural biomolecular machinery, in particular proteins such as GCN4 leucine[106], GFP[107], or T4 lysozyme[108] where the details of the energy landscape are critical to the dynamic function of the macromolecule. This research provides a potential model system to explore the design of energy landscapes similar to protein systems in a DNA nanostructure; and further, the

compliant mechanism design approach demonstrated here for a biomolecular system could even potentially be applied to designed protein systems.

This work more generally demonstrates the successful application of macroscopic engineering design concepts to DNA origami nanotechnology. These bottom-up fabricated DNA-based nanomechanisms exhibit similar characteristics to MEMS/NEMS[109–111] devices top-down fabricated from metal, silicon, polymer materials and carbon nanotubes and exhibit some unique advantages compared to traditional materials such as potential self-healing, biochemical functionality, and the ability to interface with biomolecular and even cellular systems.

Chapter 5: Projection Kinematic Analysis of DNA Origami Mechanisms Based on a Two-Dimensional TEM Image

DNA Origami Mechanisms (DOM) are nanometer scale mechanisms made of DNA materials. By mimicking concepts of links and joints in macroscopic mechanisms, we demonstrated that these DOM can produce a prescribed motion pattern. While important progress has been made towards design, fabrication and actuation of DOM, quantitative validation of their kinematic motion remains a challenge. Currently the kinematic analysis of these DOM still heavily relies on the analysis of Transmission Electronic Microscopy (TEM) or Atomic Force Microscopy (AFM) images. TEM gives 2D projections, and AFM gives height information on the top surface of the structure. Hence these images do not represent the true kinematic parameters in space. While 3D reconstruction methods exist, they are highly challenging, time consuming, and often average over many structures, which is problematic for mechanisms that can adopt many configurations. Here we propose a method, which we named “projection kinematics,” for the configuration analysis of individual DOM based on 2D projection images. The method enables finding all possible projected configurations of a DOM in space by solving the projection kinematics equations based on the minimum needed information measured from a 2D image. First, the projection kinematic analysis is demonstrated for

the basic kinematic joints – revolute, prismatic, cylindrical and spherical joints – and one degree-of-freedom (DOF) planar four-bar and two DOFs five-bar linkages. Then, a generalized procedure is presented for projection kinematics analysis. Finally, a universal joint and a Bennett linkage fabricated by DNA origami self-assembly are chosen as proof-of-concept examples to verify the feasibility of projection kinematics analysis of DOM. This approach not only provides valuable guidance for the design of nanoscale mechanisms and robots, but also offers a low cost analysis approach for kinematic verification.

5.1. Background

Structural DNA nanotechnology enables the construction of complex geometrical nanostructures through the bottom-up self-assembly of single DNA strands based on the Watson-Crick base pairing principle[15,112]. Recent advanced, including the development of scaffolded DNA origami [19,22,113], have promoted and expanded the design of dynamic DNA nanostructures. Recently we demonstrated the ability to use scaffolded DNA origami to design and fabricate a series of nanoscale classic kinematic joints, such as the revolute, prismatic, universal joints and kinematic mechanisms including a spatial four-bar Bennett linkage, a crank-slider mechanism and a scissor mechanism [20,21,30]. In addition, we also implemented the design methodology of compliant mechanisms, constructing a compliant hinge joint and a four-bar bistable mechanism [31,39,114]. We call these nanostructures DNA Origami Mechanisms (DOM).

Currently, design validation analysis of these DOM relies on measurement of projected geometric parameters, such as link lengths, angles between two links [20,40] measured from Transmission Electron Microscopy (TEM) or Atomic Force Microscopy (AFM) images. However, TEM gives a 2D projection of 3D structures, and AFM images give height information, but only of the upper most surface of a structure. Hence, it is difficult to fully prescribe the configurations of DOM, especially ones with 3D motion. EM-based reconstruction techniques provide a powerful technique to determine the 3D geometry of biomolecules with nanometer or subnanometer resolution by taking a series of images from different view angles [41,115], and this approach has been applied to DNA origami[116]. However, this technique depends heavily on the preparation quality of the sample and often requires averaging over many structures, which is problematic for DOM that adopt many configurations. In addition, the post imaging-processing algorithm for 3D reconstruction from 2D TEM images is far from mature. Recent single particle reconstruction methods have demonstrated tremendous promise for the 3D structure analysis of individual molecules and nanoparticles [116,117]; however, these methods are challenging and require time consuming optimization of sample preparation.

Here we present an alternative approach to validate the kinematic motion of DOM by analyzing its projected kinematic constraint equations to determine the relative spatial geometries of links projected on a 2D plane. Intuitively, the projected configuration of a DOM is determined by its configuration in space as well as the projection direction. If the projection direction is fixed, the motion of the mechanism in the projected image will follow the motion of the DOM in space. For example, Su et al. [115] first derived the

motion of the Bennett linkage in space and then projected the entire Bennett linkage configuration on a designated 2D plane. By kinematic analysis of a one DOF Bennett 4-bar linkage, Su et al. had successfully determined the projected joint angles and compared them with measured data from 2D TEM images.

In this chapter, we further expand this method to the kinematic analysis of projected configurations of general mechanisms. We call this approach “projection kinematics.” It differs from the projective kinematics in that projective kinematics reconstructs a 3D object from at least two stereo images [118] while our projection kinematics predicts 3D configurations using one 2D image.

This chapter is organized as the following. First, a general algorithm of the projection kinematics analysis of mechanisms is devised based on the investigation of various kinematic joints and four-bar and five-bar linkages. Second, a universal joint and Bennett linkage fabricated by DNA origami are used as two case studies to demonstrate the feasibility and describe the application process of projection kinematics. Multiple solutions can be obtained by solving the projection kinematics equations based on the information measured from the projected configuration. Also, different information, such as the combination of different angles or link lengths measured can result in different projection kinematics equations, which can obtain different solutions and some of them are mechanically different. Usually, measuring angles between two links is easier and has better measurement accuracy than measuring lengths because the ends of the links are often blurry in TEM images, especially for biological materials that are generally flexible and do not give strong contrast. At last, we will discuss the minimum variables that must

be measured for solving of projection kinematics equations and how to eliminate the extraneous one to determine the right solutions.

5.2. Projection analysis of kinematic joints

The configuration of a DOM is determined if it is fully controlled, i.e. the number of actuated kinematic parameters equals the number of its degree-of-freedom (DOF). Then the entire mechanism can be treated as a static structure and its configuration in space can be modeled by conducting the transformation in global frame. For convenience, we define the project direction as the z -axis. The projection plane is the x - y plane. Only rotations about x and y axes alter the projected configuration of the DOM. In addition, the rotation about the x -axis does not affect the projected length of a link placed along the x -axis. The same is true for the y -axis.

Mathematically, the rotation matrices about the x -axis (rotation angle α) and y -axis (rotation angle β) are defined as

$$[X(\alpha)] = \begin{bmatrix} 1 & 0 & 0 \\ 0 & \cos \alpha & -\sin \alpha \\ 0 & \sin \alpha & \cos \alpha \end{bmatrix} \text{ and } [Y(\beta)] = \begin{bmatrix} \cos \beta & 0 & \sin \beta \\ 0 & 1 & 0 \\ -\sin \beta & 0 & \cos \beta \end{bmatrix} \quad (5.1)$$

Combining these gives the resultant rotation matrix $[R]$ as

$$[R] = [Y(\beta)][X(\alpha)] = \begin{bmatrix} \cos \beta & \sin \alpha \sin \beta & \cos \alpha \sin \beta \\ 0 & \cos \alpha & -\sin \alpha \\ -\sin \beta & \sin \alpha \cos \beta & \cos \alpha \cos \beta \end{bmatrix} \quad (5.2)$$

For any given joint, or mechanism, the projection kinematics analysis will determine all possible spatial configurations that can have a particular projected configuration. Mechanisms are comprised of links connected by kinematic joints, such as revolute,

prismatic, cylindrical and spherical joints. Because of the practical difficulties in measuring the detailed geometric shape of a link from a 2D image, we simplify a link into a single line, which is sufficient to reconstruct the kinematic configuration of the DOM. Considering the links as rigid lines, their projection is the same as the projection of static structure and their shape can be reconstructed by the views taken from any side. The derivation of projection kinematics for mechanisms is based on the projection analysis of the classic kinematic joints. The top of **Error! Reference source not found.** shows the sketches of revolute, prismatic, cylindrical and spherical joints in space and their projected configurations on the x - y plane are shown at the bottom of **Error! Reference source not found.**. The origin of the global coordinate frame is placed at the point **O** and the x -axis is pointing in the direction of link OA and the z axis is the projection direction.

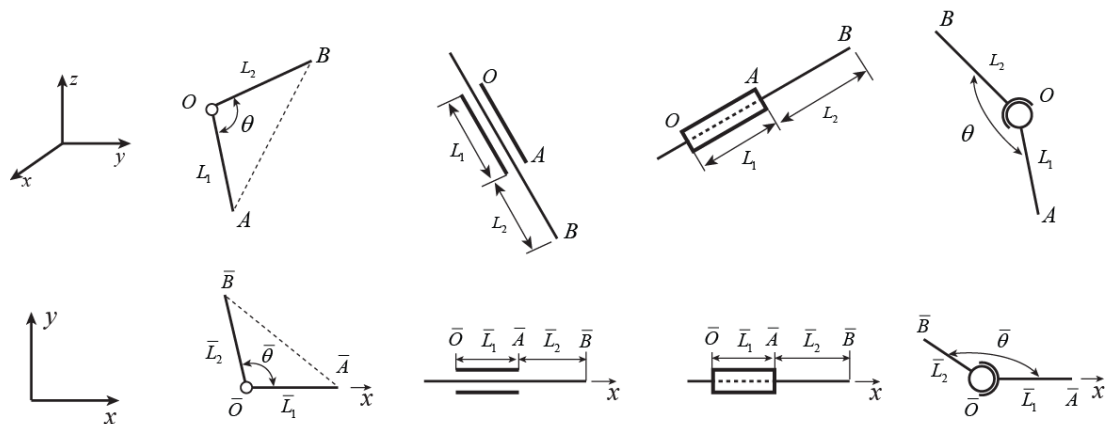


Figure 5.1: Kinematic parameters of revolute, prismatic, cylindrical and spherical joints (from left to right) are 3D (top) in nature.

In the following sections, the projection kinematics of the revolute, prismatic, cylindrical and spherical joints will be discussed in details.

5.2.1. Revolute joint

A revolute joint is constructed by two links connected with a pin joint to yield one rotational DOF. Figure 5.2 shows a sketch of a revolute joint, where cylinders represent the links and balls represent joints and end points of links. Note this representation neglects the shape of links and joints. This representation method is also used in the following sections. In Figure 5.2, the local coordinate frame xyO_0 is defined with x -axis along one link and x - y plane on the plane formed by the two links and in order to clearly show the spatial and projected configurations respectively, the spatial configuration is shifted vertically to a position above the x - y plane. The projected parameters are shown on the projected configuration (Figure 5.2(c)).

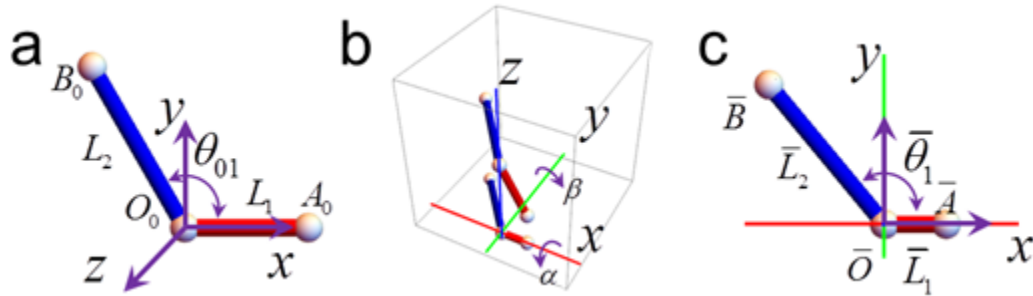


Figure 5.2: Projection of a revolute joint formed by two links.

For the analysis of the revolute joint, we assume that both links are initially laid on the x - y plane with the link $\mathbf{O}_0\mathbf{A}_0$ along the x -axis and \mathbf{O}_0 at the origin position of the global frame, as shown in Figure 5.2(a). Here the two link lengths are L_1 and L_2 , and the joint angle is θ_0 .

For convenience, let us define the x - y plane projection matrix as

$$[P] = \begin{bmatrix} 1 & 0 & 0 \\ 0 & 1 & 0 \\ 0 & 0 & 0 \end{bmatrix} \quad (5.3)$$

By multiplying $[P]$, the projection coordinate $(x, y, 0)$ on the x - y plane of any spatial points (x, y, z) can be obtained. The geometric information for the projected configuration (Figure 5.2(c)), namely the projected link lengths \bar{L}_1 , \bar{L}_2 and the projected angle $\bar{\theta}_1$ can be measured by image analysis tools.

Table 5.1: Initial, rotated, projected and measured points that define the structure of the revolute joint

Points in the local reference frame	Points after rotation	Projected points	Measured points from a 2D image
$\mathbf{A}_0 = (L_1, 0, 0)^T$	$\mathbf{A} = [R]\mathbf{A}_0$	$\bar{\mathbf{A}} = [P]\mathbf{A}$	$\bar{\mathbf{A}} = (\bar{L}_1, 0, 0)^T$
$\mathbf{B}_0 = (L_2 \cos \theta_{01}, L_2 \sin \theta_{01}, 0)^T$	$\mathbf{B} = [R]\mathbf{B}_0$	$\bar{\mathbf{B}} = [P]\mathbf{B}$	$\bar{\mathbf{B}} = (\bar{L}_2 \cos \bar{\theta}_1, \bar{L}_2 \sin \bar{\theta}_1, 0)^T$

Comparing the coordinates of projected points and measured points in Table 5.1, we can obtain the following three equations

$$\begin{cases} L_1 \cos \beta = \bar{L}_1 \\ L_2 (\cos \theta_{01} \cos \beta + \sin \theta_{01} \sin \alpha \sin \beta) = \bar{L}_2 \cos \bar{\theta}_1 \\ L_2 \sin \theta_{01} \cos \alpha = \bar{L}_2 \sin \bar{\theta}_1 \end{cases} \quad (5.4)$$

Parameters α , β and θ_{01} can be solved from Eq.(5.4) when \bar{L}_1 , \bar{L}_2 and $\bar{\theta}_1$ are measured from the projected configuration. It is noted that only the last two equations in (5.4) are mildly coupled. Solving the first equation yields two solutions of β . Substituting either of those solutions for β into the last two equations in (5.4) and eliminating α lead to an equation for θ_{01} , which we can solve to obtain four solutions. Hence, we conclude that there are at most eight solutions for the system given by Eq.(5.4).

A numerical example is shown below to validate the projection kinematics solution process for a revolute joint. First, the length of the links, the joint angle θ_{01} and global rotation angles α, β are chosen randomly (excluding the extreme position, such as the link perpendicular to the x - y plane) shown in the first row of Table 1. Secondly, the designed projected configuration can be obtained and the projection variables are shown in the second row of Table 5.2.

Table 5.2: Numerical example for projection kinematic analysis of revolute joints

Initial configuration	$L_1=100, L_2=150, \theta_{01}=120^\circ$
Rotation angles	$\alpha = -30^\circ, \beta = 60^\circ$
Projected configuration	$\bar{L}_1=50, \bar{L}_2=195.256, \bar{\theta}_1=129.809^\circ$

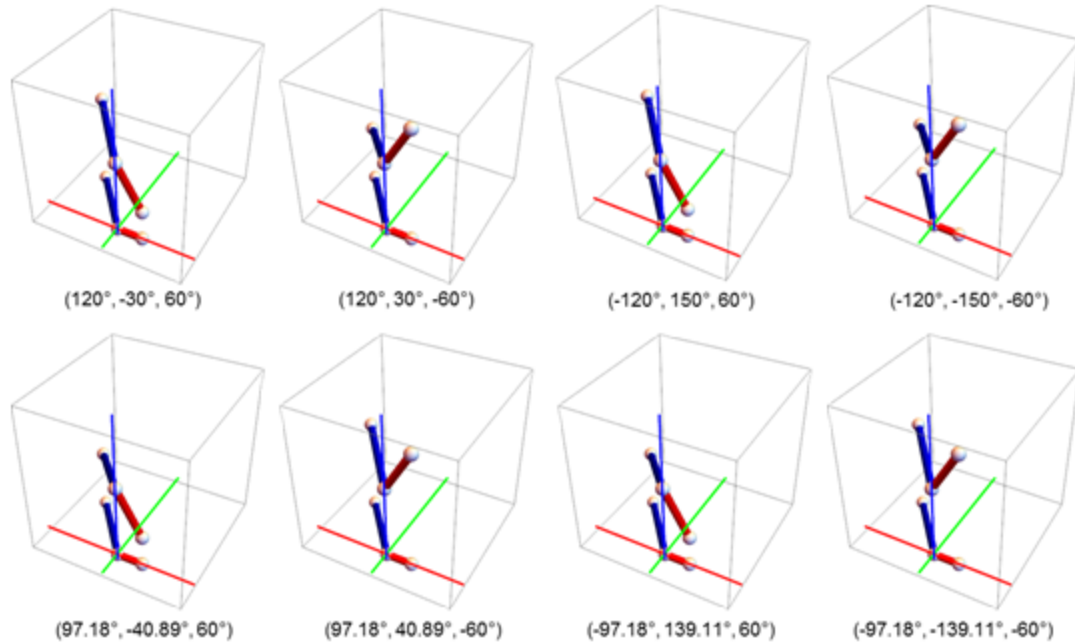


Figure 5.3: Configuration solutions of the projection kinematic analysis of a revolute joint.

Eight solutions are obtained by solving Eq. (5.4) when keep θ_{01} , α and β as unknowns and substituting the other variables shown in Table 1 into the equations. Figure 5.3 shows the eight possible solutions that can correspond to the same projected configuration, where each solution has the spatial configuration above the x - y plane and the projected configuration on the x - y plane (θ_{01} , α and β for each solution are shown under the figure as $(\theta_{01}, \alpha, \beta)$). The first solution is the same as the specified initial configuration shown in Table 5.2. The second solution has the same joint angle as the designed, but the global rotation angles α and β are actually opposite as designed. It means the revolute joint has two spatial positions that can have the same projected configuration. These kinds of

solutions can be grouped as a set. Then, the third and fourth solutions construct another set whose joint angle is -120° which means the joint rotates in the opposite direction. In addition, α of third and fourth solutions have the negative supplementary angle values as the first and second solutions respectively, while β are respectively the same. If the rotation direction can be determined from the projected configuration, for example by some asymmetric feature on a link, then the solutions with opposite rotation angle can be eliminated. The absolute angle value of the bottom four solutions is 97.18° , which means the revolute joint can have two different joint angles that correspond to the same projected configuration. Figure 5.4 shows two examples of the symmetrical (or mirrored) configurations of a revolute joint (Figure 5.4(a)) and planar four-bar linkage (Figure 5.4(b)).

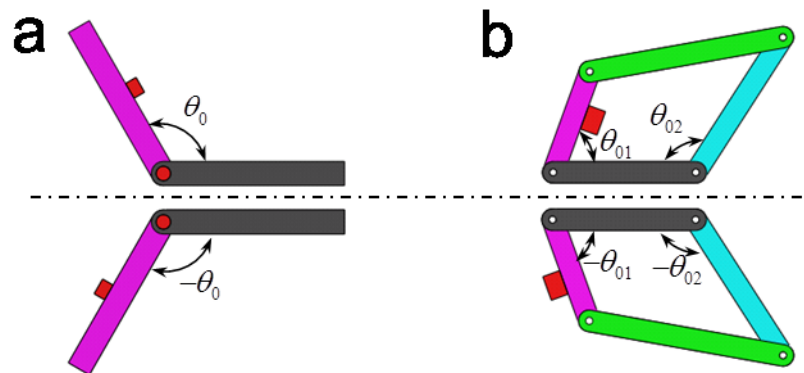


Figure 5.4: Explanation of symmetrical (mirrored) configurations distinguished by a designed feature (red box on the purple link). (a) Positive and negative revolute joint angles. (b) Symmetrical configurations of planer four-bar linkage.

An asymmetric feature, indicated by the small red box placed on the purple links can specify the rotation direction of the revolute joint and also tell the difference of the configuration of the four-bar linkage. This provides an important criterion for the design if 2D images are to be used for the analysis and verification of motion. Alternatively, if the range of angular motion can be constrained by the design, for example to be between 0° and 180° , then the joint angle can be uniquely specified. We previously used this approach for a DNA origami hinge [6].

In the following section, all of the solutions with negative rotation angles or mirrored configurations are still presented in the figures of solutions even though they look the same as the target configuration. In general asymmetric design features box can confirm the difference easily.

5.2.2. Prismatic joint

Prismatic joints are usually constructed by a slider that translates linearly relative another part. A simple example is a square rod that slides with a single DOF inside a square tube. Figure 5.5(a) shows the coordinate frame of a general prismatic joint whose cross section is rectangular and the red and blue components are the fixed part and the slider, respectively. The x -axis points along the translation direction of the blue slider. From the model, the rotation about x -axis does not change the projection result if the geometrical information of the joint is ignored. L_1 and L_2 are the length of the fixed component (red) and the extension of the slider beyond the fixed component, as shown in Figure 5.5(a). The sketch of the projected configuration of this prismatic joint is shown in

Figure 5.5(b). In addition, the projection variables, \bar{L}_1 and \bar{L}_2 corresponding with L_1 and L_2 respectively, are shown in Figure 5.5(c).

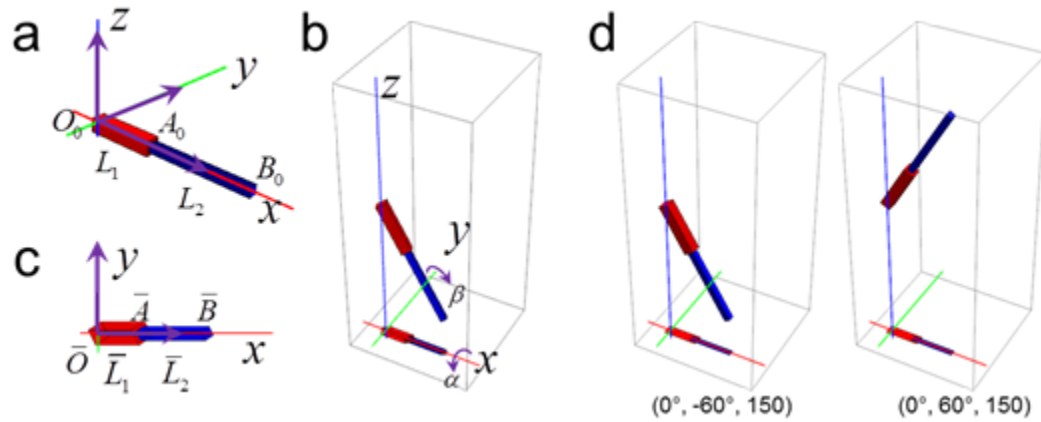


Figure 5.5: Projection kinematic analysis of prismatic joint and a numerical example. (a). The coordinate frame of prismatic joint. (b). Sketch of the projection of prismatic joint. (c). Projected configuration of the prismatic joint. (d). Solutions of a numerical example of projection kinematics analysis of prismatic joint.

By following the same solution procedures applied to the revolute joint, we can obtain the following two projection kinematic equations for a prismatic joint

$$\begin{cases} L_1 \cos \beta = \bar{L}_1 \\ (L_1 + L_2) \cos \beta = \bar{L}_1 + \bar{L}_2 \end{cases} \quad (5.5)$$

The angle α doesn't show up in Eq.(5.5) because the rotation about x -axis does not change the projected lengths, \bar{L}_1 and \bar{L}_2 . Solving Eq. (5.5) yields two solutions with identical L_2 but opposite signs of β in terms of L_1 , \bar{L}_1 and \bar{L}_2 , which means the prismatic joint has a unique configuration with two opposite rotation positions about the y -axis that

correspond to the same projected configuration. A numerical example for the projection kinematic analysis of prismatic joint is shown in Table 5.3.

Table 5.3: Numerical example for projection kinematic analysis of a prismatic joint

Initial configuration	$L_1=100, L_2=150$
Rotation angles	$\alpha = -30^\circ, \beta = 60^\circ$
Projected configuration	$\bar{L}_1=50, \bar{L}_2=75$

5.2.3. Cylindrical joint

The cylindrical joint not only has a translational DOF but also a rotational DOF about the sliding axis. That rotation does not affect the projected configuration if the x -axis of the global coordinate frame is placed along the rotation axis. In other words, it is impossible to obtain the rotation angle of the cylindrical joint from the projected image if the geometrical information of the joint is neglected or undistinguishable. Then the projection kinematics analysis is the same as the prismatic joint if the local rotational DOF is ignored.

5.2.4. Spherical joint

A spherical joint as shown in Figure 5.1 has three DOFs. Instead of using traditional azimuth and zenith angles for the modeling, here we use the angle θ_{01} between links O_0A_0 and O_0B_0 , and the angle ϕ_0 of link O_0B_0 rotating about x -axis to describe the configuration

of spherical joint. In addition, the third DOF, rotation around link O_0B_0 , is neglected as it does not affect the projected configuration. Actually, the full geometry of the spherical joint is determined only by the angle θ_{01} if the shape of the two links is negligible.

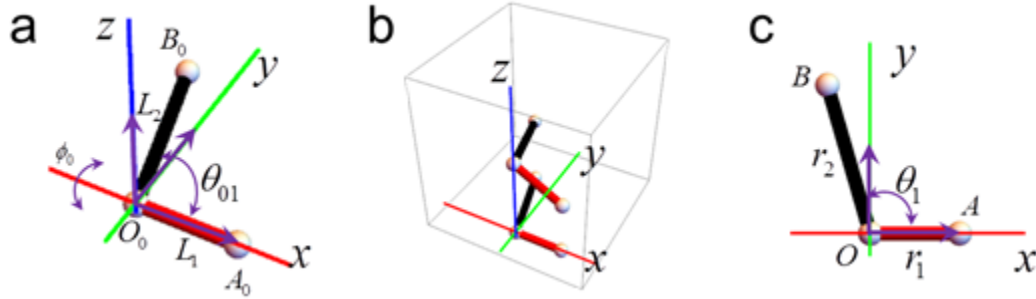


Figure 5.6: Projection kinematics analysis of spherical joint. (a). The local coordinate frame of spherical joint. (b). Sketch of the projection of spherical joint. (c). Projected configuration of the spherical joint.

When the angle θ_{01} and ϕ_0 are given, the general configuration of the entire spherical joint in space (Figure 5.6(a)) can be determined. Setting the coordinates of projected points (3rd column) equal to the measured points (4th column) in Table 5.4, we obtain three projection kinematics equations

$$\begin{cases} L_1 \cos \beta = \bar{L}_1 \\ L_2 (\cos \theta_{01} \cos \beta + \sin \theta_{01} \cos(\alpha + \phi_0) \sin \beta) = \bar{L}_2 \cos \bar{\theta}_1 \\ L_2 \sin \theta_{01} \sin(\alpha + \phi_0) = \bar{L}_2 \sin \bar{\theta}_1 \end{cases} \quad (5.6)$$

However the above three equations are not sufficient to solve the four unknowns, α , β , θ_{01} and ϕ_0 .

Table 5.4: Initial, rotated, projected and measured points that define the structure of the spherical joint

Points in the local reference frame	Points after rotation	Projected points	Measured points from a 2D image
$\mathbf{A}_0 = (L_1, 0, 0)^T$	$\mathbf{A} = [R]\mathbf{A}_0$	$\bar{\mathbf{A}} = [P]\mathbf{A}$	$\bar{\mathbf{A}} = (\bar{L}_1, 0, 0)^T$
$\mathbf{B}_0 = [X(\phi_0)]\mathbf{B}_{00}$	$\mathbf{B} = [R]\mathbf{B}_0$ $= [Y(\beta)][X(\alpha + \phi_0)]\mathbf{B}_{00}$	$\bar{\mathbf{B}} = [P]\mathbf{B}$	$\bar{\mathbf{B}} = (\bar{L}_2 \cos \bar{\theta}_1, \bar{L}_2 \sin \bar{\theta}_1, 0)^T$

Here $\mathbf{B}_{00} = (L_2 \cos \theta_{01}, L_2 \sin \theta_{01}, 0)^T$.

Noticing that $\alpha + \phi_0$ in Eq. (5.6) can be treated as a single unknown, eight solutions of β , θ_{01} and $\alpha + \phi_0$ can be obtained similarly to the projection kinematics analysis of revolute joint. This agrees with our intuition that the initial configuration is determined by the angle θ_{01} and the local rotation ϕ_0 is coupled to the global rotation about x -axis. In other words, the projection kinematics of spherical joint reduces to the same analysis as the revolute joint if the specific geometry of the links is neglected. To validate the projection kinematics analysis procedure of a spherical joint, a numerical example shown in Table 5.5 is used.

Table 5.5: Numerical example for projection kinematics analysis of a spherical joint

Initial configuration	$L_1=100, L_2=150; \theta_{01}=100^\circ, \phi_0= 15^\circ$
Rotation angles	$\alpha = -30^\circ, \beta=30^\circ$
Projected configuration	$\bar{L}_1=86.60, \bar{L}_2=148.65, \bar{\theta}_1=106.28^\circ$

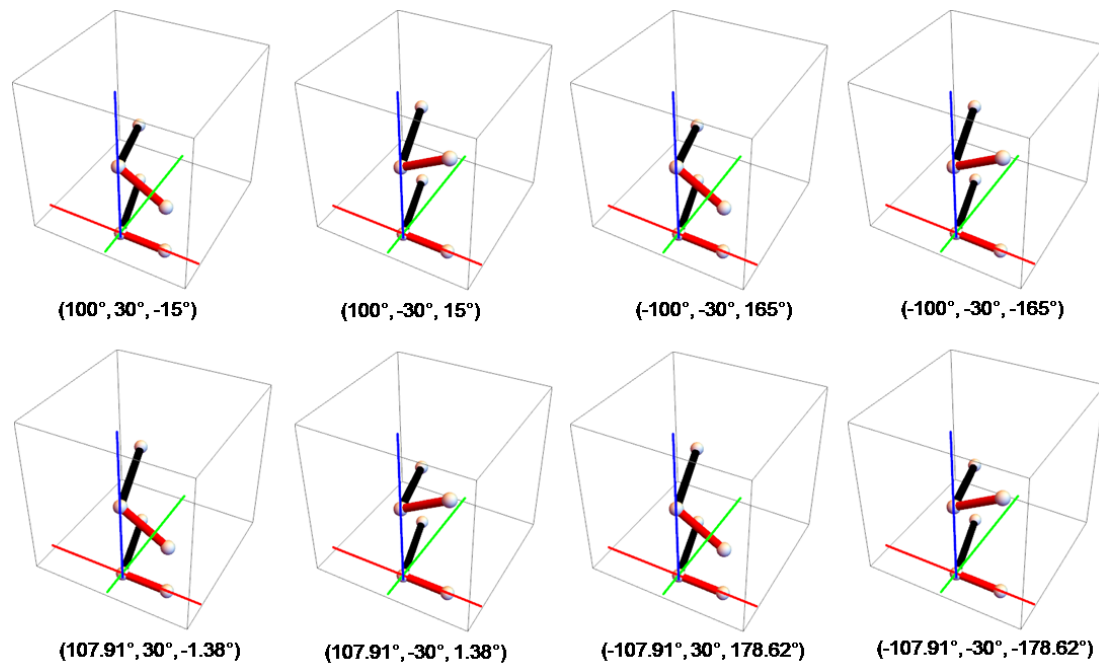


Figure 5.7: Configuration solutions of the projection kinematic analysis of a spherical joint. θ_{01} , β and $\alpha+\phi_0$ for each solution is shown under the figure as $(\theta_{01}, \beta, \alpha+\phi_0)$.

Eight solutions of $(\theta_{01}, \beta, \alpha+\phi_0)$ are obtained and the corresponding projection sketches are shown in Figure 5.7. Similar to the revolute joint, the first two solutions have the same θ_{01} as the specified one in Table 5.5 and the third and fourth solutions have the opposite θ_{01} . The other four solutions have a different θ_{01} and different spatial positions with the seventh and eighth solutions having an opposite θ_{01} as the fifth and sixth solutions.

From the projection kinematic analysis of revolute, prismatic, cylindrical and spherical joints, if the rotation direction is identifiable, for example by an asymmetric design feature, there would be only two configurations with two spatial positions for each joint

that can have the same projected configuration for a revolute or a spherical joint. If the rotation of the prismatic and spherical joint about the sliding axis cannot be identified, there will be only one configuration solution with two spatial positions that can have the same projected configuration.

5.3. Projection kinematics of planar mechanisms

Building on the projection kinematics analysis for basic kinematic joints, we can apply the projection kinematics analysis to any planar or spatial mechanisms. Different from the single joint analysis, we consider closed-chain mechanisms with four or more links, which provides more information for analysis of projected configurations. In addition, the DOF of the mechanism can introduce additional constraints to the analysis. We first consider a general four-bar linkage and a general five-bar linkage as examples to show the comprehensive analysis procedure.

5.3.1. Planar four-bar linkage

Planar four-bar linkages are constructed by four links connected by four revolute joints. Figure 5.8(a) shows the sketch and coordinate frame of a general four bar linkage. As explained previously, thick lines and circles are used to represent the links and joints respectively. We assume the thickness of the lines and the size of the dots are infinitely small. In reality, the geometry of the links or details of the joint may provide constraints to the range of motion of each joint. However, this would only simplify the projection kinematics analysis by allowing selection of the correct solution. The configuration in

space can still be obtained by the consequently rotations about x -axis and y -axis and the rotation matrix is the same as Eq. (5.2).

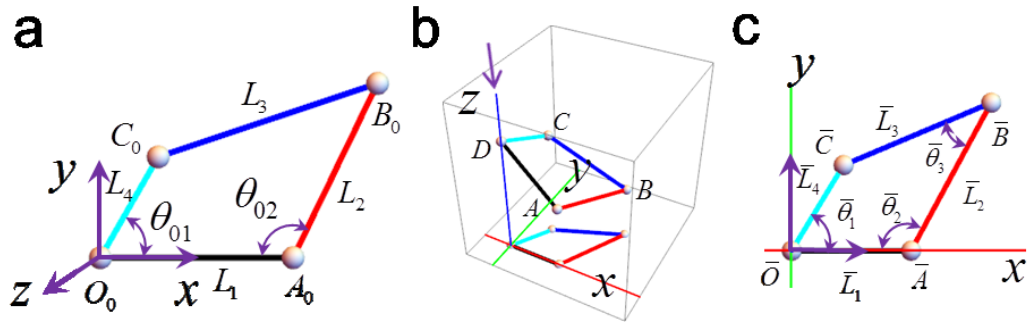


Figure 5.8: Projection kinematic analysis of a planar four-bar linkage. (a). The local coordinate frame of planar four-bar linkage. (b). The original and projected planar four-bar linkage. (c). The projected configuration.

In contrast to single joints, the four-bar linkage has its own kinematics equations which should be solved first to obtain the true configuration if any of the input angles, e.g. θ_{01} , is given. These kinematics equations of the projected configuration can introduce extra constraints.

The spatial configuration can be obtained by two global rotation angles α and β (Figure 5.8(b)). Plus one extra unknown for the input parameter, there are three unknowns in total that need to be solved. Therefore, three constraint equations must be derived based on the information measured from the projected configuration as well as the closed-loop constraint equation. The detailed derivation is described below.

Equating the coordinates of projected points (3rd column) and measured points (4th columns) in Table 5.6 yields five projection kinematic equations,

$$L_1 \cos \beta = \bar{L}_1 \quad (5.7)$$

$$L_1 \cos \beta - L_2 \cos \beta \cos \theta_{02} + L_2 \sin \alpha \sin \beta \sin \theta_{02} = \bar{L}_1 + \bar{L}_2 \cos(\pi - \bar{\theta}_2) \quad (5.8)$$

$$L_2 \cos \alpha \sin \theta_{02} = \bar{L}_2 \sin(\pi - \bar{\theta}_2) \quad (5.9)$$

$$L_4 \cos \beta \cos \theta_{01} + L_4 \sin \alpha \sin \beta \sin \theta_{01} = \bar{L}_4 \cos \bar{\theta}_1 \quad (5.10)$$

$$L_4 \cos \alpha \sin \theta_{01} = \bar{L}_4 \sin \bar{\theta}_1 \quad (5.11)$$

And the geometric constraint equation of the constant coupler link is $|\mathbf{B}_0 - \mathbf{C}_0| - L_3 = 0$, which can be rewritten as the following equation after substituting the coordinates of in \mathbf{B}_0 and \mathbf{C}_0 ,

$$L_1^2 + L_2^2 + L_4^2 - L_3^2 - 2L_1L_4 \cos \theta_{01} - 2L_1L_2 \cos \theta_{02} + 2L_2L_4 \cos(\theta_{01} + \theta_{02}) = 0 \quad (5.12)$$

Including the geometry constraint equation Eq.(5.12), six equations are obtained and θ_{01} , θ_{02} , α , β , $\bar{\theta}_1$, $\bar{\theta}_2$, \bar{L}_1 , \bar{L}_2 and \bar{L}_4 are the unknowns.

Table 5.6: Initial, rotated, projected and measured points that define the structure of planar four-bar linkage

Points in the local reference frame	Points after rotation	Projecte d points	Measured points from a 2D image
$\mathbf{A}_0 = (L_1, 0, 0)^T$	$\mathbf{A} = [R]\mathbf{A}_0$	$\bar{\mathbf{A}} = [P]\mathbf{A}$	$\bar{\mathbf{A}} = (\bar{L}_1, 0, 0)^T$
$\mathbf{B}_0 = \mathbf{A}_0 + L_2(\cos(\pi - \theta_{02}), \sin(\pi - \theta_{02}), 0)^T$	$\mathbf{B} = [R]\mathbf{B}_0$	$\bar{\mathbf{B}} = [P]\mathbf{B}$	$\bar{\mathbf{B}} = \bar{\mathbf{A}} + (\bar{L}_2 \cos(\pi - \bar{\theta}_2), \bar{L}_2 \sin(\pi - \bar{\theta}_2), 0)^T$
$\mathbf{C}_0 = L_4(\cos \theta_{01}, \sin \theta_{01}, 0)^T$	$\mathbf{C} = [R]\mathbf{C}_0$	$\bar{\mathbf{C}} = [P]\mathbf{C}$	$\bar{\mathbf{C}} = (\bar{L}_4 \cos \bar{\theta}_1, \bar{L}_4 \sin \bar{\theta}_1, 0)^T$

Notice that there are eight total parameters including four angles, $\bar{\theta}_1$, $\bar{\theta}_2$, $\bar{\theta}_3$ and $\bar{\theta}_4$, and four link lengths, \bar{L}_1 , \bar{L}_2 , \bar{L}_3 and \bar{L}_4 , which can be measured on the projected configuration (Figure 5.8©). This gives a total of 56 combinations of three parameters that can be chosen from the total of eight. However, we only need to consider the following four cases without loss of generality.

1. Two adjacent links and the joint between them are measured. Without loss of the generality, if \bar{L}_1 , \bar{L}_4 and $\bar{\theta}_1$ are measured, then Eqs. ((5.7), (5.10), (5.11)) and constraint equation Eq. (5.12) are enough to solve θ_{01} , θ_{02} , α , β . The solving process is identical to that of the revolute joint.
2. Two adjacent joint angles and the length of link between them. For instance, if $\bar{\theta}_1$, \bar{L}_1 and $\bar{\theta}_2$ are measured, \bar{L}_2 can be solved first by Eq. (5.9)

$$\bar{L}_2 = L_2 \cos \alpha \sin \theta_{02} / \sin(\pi - \bar{\theta}_2) \quad (5.13)$$

Substituting (5.13) into (5.8) yields

$$L_1 \cos \beta - L_2 \cos \beta \cos \theta_{02} + L_2 \sin \alpha \sin \beta \sin \theta_{02} = \bar{L}_1 + (L_2 \cos \alpha \sin \theta_{02} / \sin(\pi - \bar{\theta}_2)) \cos(\pi - \bar{\theta}_2), \quad (5.14)$$

and \bar{L}_4 can be solved by Eq. (5.11)

$$\bar{L}_4 = L_4 \cos \alpha \sin \theta_{01} / \sin \bar{\theta}_1, \quad (5.15)$$

Substituting (5.15) into (5.10) yields

$$L_4 \cos \beta \cos \theta_{01} + L_4 \sin \alpha \sin \beta \sin \theta_{01} = (L_4 \cos \alpha \sin \theta_{01} / \sin \bar{\theta}_1) \cos \bar{\theta}_1 \quad (5.16)$$

Finally, Eqs. ((5.7), (5.15), (5.16)) and constraint equation Eq. (5.12) are used to solve θ_{01} , θ_{02} , α , β .

3. Three joint angles are measured, e.g. $\bar{\theta}_1, \bar{\theta}_2, \bar{\theta}_3$. In addition, the projected configuration has another close loop kinematic constraint, written as

$$\bar{L}_1 + \bar{L}_2 \cos(\pi - \bar{\theta}_2) = \bar{L}_4 \cos \bar{\theta}_1 + \bar{L}_3 \cos(\psi_3), \quad (5.17)$$

$$\bar{L}_2 \sin(\pi - \bar{\theta}_2) = \bar{L}_4 \sin \bar{\theta}_1 + \bar{L}_3 \sin(\psi_3), \quad (5.18)$$

where

$$\begin{aligned} \bar{\theta}_4 &= 2\pi - (\bar{\theta}_1 + \bar{\theta}_2 + \bar{\theta}_3), \\ \psi_3 &= \bar{\theta}_1 + \bar{\theta}_4 - \pi. \end{aligned} \quad (5.19)$$

and the projection length variable, \bar{L}_3 can be obtained by substituting \bar{L}_2 in Eq.(5.13) and \bar{L}_4 in Eq.(5.15) into Eq.(5.18)

$$\bar{L}_3 = (L_2 \cos \alpha \sin \theta_{02} - L_4 \cos \alpha \sin \theta_{01}) / \sin(\psi_3) \quad (5.20)$$

Then $\bar{L}_1, \bar{L}_2, \bar{L}_4$ and \bar{L}_3 solved by Eqs.((5.7), (5.13), (5.15), (5.20)) are substituted into Eqs. ((5.8), (5.10), (5.17)) and obtain

$$L_1 \cos \beta - L_2 \cos \beta \cos \theta_{02} + L_2 \sin \alpha \sin \beta \sin \theta_{02} = (L_1 \cos \beta) + (L_2 \cos \alpha \sin \theta_{02} / \sin(\pi - \bar{\theta}_2)) \cos(\pi - \bar{\theta}_2) \quad (5.21)$$

$$L_4 \cos \beta \cos \theta_{01} + L_4 \sin \alpha \sin \beta \sin \theta_{01} = (L_4 \cos \alpha \sin \theta_{01} / \sin \bar{\theta}_1) \cos \bar{\theta}_1, \quad (5.22)$$

$$L_1 \cos \beta + L_2 \cos \alpha \sin \theta_{02} \cot(\pi - \bar{\theta}_2) = L_4 \cos \alpha \sin \theta_{01} \cot \bar{\theta}_1 + (L_2 \cos \alpha \sin \theta_{02} - L_4 \cos \alpha \sin \theta_{01}) \cot(\psi_3) \quad (5.23)$$

Eqs ((5.20), (5.21), (5.22)) and Eq. (5.12) are the final four equations that are used to obtain $\theta_{01}, \theta_{02}, \alpha, \beta$.

4. Three adjacent links, e.g. \bar{L}_1, \bar{L}_2 and \bar{L}_4 are measured. Based on the projected link lengths \bar{AB} and \bar{OC} , i.e. $|\bar{\mathbf{A}} - \bar{\mathbf{B}}| = \bar{L}_2, |\bar{\mathbf{O}} - \bar{\mathbf{C}}| = \bar{L}_4$, we can obtain

$$(L_4 \cos \beta \cos \theta_{01} + L_4 \sin \alpha \sin \beta \sin \theta_{01})^2 + (L_4 \cos \alpha \sin \theta_{01})^2 = \bar{L}_4^2, \quad (5.24)$$

$$(L_1 \cos \beta - L_2 \cos \beta \cos \theta_{02} + L_2 \sin \alpha \sin \beta \sin \theta_{02} - L_1 \cos \beta)^2 + (L_2 \cos \alpha \sin \theta_{02})^2 = \bar{L}_2^2, \quad (5.25)$$

Together with Eq. ((5.7), (5.12)), we can solve for the four unknowns, θ_{01} , θ_{02} , α , β .

The four cases for projection kinematic analysis of four-bar linkage and the corresponding equations are summarized in Table 5.7. Note each case is a representative case of multiple permutations.

Table 5.7: Equations and solutions of four kinds of projection kinematic analysis for the four-bar linkage

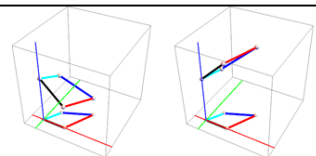
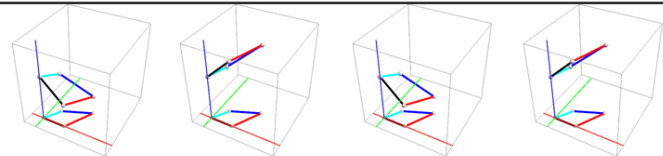
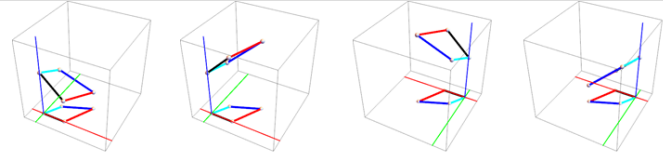
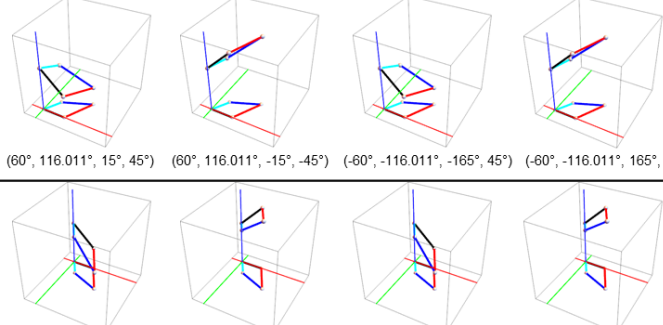
Case	Measured geometric parameters	Measured parameters	Representative Equations	# of solutions
1	Two links and the joint between them	$\bar{L}_1, \bar{L}_4, \bar{\theta}_1$	(7, 10, 11, 12)	2
2	Two adjacent joints and the link between them	$\bar{\theta}_1, \bar{L}_1, \bar{\theta}_2$	(7, 12, 15, 16)	4
3	Three joints	$\bar{\theta}_1, \bar{\theta}_2, \bar{\theta}_3$	(12, 20, 21, 22)	4
4	Three links	$\bar{L}_1, \bar{L}_2, \bar{L}_4$	(7, 12, 24, 25)	8

A numerical example is discussed below to verify the strategies introduced above. The variables of initial and projected configurations and global rotations are shown in Table 5.8.

Table 5.8: Numerical example of projection kinematic analysis of a four-bar linkage

Initial configuration	$L_1=5, L_2=5, L_3=6, L_4=3, \theta_{01}=60^\circ, \theta_{02}=116.011^\circ; \alpha = 15^\circ, \beta=45^\circ$
Projected configuration	$\bar{L}_1=3.54, \bar{L}_2=4.95, \bar{L}_3=4.74, \bar{L}_4=2.94; \bar{\theta}_1=58.53^\circ, \bar{\theta}_2=118.67^\circ, \bar{\theta}_3=38.61^\circ;$

Table 5.9: Solutions of case 1, 2, 3 and 4 of the projection kinematics analysis of planar four-bar linkage. The values of $(\theta_{01}, \theta_{02}, \alpha, \beta)$ is shown at the bottom of each 3D subfigure.

Case	Solutions
1	 $(60^\circ, 116.011^\circ, 15^\circ, 45^\circ)$ $(60^\circ, 116.011^\circ, -15^\circ, -45^\circ)$
2	 $(60^\circ, 116.011^\circ, 15^\circ, 45^\circ)$ $(60^\circ, 116.011^\circ, -15^\circ, -45^\circ)$ $(-60^\circ, -116.011^\circ, -165^\circ, 45^\circ)$ $(-60^\circ, -116.011^\circ, 165^\circ, -45^\circ)$
3	 $(60^\circ, 116.011^\circ, 15^\circ, 45^\circ)$ $(60^\circ, 116.011^\circ, -15^\circ, -45^\circ)$ $(60^\circ, 116.011^\circ, 165^\circ, -135^\circ)$ $(60^\circ, 116.011^\circ, -165^\circ, 135^\circ)$
4	 $(60^\circ, 116.011^\circ, 15^\circ, 45^\circ)$ $(60^\circ, 116.011^\circ, -15^\circ, -45^\circ)$ $(-60^\circ, -116.011^\circ, -165^\circ, 45^\circ)$ $(-60^\circ, -116.011^\circ, 165^\circ, -45^\circ)$ $(60^\circ, 116.011^\circ, 165^\circ, 45^\circ)$ $(60^\circ, 116.011^\circ, -165^\circ, -45^\circ)$ $(-60^\circ, -116.011^\circ, -15^\circ, 45^\circ)$ $(-60^\circ, -116.011^\circ, 15^\circ, -45^\circ)$

The equations in case 1 and 2 can be solved easily. However, the equations derived in case 3 and 4 are too complex to be solved directly. Instead, we used the polynomial homotopy solver PHCPack [17] to find the solutions of case 3 and 4. To obtain polynomial equations, we defined c and s for $\cos(\bullet)$ and $\sin(\bullet)$ functions and introduce the extra identical equation $c^2+s^2=1$ for each angle variable. The eight equations for case 3 and 4 respectively are imported into the PHCPack. Finally, all solutions of case 1, 2, 3 and 4 are summarized in Table 5.9. For each solution, the spatial and projected configurations are presented in a boxed figure and the values of the unknowns, $(\theta_{01}, \theta_{02}, \alpha, \beta)$ are shown at the bottom of each figure.

5.3.2. Planar five-bar linkage

In order to further test the projection kinematics routine, we considered a general planar five-bar linkage. Here we focus on only one case, i.e. measuring joint angles only. The planar five-bar linkage has two DOFs that will bring in two extra input unknowns and together with the two global rotation variables, four total unknowns need to be solved, which means we need to measure at least four angles to solve the projection kinematics equations.

Planar five-bar linkage consists of five links connected by five revolute joints (Figure 5.9(a)), when θ_{01} and θ_{02} are given, the configuration of the five-bar linkage is determined but not unique due to the existence of multiple solutions of θ_{03} . To uniquely determine the true configuration, we must rely on extra information to pick the correct solution of θ_{03} . Figure 5.9(b) shows the sketch of the projection after the global rotations about x -axis and y -axis and the projected configuration is shown in details in Figure 5.9(c). Four

adjacent joint angles, $\bar{\theta}_1$, $\bar{\theta}_2$, $\bar{\theta}_3$ and $\bar{\theta}_4$ will be measured and used for the projection kinematic analysis of the five-bar linkage. Table 5.10 presents the joints positions of initial, rotated and projected configurations of five-bar linkage.

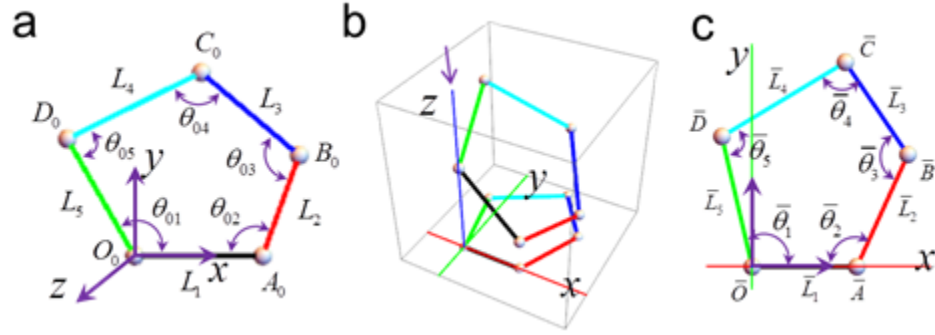


Figure 5.9: Projection kinematic analysis of a planar five-bar linkage. (a) The local coordinate frame is defined. (b) The planar five-bar linkage in space and its projection onto xy plane. (c) The detailed projected configuration.

Table 5.10: Initial, rotated, projected and measured points that define the structure of planar five-bar linkage

Points in the local reference frame	Points After Rotation	Projected points	Measured points from a 2D image
$\mathbf{A}_0 = (L_1, 0, 0)^T$	$\mathbf{A} = [R]\mathbf{A}_0$	$\bar{\mathbf{A}} = [P]\mathbf{A}$	$\bar{\mathbf{A}} = (\bar{L}_1, 0, 0)^T$
$\mathbf{B}_0 = \mathbf{A}_0 + L_2(-\cos(\theta_{02}), \sin(\theta_{02}), 0)^T$	$\mathbf{B} = [R]\mathbf{B}_0$	$\bar{\mathbf{B}} = [P]\mathbf{B}$	$\bar{\mathbf{B}} = \bar{\mathbf{A}} + (-\bar{L}_2 \cos(\bar{\theta}_2), \bar{L}_2 \sin(\bar{\theta}_2), 0)^T$
$\mathbf{C}_0 = \mathbf{B}_0 + (L_3 \cos(\theta_{02} + \theta_{03}), L_3 \sin(-(\theta_{02} + \theta_{03})), 0)^T$	$\mathbf{C} = [R]\mathbf{C}_0$	$\bar{\mathbf{C}} = [P]\mathbf{C}$	$\bar{\mathbf{C}} = \bar{\mathbf{B}} + (\bar{L}_3 \cos(\bar{\theta}_2 + \bar{\theta}_3), \bar{L}_3 \sin(-(\bar{\theta}_2 + \bar{\theta}_3)), 0)^T$
$\mathbf{D}_0 = (L_5 \cos \theta_{01}, L_5 \sin \theta_{01}, 0)^T$	$\mathbf{D} = [R]\mathbf{D}_0$	$\bar{\mathbf{D}} = [P]\mathbf{D}$	$\bar{\mathbf{D}} = (\bar{L}_5 \cos \bar{\theta}_1, \bar{L}_5 \sin \bar{\theta}_1, 0)^T$

Equating the coordinates of projected points (3rd column) with measured points (4th column) in Table 5.10 yields seven equations,

$$\begin{cases} L_1 \cos \beta = \bar{L}_1 \\ L_1 \cos \beta - L_2 \cos \beta \cos \theta_{02} + L_2 \sin \alpha \sin \beta \sin \theta_{02} = \bar{L}_1 + \bar{L}_2 \cos(\pi - \bar{\theta}_2) \\ L_2 \cos \alpha \sin \theta_{02} = \bar{L}_2 \sin(\pi - \bar{\theta}_2) \\ L_1 \cos \beta - L_2 \cos \beta \cos \theta_{02} + L_3 \cos \beta \cos(\theta_{02} + \theta_{03}) + L_2 \sin \alpha \sin \beta \sin \theta_{02} - L_3 \sin \alpha \sin \beta \sin(\theta_{02} + \theta_{03}) \\ = \bar{L}_1 + \bar{L}_2 \cos(\pi - \bar{\theta}_2) + \bar{L}_3 \cos(\bar{\theta}_2 + \bar{\theta}_3), \\ L_2 \cos \alpha \sin \theta_{02} - L_3 \cos \alpha \sin(\theta_{02} + \theta_{03}) = \bar{L}_2 \sin(\pi - \bar{\theta}_2) + \bar{L}_3 \sin(-(\bar{\theta}_2 + \bar{\theta}_3)) \\ L_5 \cos \beta \cos \theta_{01} + L_5 \sin \alpha \sin \beta \sin \theta_{01} = \bar{L}_5 \cos \bar{\theta}_1 \\ L_5 \cos \alpha \sin \theta_{01} = \bar{L}_5 \sin \bar{\theta}_1 \end{cases} \quad (5.26)$$

Based on the coordinate frame in Figure 5.9(a), the geometry constraint equation is

$$|\mathbf{C}_0 - \mathbf{D}_0| - L_4^2 = 0 . \quad (5.27)$$

In addition, the vector loop of the projected configuration leads two additional constraint equations

$$\begin{cases} \bar{L}_1 - \bar{L}_2 \cos \bar{\theta}_2 + \bar{L}_3 \cos(\bar{\theta}_2 + \bar{\theta}_3) - \bar{L}_5 \cos \bar{\theta}_1 + \bar{L}_4 \cos(\bar{\theta}_1 + \bar{\theta}_5) = 0 \\ \bar{L}_2 \sin \bar{\theta}_2 - \bar{L}_3 \sin(\bar{\theta}_2 + \bar{\theta}_3) - \bar{L}_5 \sin \bar{\theta}_1 + \bar{L}_4 \sin(\bar{\theta}_1 + \bar{\theta}_5) = 0 \end{cases} \quad (5.28)$$

Finally, we obtained ten total equations, Eqs. ((5.26), (5.27), (5.28)), for the projection kinematics analysis of the planar five-bar mechanism. First, \bar{L}_1 , \bar{L}_2 , \bar{L}_3 , \bar{L}_4 , and \bar{L}_5 should be eliminated and only five equations with five unknowns, θ_{01} , θ_{02} , θ_{03} , α and β , are kept. Then the five equations, along with the five identical equation $c^2+s^2=1$ for each angle variable, can be solved by the PHCpack solver. The redundant solutions can be eliminated by checking the four measured projected joint angles and the projected link length, and finally we obtained four solutions with all of them have the same

configuration as the designed one. A numerical example of projection analysis of a five-bar linkage was shown in Table 5.11.

Table 5.11: Numerical example of projection kinematics analysis of a five-bar linkage

Initial configuration	$L_1=2, L_2=5/3, L_3=2, L_4=7/3, \theta_{01}=120^\circ, \theta_{02}=110^\circ, \theta_{03}=110.119^\circ; \alpha = 15^\circ, \beta=45^\circ$
Projected configuration	$\bar{L}_1=1.414, \bar{L}_2=1.663, \bar{L}_3=1.505, \bar{L}_4=1.945, \bar{L}_5=1.804; \bar{\theta}_1=103.126^\circ, \bar{\theta}_2=114.509^\circ, \bar{\theta}_3=121.303^\circ, \bar{\theta}_4=93.22^\circ, \bar{\theta}_5=107.842^\circ;$

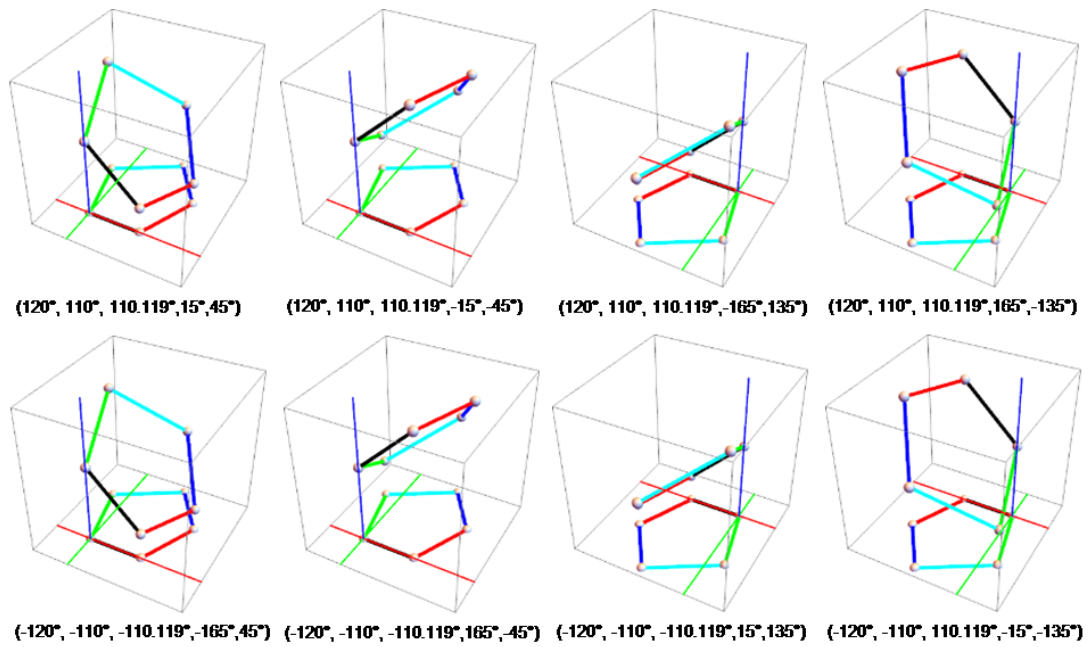


Figure 5.10: Solutions of the projection kinematics analysis of planar five-bar linkage. The $(\theta_{01}, \theta_{02}, \theta_{03}, \alpha, \beta)$ for each solution is shown at the bottom of each subfigure.

The eight solutions are shown in Figure 5.10. The first four solutions have the same configuration as designed but with four different orientations in 3D space, while the last four solutions are the mirrored configurations, also with four different orientations.

5.4. Algorithm of the projection kinematics analysis

All of the projection kinematics equations can be solved when the number of unknowns equals to the number of equations, which is referred as the minimum measurement case. With minimum measurements, the projection kinematics analysis procedure is summarized as follows:

- 1) Set up the global coordinate frame of the mechanism. Specifically, it is convenient to place the x -axis along a link so that the projected link length of this link will not change if the entire mechanism has a transformation of rotation about x -axis.
- 2) Define the true configuration of the mechanism.
- 3) Conduct the global rotation about x -axis and y -axis to obtain the spatial configuration.
- 4) Project the spatial configuration to the x - y plane and obtain the symbolic equations of the projected angles and projected link lengths.
- 5) Measure the corresponding angles and link lengths from the experimental 2D image, for example a TEM image.
- 6) Obtain the minimum projection kinematics equations by comparing the variables obtained in 4) and 5).
- 7) Solve the projection kinematics equations obtained in 6). PHCpack solver can be used when the equations are complex.

- 8) Compare the projection information calculated from the solution obtained in 7) with the measured ones in 5) and keep the right solutions if the differences between them are acceptable.

In real world applications, you may have more than minimum measurements. Different measurements for the projection kinematics equations may result in different solutions with different errors. Errors mainly depend on the fabrication of the mechanisms and accuracy of measurement. In order to minimize the errors, the variables with less measurement errors should be used firstly and the quality of the solutions must be verified by extra kinematics equations or measurements. For example, $\{Q_m=0\}$ and $\{\bar{x}_n\}$ are respectively the collection of all projection kinematics equations and measurements, and $\{Q_j=0\}$ is a subset of $\{Q_m=0\}$ and has the minimum number of equations corresponding to the chosen subset of measurements $\{\bar{x}_j\}$. The error can be quantified by substituting solutions obtained by solving $\{Q_j=0\}$ into all other kinematics equations, as $\varepsilon = \sum Q_k$ ($k \neq j$). Also, the error can be termed by the derived projection variables and the extra measurements as $\delta = \sum(\bar{x}_i - \bar{x}_{i-p}) / \bar{x}_i$ ($i \neq j$). Finally, the good solutions should be those that can obtain small and acceptable errors ε and δ .

5.5. Application on DNA origami nanomechanisms

In this section, we will apply projection kinematics to the analysis of two real DNA origami mechanisms (DOM). As mentioned in the introduction section, the motivation of this research comes from the need to estimate the true configuration of DOM from a single 2D microscopy image, which is essentially the projected image of an arbitrary

mechanism in 3D space. Errors of variables measured from TEM images always exist due to the fuzzy ends or boundaries of double strand DNA bundles. The main sources of the fuzzy end or boundaries include ssDNA at the end of the link (to prevent nonspecific binding) or staining during TEM sample preparation [7,8].

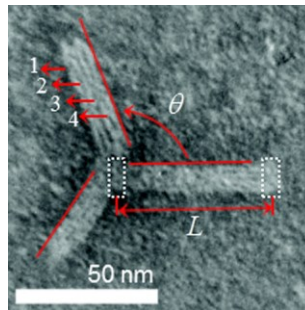


Figure 5.11: Measurements on TEM image.

Figure 5.11 shows how the projected angle and link length are measured from a TEM image and red lines are the reference lines that parallel with the helices of double strand DNA on each link. It is usually very easy to distinguish the helices of double strand DNA on TEM image, such as the four helices (labeled as 1, 2, 3 and 4) on the upper left link. The angle θ between the reference lines is measured as the projected angle and the projection link length is measured along the reference line. However, the ends of double strand DNA bundles are fuzzy. Therefore, estimated positions will be chosen for the length measurement. For example, the two ends of the horizontal link on Figure 5.11 fall in the two white boxes and the width of the white box is about 12 nm which is close to

20% of the designed link length. Here, the projection kinematics results are acceptable if the link length error between the calculation and the measurement is smaller or close to 20%.

5.5.1. Application to the DNA origami quasi universal joint TEM image analysis

The design of a quasi universal joint with DNA origami nanotechnology has been described in [49]. Here, we use the quasi universal joint as an example of an open chain mechanism for demonstrating the application of projection kinematics for the analysis of 2D transmission electronic microscopy (TEM) images. The dimension information is also represented in the Figure 5.12.

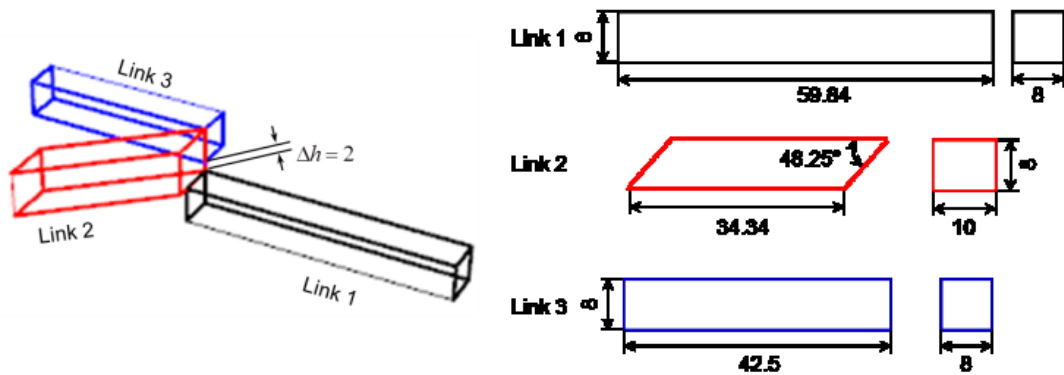


Figure 5.12: Dimension of the universal joint, unit: nm.

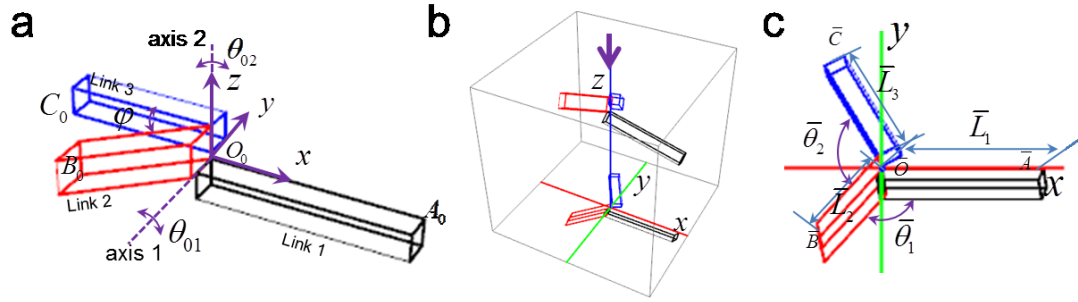


Figure 5.13: Projection kinematics analysis of quasi universal joint. (a, b, c) are the local coordinate frame, sketch of the projection configuration and projected configuration of the quasi universal joint respectively.

In addition, the conceptual design of the universal joint and the initial position are shown in Figure 5.13(a). Axis 1, constructed by the shared edge between link 1 and link 2, and axis 2, constructed by the edge between link 2 and link 3, intersect at a point, which is also chosen as the origin position of the global coordinate frame. θ_{01} and θ_{02} are the initial rotation angles of the two joints respectively. To be clear, the spatial and projected configurations are shown in Figure 5.13(b) and Figure 5.13(c) respectively.

Here, we picked A_0 , B_0 and C_0 on the three links respectively as the primary points to explain the solution process. Other points on each link could also be used following a similar computing procedure. The rotation matrix about the two hinge joint are defined as

$$[Y(\theta_{01})] = \begin{bmatrix} \cos \theta_{01} & 0 & \sin \theta_{01} \\ 0 & 1 & 0 \\ -\sin \theta_{01} & 0 & \cos \theta_{01} \end{bmatrix}, [Z(\theta_{02})] = \begin{bmatrix} \cos \theta_{02} & -\sin \theta_{02} & 0 \\ \sin \theta_{02} & \cos \theta_{02} & 0 \\ 0 & 0 & 1 \end{bmatrix}. \quad (5.29)$$

Then the coordinates of points A_0 , B_0 and C_0 on the true, rotated and projected configurations are derived and presented in

Table 5.12.

Table 5.12: Initial, rotated, projected and measured points that define the structure of quasi universal joint

True configuration points	Points after rotation	Projected points	Measured points from a 2D image
$\mathbf{A}_0 = (L_1, 0, 0)^T$	$\mathbf{A} = [R]\mathbf{A}_0$	$\bar{\mathbf{A}} = [P]\mathbf{A}$	$\bar{\mathbf{A}} = (\bar{L}_1, 0, 0)^T$
$\mathbf{B}_0 = (-L_2 \cos \varphi, -L_2 \sin \varphi, 0)^T$	$\mathbf{B} = [R][Y(\theta_{01})]\mathbf{B}_0$	$\bar{\mathbf{B}} = [P]\mathbf{B}$	$\bar{\mathbf{B}} = (\bar{L}_2 \cos(-\bar{\theta}_1), \bar{L}_2 \sin(-\bar{\theta}_1), 0)^T$
$\mathbf{C}_0 = (-L_3, 0, \Delta h)^T$	$\mathbf{C} = [R][Y(\theta_{01})][Z(\theta_{02})]\mathbf{C}_0$	$\bar{\mathbf{C}} = [P]\mathbf{C}$	$\bar{\mathbf{C}} = (\bar{L}_3 \cos(-\bar{\theta}_1 - \bar{\theta}_2), \bar{L}_3 \sin(-\bar{\theta}_1 - \bar{\theta}_2), 0)^T$

Note: Δh is the design variable that is shown in Figure 5.12.

Equating the coordinates of projected (3rd column) and measured points (4th column) in

Table 10, we obtain five equations

$$\begin{cases} L_1 \cos \beta = \bar{L}_1 \\ L_2(-\cos \beta \cos \theta_{01} \cos \varphi + \cos \alpha \sin \beta \sin \theta_{01} \cos \varphi - \sin \alpha \sin \beta \sin \varphi) = \bar{L}_2 \cos \bar{\theta}_1 \\ L_2(\sin \alpha \sin \theta_{01} \cos \varphi + \cos \alpha \sin \varphi) = \bar{L}_2 \sin \bar{\theta}_1 \\ L_3(-\cos \beta \cos \theta_{01} \cos \theta_{02} + \cos \alpha \sin \beta \sin \theta_{01} \cos \theta_{02} - \sin \alpha \sin \beta \sin \theta_{02}) = \bar{L}_3 \cos(-\bar{\theta}_1 - \bar{\theta}_2) \\ L_3(-\sin \alpha \sin \theta_{01} \cos \theta_{02} - \cos \alpha \sin \theta_{02}) = \bar{L}_3 \sin(-\bar{\theta}_1 - \bar{\theta}_2) \end{cases} \quad (5.30)$$

The unknowns α , β , θ_{01} and θ_{02} can be easily solved from Eq. (5.30) if $\bar{\theta}_1$, $\bar{\theta}_2$, \bar{L}_1 , and \bar{L}_2 are measured from the projected configuration. The solution of \bar{L}_3 can be used as a criterion for picking the correct configuration. Finally, a total of sixteen groups of solutions including the initially specified one are obtained. The other fifteen groups of solutions do not satisfy the projection information including the projected angles and links.

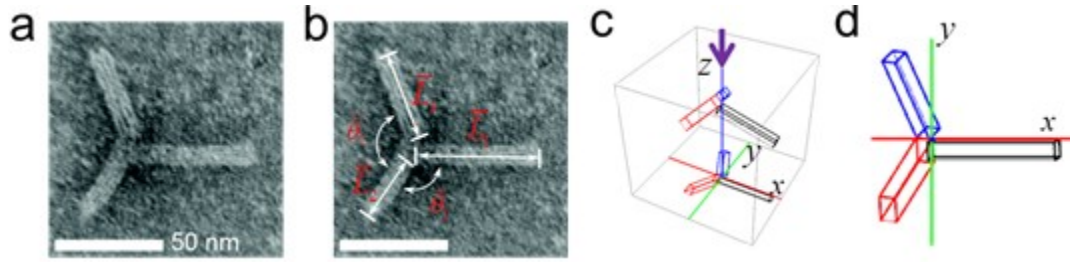


Figure 5.14: Projection kinematics analysis of the quasi universal joint based on the TEM image. (a) A typical TEM image of the DNA origami universal joint. (b) The projection information that can be measured from the TEM image. (c) 3D projection solution of the TEM image sample. (d) The detailed projected configuration of the solution.

The experimental methods and results are discussed in [49]. Here, one typical universal joint TEM image is shown in Figure 5.14(a). $\bar{\theta}_1$, $\bar{\theta}_2$, \bar{L}_1 , \bar{L}_2 and \bar{L}_3 are measured from the TEM image (Figure 5.14(b)) which are shown in Table 5.13. All measurements were conducted by ImageJ and the value of each measured variable value is the average value of three repeated measurements.

Table 5.13: Projection kinematic analysis of a DNA origami quasi universal joint

True configuration	$L_1=59.84\text{nm}, L_2=34.34 \text{ nm}, L_3=49.3\text{nm}; \varphi=41.75^\circ$
Projected configuration	$\bar{L}_1=57.29, \bar{L}_2=31.38, \bar{L}_3=37.52, \bar{\theta}_1=122.20^\circ, \bar{\theta}_2=123.49^\circ$
Solution	$\theta_{01}=-62.12^\circ, \theta_{02}=-62.99^\circ; \alpha=-10.32^\circ, \beta=16.79^\circ$
Projected variables calculated from the solution	$\bar{L}_{1-p}=57.29, \bar{L}_{2-p}=31.38, \bar{L}_{3-p}=39.18, \bar{\theta}_{1-p}=122.20^\circ, \bar{\theta}_{2-p}=123.49^\circ$

The final solution is chosen based on the following criteria:

1. The projected angle calculated from the model, $\bar{\theta}_{1-p}$ and $\bar{\theta}_{2-p}$, are the same as those from measurements, $\bar{\theta}_1$ and $\bar{\theta}_2$.
2. The projected link lengths \bar{L}_{1-p} and \bar{L}_{2-p} calculated from the model are the same as from measurements, \bar{L}_1 and \bar{L}_2 ,
3. The projected link length \bar{L}_{3-p} calculated from the model should be as close from measurement \bar{L}_3 as possible.

Here, the difference between \bar{L}_3 and \bar{L}_{3-p} is about 4.42%. Figure 5.14(c) shows the 3D projection of the solution and Figure 5.14(d) shows the projected configuration of the universal joint in details.

5.5.2. Application of projection kinematics analysis on the DNA origami Bennett linkage

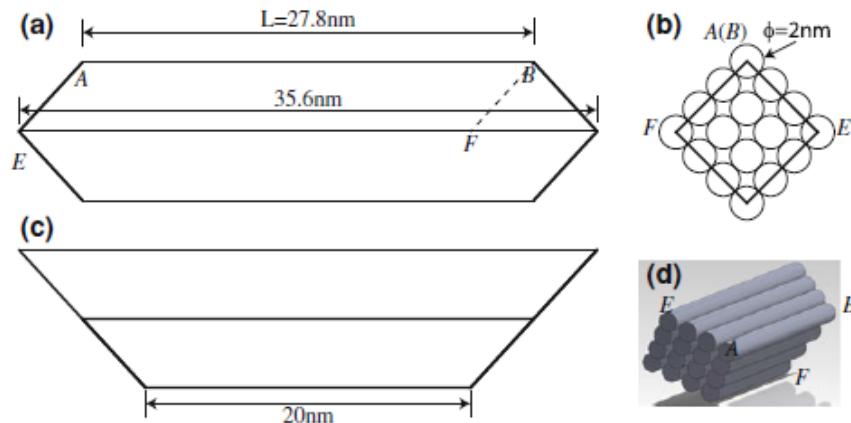


Figure 5.15: Dimension of the Bennett linkage.

We previously reported the design of the Bennett linkage [6,12]. The details of its dimensions are shown in Figure 5.15.

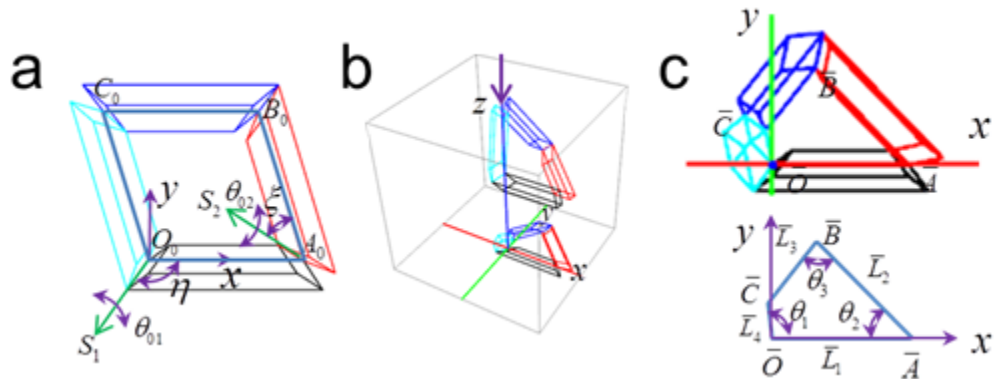


Figure 5.16: Projection kinematics analysis of the Bennett linkage. (a, b and c) are the local coordinate frame, sketch of the projection configuration and projected configuration of the Bennett linkage respectively.

In addition, Figure 5.16(a) shows the sketch of the Bennett linkage, the coordinate system and the rotation angles. Here, the configuration is determined when all of the points O_0 , A_0 , B_0 and C_0 are in the same plane and this plane is chosen as the x-y plane of the global coordinate frame. The lengths of the four edges are equal to L . The same as previous examples, α and β are the global rotation angles used to determine the pose of the Bennett linkage is spatial. Figure 5.16(b) shows the Bennett linkage in spatial and its projected configuration. Here, we only test the case 3 discussed in previous section,

which can solve the projection kinematics equations based on three projected angles. Figure 5.16(c) shows the projected configuration of the Bennett linkage in 2D and the three angles, $\bar{\theta}_1$, $\bar{\theta}_2$, and $\bar{\theta}_3$ that can be obtained from the quadrilateral determined by the inner boundaries (bottom of Figure 5.16(c)). The link lengths \bar{L}_1 , \bar{L}_2 , \bar{L}_3 and \bar{L}_4 can be used to eliminate extraneous solutions. The kinematics equations of the Bennett linkage are discussed in

Table 5.14.

Table 5.14: Initial, rotated, projected and measured points that define the structure of DNA origami Bennett linkage

Points in the local reference frame	Points after rotation	Projected points	Measured points
$\mathbf{A}_0 = (L, 0, 0)^T$	$\mathbf{A} = [R]\mathbf{A}_0$	$\bar{\mathbf{A}} = [P]\mathbf{A}$ $= (A_x, 0, 0)^T$	$\bar{\mathbf{A}} = (\bar{L}_1, 0, 0)^T$
$\mathbf{B}_0 = \mathbf{A}_0 + [e^{\theta_2 S_2}] \begin{Bmatrix} -L \\ 0 \\ 0 \end{Bmatrix}$	$\mathbf{B} = [R]\mathbf{B}_0$	$\bar{\mathbf{B}} = [P]\mathbf{B}$ $= (B_x, B_y, 0)^T$	$\bar{\mathbf{B}} = \bar{\mathbf{A}} + (-\bar{L}_2 \cos(\bar{\theta}_2), \bar{L}_2 \sin(\bar{\theta}_2), 0)^T$
$\mathbf{C}_0 = [e^{\theta_1 S_1}] \begin{Bmatrix} L \\ 0 \\ 0 \end{Bmatrix}$	$\mathbf{C} = [R]\mathbf{C}_0$	$\bar{\mathbf{C}} = [P]\mathbf{C}$ $= (C_x, C_y, 0)^T$	$\bar{\mathbf{C}} = (\bar{L}_4 \cos \bar{\theta}_1, \bar{L}_4 \sin \bar{\theta}_1, 0)^T$

Note: A_x, B_x, B_y, C_x and C_y are used to represent the coordinates elements because the explicit expressions of them are too complex.

Again, equating the coordinates of projected and measured points in Table 13, we can obtain five equations

$$A_x = \bar{L}_1, B_x = \bar{L}_1 + \bar{L}_2 \cos(\pi - \bar{\theta}_2), B_y = \bar{L}_2 \sin(\pi - \bar{\theta}_2), C_x = \bar{L}_4 \cos \bar{\theta}_1, C_y = \bar{L}_4 \sin \bar{\theta}_1 \quad (5.31)$$

The geometric constraint equation is given by the length of top blue link

$$(\mathbf{B}_0 - \mathbf{C}_0) \cdot (\mathbf{B}_0 - \mathbf{C}_0) - L^2 = 0, \quad (5.32)$$

and θ_{02} can be solved from this equation when θ_{01} is given.

Similar to the case of planar four-bar linkages, the closed-loop of the projected configuration introduces two additional constraint equations Eqs. ((5.17), (5.18)). Together with Eqs. ((5.31), (5.32)), eight equations are obtained. \bar{L}_1 , \bar{L}_2 , \bar{L}_3 and \bar{L}_4 are eliminated first, then the left four equations are the minimum equations that can be used to solve for θ_{01} , θ_{02} , α and β .

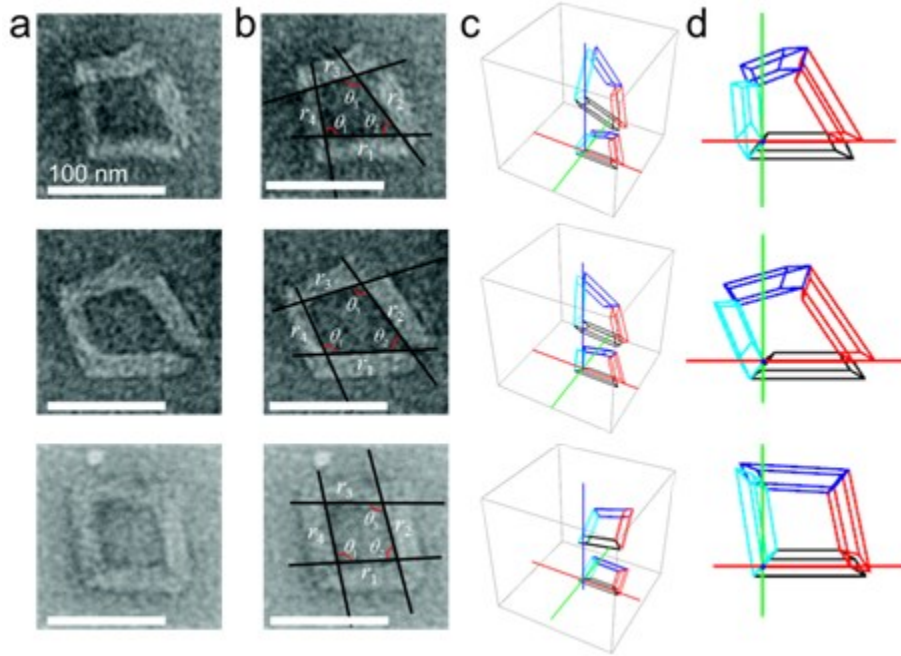


Figure 5.17: Analysis of the projection kinematic of the Bennett linkage based on the TEM image.(a) Typical TEM images of the Bennett linkage. (b) The projection

information measured from the TEM image. (c) 3D projection solution of the TEM image sample. (d) The detailed projected configuration of the solution.

Table 5.15: Measurements, projection kinematics solution and projection results from the model, errors of link lengths between the experiment measurements and projection kinematics analysis of DNA origami Bennett linkage (examples 1, 2, and 3 corresponding to the three examples in Figure 5.17 from top to bottom respectively), unit for length: nm.

E.g	Measurements	Solutions	Projection results from the model	Average error of the link length
1	$\bar{\theta}_1 = 101.05^\circ$, $\bar{\theta}_2 = 52.52^\circ$, $\bar{\theta}_3 = 110.19^\circ$, $\bar{L}_1 = 31.64$, $\bar{L}_2 = 31.20$, $\bar{L}_3 = 16.93$, $\bar{L}_4 = 19.71$	$\theta_{01} = 155.85^\circ$, $\theta_{02} = 67.25^\circ$, $\alpha = -2.33^\circ$, $\beta = 22.24^\circ$	$\bar{\theta}_{1-p} = 101.05^\circ$, $\bar{\theta}_{2-p} = 52.52^\circ$, $\bar{\theta}_{3-p} = 110.19^\circ$, $\bar{L}_{1-p} = 25.73$, $\bar{L}_{2-p} = 26.50$, $\bar{L}_{3-p} = 17.55$, $\bar{L}_{4-p} = 14.58$,	15.9%
2	$\bar{\theta}_1 = 113.25^\circ$, $\bar{\theta}_2 = 55.48^\circ$, $\bar{\theta}_3 = 109.18^\circ$, $\bar{L}_1 = 35.29$, $\bar{L}_2 = 35.03$, $\bar{L}_3 = 24.11$, $\bar{L}_4 = 25.89$	$\theta_{01} = 154.88^\circ$, $\theta_{02} = 66.93^\circ$, $\alpha = -2.47^\circ$, $\beta = 5.74^\circ$	$\bar{\theta}_{1-p} = 122.20^\circ$, $\bar{\theta}_{2-p} = 123.49^\circ$, $\bar{\theta}_{3-p} = 123.49^\circ$, $\bar{L}_{1-p} = 27.66$, $\bar{L}_{2-p} = 27.48$, $\bar{L}_{3-p} = 18.82$, $\bar{L}_{4-p} = 20.24$	21.7%
3	$\bar{\theta}_1 = 99.138^\circ$, $\bar{\theta}_2 = 78.27^\circ$, $\bar{\theta}_3 = 105.027^\circ$, $\bar{L}_1 = 25.89$, $\bar{L}_2 = 25.07$, $\bar{L}_3 = 24.59$, $\bar{L}_4 = 25.67$	$\theta_{01} = -124.83^\circ$, $\theta_{02} = 104.99^\circ$, $\alpha = 32.41^\circ$, $\beta = -9.57^\circ$	$\bar{\theta}_{1-p} = 99.138^\circ$, $\bar{\theta}_{2-p} = 78.27^\circ$, $\bar{\theta}_{3-p} = 105.027^\circ$, $\bar{L}_{1-p} = 27.41$, $\bar{L}_{2-p} = 25.38$, $\bar{L}_{3-p} = 25.42$, $\bar{L}_{4-p} = 27.90$	4.8%

The experimental analysis of the Bennett linkage fabricated by scaffolded DNA origami was described in [7]. Here three different TEM images of the Bennett linkage were picked, and each of them correspond to an individual Bennett linkage (Figure 5.17(a)). Seven variables, $\bar{\theta}_1$, $\bar{\theta}_2$, $\bar{\theta}_3$, \bar{L}_1 , \bar{L}_2 , \bar{L}_3 and \bar{L}_4 were measured from each TEM images (Figure 5.17(b) and Table 5.15), and the measured three angles were used to solve the projection kinematics equations, and the measured link lengths were used to verify the solutions and only the one that can produce the minimum error between the derived projection link lengths and the measurements can be kept. The second column of the Table 5.15 shows the obtained solution and the corresponding spatial and projection configuration are shown in Figure 5.17(c,d). The errors between the link lengths of the three TEM images and projected configurations derived from the solutions are 15.9%, 21.7% and 4.8% respectively (Column 4 of Table 5.15).

5.6. Summary and discussion

In this chapter, we introduced the concept of the projection kinematics that can be used to identify the possible configurations of mechanisms by only analyzing their 2D projected images. The motivation of this research comes from the need for the verification of the kinematics of DNA origami mechanisms (DOM). These DOM are self-assembled by programmed DNA base pairing and function much like macroscopic mechanisms. We started with the projection kinematics analysis of revolute, prismatic, cylindrical and spherical joints and then extend it to general planar mechanisms. For planar mechanisms, we can always determine the unique configuration if the rotation

directions of the joint can be distinguished from the projection image. For analysis of spatial linkages and application to real world DNA origami mechanism samples, we studied universal joints and the Bennett four-bar linkage. We concluded that the estimated configurations of DOM are close to our initial mechanism because they followed the kinematics constraints fairly well. Moreover, unique solutions may be obtained if two images taken from different directions are used for the projection kinematics analysis since the correct solution must be the common solution of the analyses based on the two projection images. Finally, the existence of multiple solutions suggests that it is important to design extra feature on the structures to eliminate the ambiguity.

Chapter 6: Origami Inspired Design of Reconfigurable Nanostructures with DNA Origami

Origami provides feasible and flexible approaches for novel civil structures, robot and material designs and fabrication at macro/micro scale. Based on the ability to program DNA self-assembly, DNA origami nanotechnology is enriching the fabrication of static and dynamic nanostructures with DNA as the underlying construction material. Here, we expand the capabilities to design DNA origami nanodevices with drastic shape transformations by mimicking the waterbomb base paper origami design. In particular we followed the waterbomb base design used in thick panel origami. A six-link-joint-spatial dynamic waterbomb base linkage was designed, fabricated and actuated by DNA origami nanotechnology. Its shape transformation capability was demonstrated by actuating the linkage into triangular, rectangular and fully-compacted configurations, respectively. This multi degree of freedom nanostructure can be a foundational element of functional biomaterials or innovative design of nanomachines.

6.1. Background and motivation

As an art of three-dimensional construction, paper-based origami enables the fabrication the fabrication of arbitrary three-dimensional structures based on the folding

along valley and mountain creases pre-assigned on a two-dimensional thin sheet [119]. Without assembly, fabrication of origami structures is simplified and microscale or even nanoscale origami structure designs can also be built [120–122]. Recently the paper origami principle has been successfully applied to the design of novel materials [123,124], foldable robots [125,126] and deployable structures [127–129]. While the traditional origami folding art neglects the material thickness, some noticeable efforts have enabled the design of foldable structures out of thick (nonzero) panels at the macro [121], micro and nano scale [122].

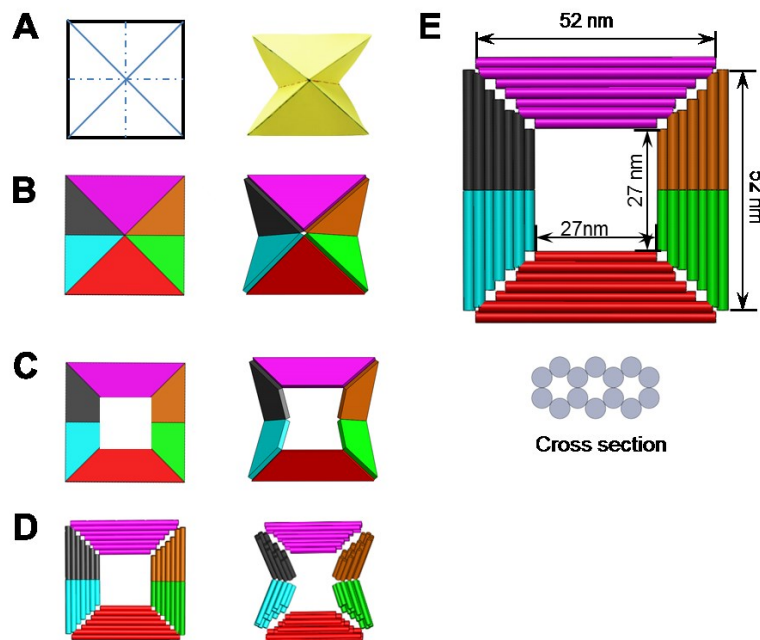


Figure 6.1: Design procedure. (A) Waterbomb base designed by a single paper. (B) Thick panel design of Waterbomb base. (C) Modified waterbomb base design with a square portion was removed at center. (D) Cylinder model of our waterbomb base design. (E) Dimensions and cross section of the waterbomb base.

DNA nanotechnology, specifically DNA origami, has enabled the self-assembly of nanostructures with unprecedented 2D and 3D geometric complexity. As shown in previous chapters, complex dynamic nanostructures have been designed and fabricated by scaffolded DNA origami following a macroscopic machine design philosophy, including classic linkages and joints, such as the Bennett linkage, prismatic joint, compliant hinge, and four-bar bistable linkages [30,31,39,40]. However, most of the fabricated dynamic nanostructures have only one degree-of-freedom (DOF) and can only achieve single function or dual configuration transformation [47,130,131].

Here, a Waterbomb base was designed by DNA origami (Figure 6.1) based on thick panel origami method. The entire size of the design is about $52\text{nm} \times 52\text{nm}$ for the outside square and all of the double helices are aligned parallel to the edges of the square. A small square ($\sim 27\text{nm} \times 27\text{nm}$) was cut at the center of the square in order to avoid short helices due to the sharp angle of the triangle shape. Very short helices may have insufficient base-pair binding energy leading to poor folding results. Each link has fourteen dsDNA helices arranged in two honeycomb layers (Figure 6.1). The four mountain creases at four corners and two valley creases at waist correspond to four diagonal and two waist revolute joints, respectively. Each revolute joint is constructed by two connections consisting of four or six ssDNA bases on the scaffold (Figure 6.2).

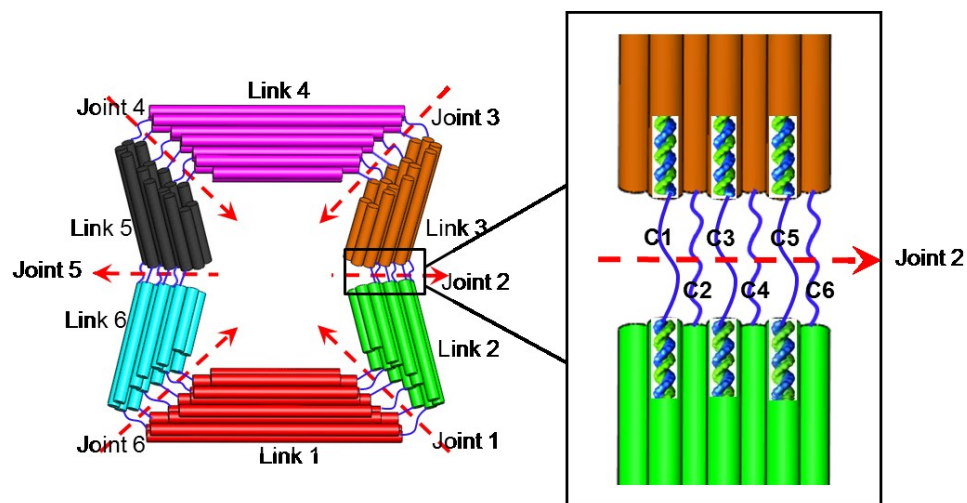


Figure 6.2: Construction of joints. Detailed length for each connection can be found in Table 6.1.

Table 6.1: Detailed design parameters of joints

Connection	C1(nt)	C2(nt)	C3(nt)	C4(nt)	C5(nt)	C6(nt)
Joint 1	4	20	4	22	6	21
Joint 2	4	20	4	20	4	20
Joint 3	4	20	4	20	6	20
Joint 4	4	20	4	20	6	20
Joint 5	4	20	4	20	4	20
Joint 6	4	20	4	20	6	20

In order to avoid base stacking, extra ssDNA bases on the scaffold are left at the ends of double helices on the mating surfaces between two connecting links. These extra ssDNA strands at the end of double helices can cause steric or charge repulsion effects

that force joints have some initial joint angles so that the waterbomb base structure tends to avoid the flat configuration. The completely flat configuration is a singularity position where folding into other configurations is challenging (Table 6.1).

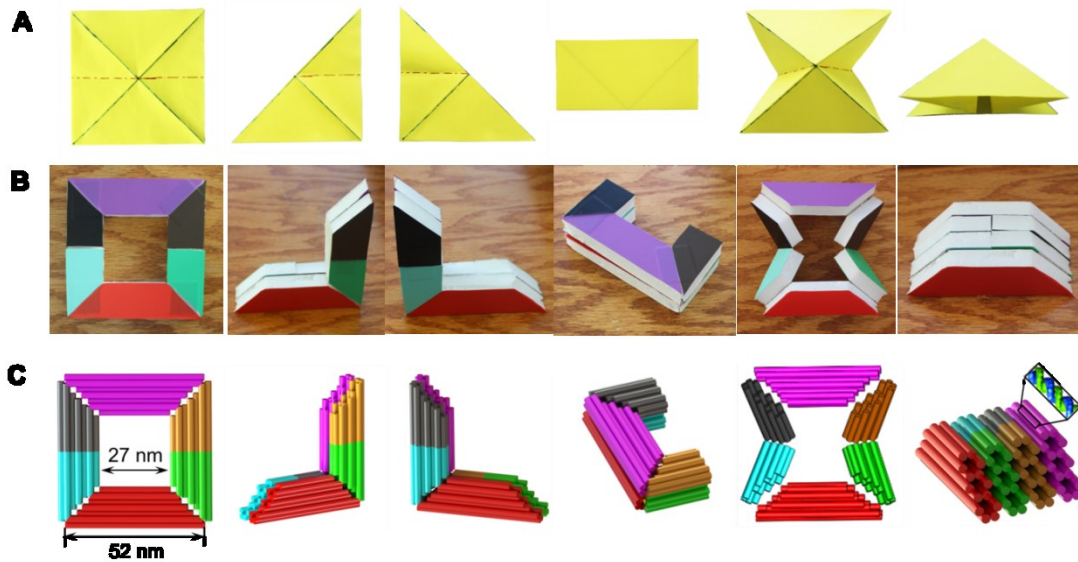


Figure 6.3: 3D folding design of waterbomb base. (A) The waterbomb base folded by a single thin paper and its square, triangle, rectangle, intermediate, compact configurations (from left to right). (B) Thick panel Waterbomb base design. (C) Cylinder model of DNA origami Waterbomb base.

At the flat square configuration, the waterbomb has three degree of freedoms, which correspond to folding along the two diagonal creases toward the triangle configurations and folding along the waist crease towards the one rectangle configuration. In addition, when all of six joints are closed, a final folded compact configuration can be achieved. In this way, the scaling ratio of the folding can reach 0.25, which is ratio between the top

surface area of square and final compact configurations (Figure 6.3). All of the joints can be closed by binding of DNA actuation strands, and reversed by the strand displacement method. The actuation strands bind to two overhangs extended eight bases from staple ends that point outwards from link body on adjacent links. For example, joint J1 can be actuated by an actuation strand that binds to overhangs on the surface of both link 2 and link 1. Each joint has at least four pairs of overhangs that can be bound by complementary ssDNA strands, which we refer to as actuation staples. In order to demonstrate that all of folded configurations are reversible, a toehold consisting of five bases is added at the end of each actuation staple so that a removal staple that has the full complementary sequence of the actuation staple can be added to release the overhangs and reopen the structure.

6.2. The modeling and analysis of the waterbomb base

6.2.1. Kinematic analysis

The single waterbomb base comprised of thick panels can be modeled as a 6R (six revolute) joint closed chain spatial mechanisms (Figure 6.4). Here, without loss of generality, the red link was chosen as the frame link, and the global coordinate frame was located on the red link with the X-axis perpendicular with its lateral surface and Y-axis along the edge of the bottom surface. The coordinate frame of each joint is represented by blue lines pointing to the positive direction. Note only the Z- and X-axes of each frame are shown.

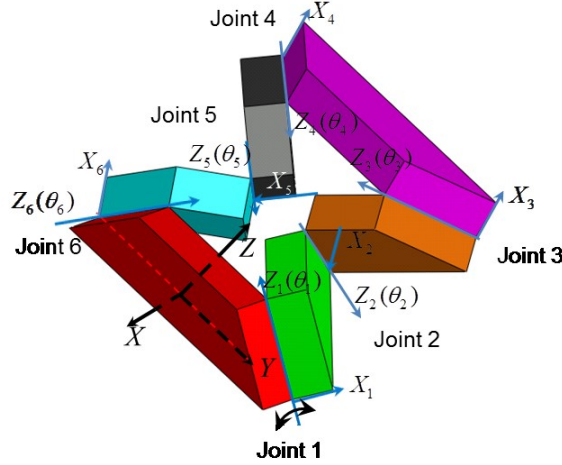


Figure 6.4: Coordinate frames and parameters for kinematics analysis.

Folding the Waterbomb base into the respective triangular or rectangular configurations requires folding of the corresponding joints. The transformation between the square and the compact configurations is a one degree-of-freedom (DOF) motion, which can be analyzed using the following kinematics analysis routine. First, we chose θ_1 as the input (driver) angle and others θ_2 to θ_6 as the output (driven) angles. Due to the known symmetric constraint, we have

$$\theta_1 = \theta_3 = -\theta_4 = -\theta_6, \theta_2 = -\theta_5 \quad (6.1)$$

The rotation matrix about the Z- and X- axes are defined by

$$R_Z(\theta) = \begin{bmatrix} \cos \theta & -\sin \theta & 0 \\ \sin \theta & \cos \theta & 0 \\ 0 & 0 & 1 \end{bmatrix}, R_X(\alpha) = \begin{bmatrix} 1 & 0 & 0 \\ 0 & \cos \alpha & -\sin \alpha \\ 0 & \sin \alpha & \cos \alpha \end{bmatrix} \quad (6.2)$$

where θ and α are the rotation angles about the Z and X axes, respectively.

In addition, screw theory was used to obtain the kinematics equations and we defined the transformation matrix for screw system as

$$[Ad] = \begin{bmatrix} R & 0 \\ DR & R \end{bmatrix} \quad (6.3)$$

where R is the 3x3 rotation matrix and D is the antisymmetric matrix of the position vector of the screw. With the position vector defined as

$$\mathbf{r} = (r_x, r_y, r_z) \quad (6.4)$$

the corresponding antisymmetric matrix is

$$D = \begin{bmatrix} 0 & -r_z & r_y \\ r_z & 0 & -r_x \\ -r_y & r_x & 0 \end{bmatrix} \quad (6.5)$$

In addition, the initial screw of the global coordinate frame is defines as

$$\mathcal{S}_0 = \{0, 0, 1, 0, 0, 0\} \quad (6.6)$$

Table 6.2: Detailed Denavit–Hartenberg parameters and obtained screws for all joints.

Joint i	α_{i-1}	a_{i-1}	d_i	θ_i	R_i	\mathbf{r}_{i-1}	\mathcal{S}_i
1	$\pi/4$	0	0	θ_1	$R_x(\pi/4)R_z(\theta_1)$	(0,0,0)	$\mathcal{S}_1 = [Ad]_1 \mathcal{S}_0$
2	$-3\pi/4$	t	0	θ_2	$R_x(-3\pi/4)R_z(\theta_2)$	($t, 0, 0$)	$\mathcal{S}_2 = [Ad]_1 [Ad]_2 \mathcal{S}_0$
3	$-3\pi/4$	$-t$	0	θ_3	$R_x(-3\pi/4)R_z(\theta_3)$	($-t, 0, 0$)	$\mathcal{S}_3 = [Ad]_1 [Ad]_2 [Ad]_3 \mathcal{S}_0$
6	$-\pi/4$	0	0	θ_6	$R_x(-\pi/4)R_z(\theta_6)$	(0,0,0)	$\mathcal{S}_4 = [Ad]_6 [Ad]_5 [Ad]_4 \mathcal{S}_0$
5	$3\pi/4$	t	0	θ_5	$R_x(3\pi/4)R_z(\theta_5)$	($t, 0, 0$)	$\mathcal{S}_5 = [Ad]_6 [Ad]_5 \mathcal{S}_0$
4	$3\pi/4$	$-t$	0	θ_4	$R_x(3\pi/4)R_z(\theta_4)$	($-t, 0, 0$)	$\mathcal{S}_4 = [Ad]_6 \mathcal{S}_0$

The screws of all joints were calculated based on the Denavit–Hartenberg parameters shown in Table 6.2. The relationship between screws of joint 3 and joint 4 are

$$\mathcal{S}_4 = [Ad]\mathcal{S}_3 \quad (6.7)$$

where $R = R_x(\pi/2)$, $\mathbf{r} = (0, 0, 0)$.

From Eq.(6.7), the relationship of joint angles θ_1 and θ_2 can be obtained as

$$-1 + \cos \theta_1^2 + \cos \theta_2 - \cos \theta_1^2 \cos \theta_2 + 2 \cos \theta_2 \sin \theta_1^2 - 2\sqrt{2} \cos \theta_1 \sin \theta_1 \sin \theta_2 = 0 \quad (6.8)$$

6.2.2. Projection kinematics analysis

As discussed in detail in Chapter 5, structure parameters measured from TEM images do not represent the true kinematic parameters, but instead the projected ones. Here, the recently developed projection kinematic analysis methods [132] was applied to obtain the true kinematic parameters based on measurements of the projected angles from TEM images. With the assumption that three points on the waterbomb lay flat on the TEM grid, projection plane are defined by the three corner points of three links, P_1 , P_2 and P_3 shown in Figure 6.5(A). The projection angles, $\bar{\theta}_1$ and $\bar{\theta}_2$ are respectively calculated by the corresponding projection vectors, which can be derived from the real link edge vectors based on the following equation

$$\bar{\mathbf{v}} = \mathbf{v} - (\mathbf{v} \cdot \mathbf{n})\mathbf{n} \quad (6.9)$$

$\bar{\mathbf{v}}$ is the projection vector, \mathbf{v} is the real link edge vector, and \mathbf{n} is the unit normal vector of the projection plane.

The relationship between projection angles $\bar{\theta}_1$ and $\bar{\theta}_2$ can be derived from the projection configuration (Figure 6.5(A)) directly, $\bar{\theta}_2 = 2\bar{\theta}_1$. The relationship between the real joint angle θ_1 and projection angle $\bar{\theta}_1$ is presented in Figure 6.5(C). If a projection angle $\bar{\theta}_1$ is measured from a TEM image, the real joint angle θ_1 , and correspondingly the real waterbomb base configuration, can be obtained.

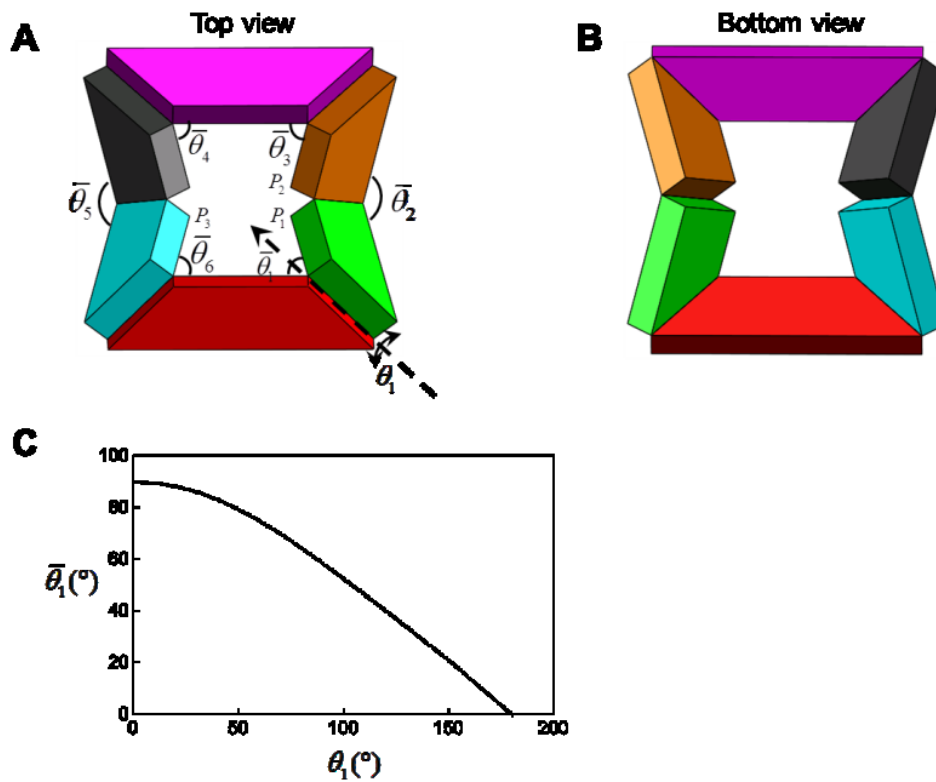


Figure 6.5: Projection kinematics analysis. (A) Top view of the waterbomb base. (B) Bottom view of the waterbomb base. (C) Relationship between the real joint angle θ_1 and projection joint angle $\bar{\theta}_1$.

6.3. Fabrication of the waterbomb base

The entire waterbomb base is constructed by folding a 8064 base version of the M13 ssDNA scaffold [20] using 197 ssDNA staples. The folding conditions and thermal annealing protocol are detailed in the following Experimental procedure section.

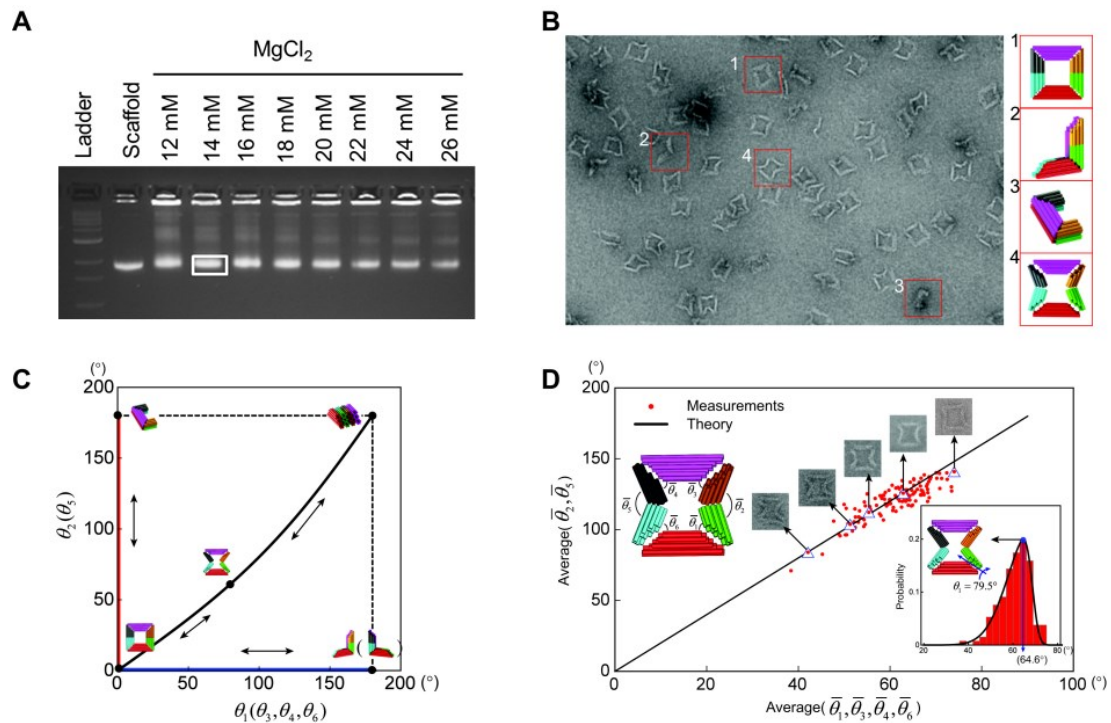


Figure 6.6: Experiment of waterbomb base. (A) Agarose gel electrophoresis purification image. (B) Transformation paths among the square, triangle, rectangle and compact configurations. (C) A transmission electron microscopy images and represents of folded configurations, scale bar: 100 nm. (D) Projection kinematics analysis (cite MMT paper) and equilibrium configuration. Black line is the theoretical relationship between projection angles $\bar{\theta}_1$ and $\bar{\theta}_2$, red dots are the measured projection information from TEM images and five typical TEM particles are shown. The distribution of the measured projection angle $\bar{\theta}_1$ is shown at the right bottom, and the equilibrium configuration is pointed out at the highest probability position.

The Gel purification image (Figure 6.6(A)) showed 14mM is the best magnesium concentration for the folding of waterbomb base. Figure 6.6(B) shows a TEM image snapshot of the experimental results. Most of the particles stay at an intermediate configuration where the six joints have some non-zero initial joint angles. A few structures exhibit the flat square configuration, and a few others exhibit a triangle or rectangle configuration. The most common set of configurations where the six joints have some random initial angles was termed an “intermediate” configuration, while a certain percentage of square, triangle and rectangle configurations can also be found.

When the waterbomb base is at the flat square configuration, the axes of the diagonal joints J1 and J4 are collinear and so are the diagonal joints J3 and J6. This square configuration facilitates the transformation into the triangular configuration by actuating the two collinear diagonal joints at the same time. Similarly, the structure transforms into the rectangular configuration by actuating the two waist joints (J2 and J5). In addition, the intermediate configuration can be folded into the compact one by closing all six joints simultaneously. Due to the compliance and clearance of the ssDNA connections at the joints and flexibility of dsDNA bundles, the entire structure is flexible and has noticeable variations in all configurations.

Since measuring the true kinematic parameters like joint angles in 3D space using TEM images is not possible, we applied the projection kinematics analysis (Figure 6.6(D)) [132] to estimate the configuration parameters based on projected parameters measured from 2D TEM images. We use $\bar{\theta}_1$, $\bar{\theta}_2$, $\bar{\theta}_3$, $\bar{\theta}_4$, $\bar{\theta}_5$ and $\bar{\theta}_6$ to denote the six projected joint angles from a chosen particle. From the projection angle distribution

(average value of $\bar{\theta}_1$, $\bar{\theta}_3$, $\bar{\theta}_4$ and $\bar{\theta}_6$), the equilibrium configuration was determined at $\bar{\theta}_1 = 64.5^\circ$, and the real joint angles $\theta_1 = 79.5^\circ$ and $\theta_2 = 79.5^\circ$ were obtained from the projection kinematics analysis (Figure 6.5). Previous research has shown that joints constructed by several short ssDNA segments had an equilibrium angle where the torque was zero if it was modeled as a torsional spring and the torque was fairly large when the joint was near the close and open positions [30].

6.4. Actuation of the waterbomb base

The waterbomb base is widely used as a structural unit for periodic assemblies with complex shape transformations such as a flat ribbon to a tube, or a tube to a sphere.

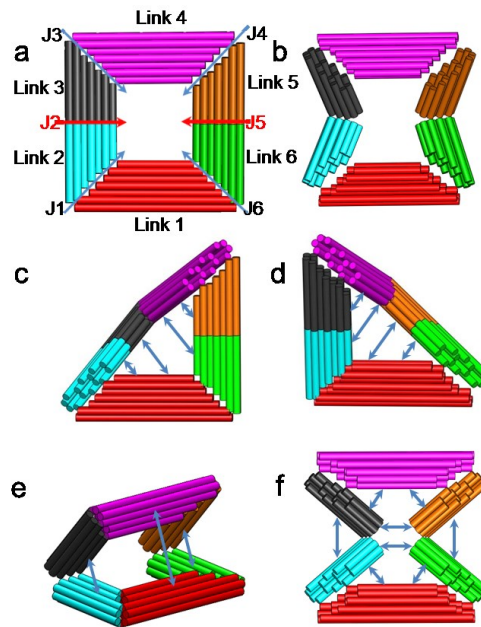


Figure 6.7: 3D cylindrical model of waterbomb base and its transformations.

The DNA waterbomb base is comprised of 6 flat panels connected by 6 foldable creases. Figure 6.7 illustrates the cylindrical model and its transformations.

6.4.1. Triangular configuration folding at room temperature

Each of the four diagonal joints J1, J3, J4 and J6 has five pairs of overhangs designed for actuation. In order to actuate into the folded triangular configuration, pairs of overhangs were designed, such as five pairs of overhangs on the surfaces of link2 and link 1 were used to assist the actuation of joint J1. A similar strategy was applied to the other three diagonal joints J3, J4 and J6. There are about 18 pairs of overhangs designed to trigger the folding of each triangle configuration, which should provide enough binding strength to stabilize the triangle. In addition, larger actuation torque introduced by these overhangs is levered by their further distance to diagonal joint axes. Also, more binding probability may be added for a successfully actuation.

Firstly, all 18 actuation staples for both right and left triangle configurations were added into waterbomb base sample purified by gel and kept incubated at room temperature overnight with the actuation staples at a 10-fold excess and magnesium ion concentration adjusted to 10 mM. Figure 6.8(top) shows the results of folding triangle configurations by adding the actuation staples directly. The actuation efficiency was determined by quantifying the ratio of the number of triangle configurations and total number of well-folded waterbomb bases on TEM images. Actuation efficiencies of both triangle configurations upon directly adding all of the actuation staples were in the range of 30-40%. The likely reason for the low efficiency is that a geometric obstacle is introduced when the waterbomb base is at an intermediate configurations, which is the

most common initial configuration. In the intermediate configurations, the axes of the diagonal joint pairs (J1 and J4) or (J3 and J6) are not collinear. This can also be detected and shown from the TEM images taken after directly actuation. Such as the circled particles shown on the right top TEM image, two diagonal joints J1, J4, but the particles still stay at the middle configuration because the clearances at joints introduced by four bases joint connections result in larger flexibility of the entire structure. In addition, adjuvant overhangs for the actuation of diagonal joints can't work due to geometric constraints. This is the case for both of the triangle configurations.

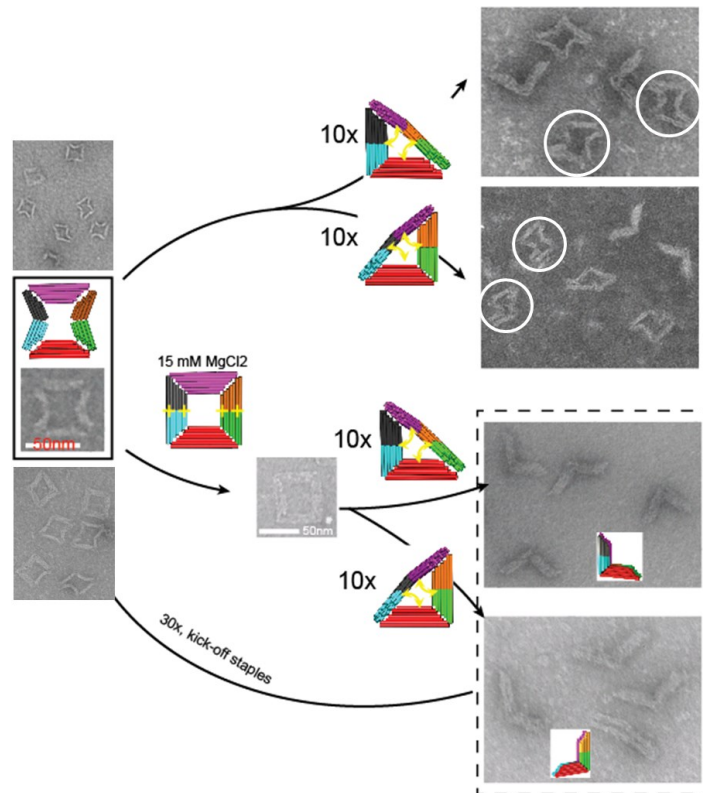


Figure 6.8: Triangle configurations actuation of waterbomb base.

In order to increase the triangle configuration actuation efficiency, a configuration folding control approach was developed. Intuitively, it is much easier to fold the waterbomb base from square configuration into the triangle configuration than start from the middle configuration where the entire structure has high probability folding to final compact configuration. In addition, flexibility of the joints results in uncertain configuration. In our waterbomb base design, two waist joints J2 and J5 can be locked by inducing base stacking at the ends of double helices adjacent to joint J2 on link 2 and link 3 or adjacent to joint J5 on link 5 and link 6. Only the two DOFs corresponding to the two triangle configurations will be left when two waist joints J2 and J5 are locked. Base stacking can be easily triggered by increasing the magnesium ion concentration as demonstrated in a recent study using base stacking interactions to reconfigure DNA origami devices [47,133].

To improve the triangle configuration actuation, we developed a multi-stage actuation approach. First, the magnesium concentration of gel purified waterbomb base samples was adjusted to 15 mM and kept at room temperature for a couple of hours to facilitate transformation into the flat configuration. Then, the actuation staples for the respective triangle configurations were added at 10-fold excess, and the mixture was incubated at room temperature overnight. TEM images at the bottom of Figure 6.8 show that most of waterbomb bases stay at triangle configuration, which means the DOFs elimination can dramatically increase the designated actuation efficiency. Also, torque introduced by the actuation staples works with the thermal fluctuation can overcome the energy barrier between the square and triangle configurations. We measured an actuation efficiency of

~80% was obtained for both of the triangle configuration actuations following this multi-stage actuation scheme.

On the other hand, in order to demonstrate that the triangle either configuration folding is reversible, a 30x excess of the removal staples that are fully complementary to the actuation staples were added to reopen all triangle-shape folded waterbomb bases. The mixtures were kept on a shaker table with 250 rpm rotation speed and 37 °C for two hours. TEM images show that most of triangle configuration particles were reopened (Figure 6.8, bottom left).

6.4.2. Rectangular configuration folding at room temperature

In addition to the two triangle configurations, the waterbomb base can also be folded into a rectangle configuration by actuating two waist joints J2 and J5. Similar to the triangle configuration actuation, six extra pairs of overhangs were designed on the surface of link 1 and link 4. Therefore, there are a total 16 pairs of overhangs for the actuation of rectangle configuration including five pairs of overhangs for each waist joints and the 6 pairs on link 1 and link 4.

First, all sixteen actuation staples corresponding to the sixteen pairs of overhangs were added to gel-purified waterbomb base structures directly. We tested ratios between the actuation staples and nanostructure of 10:1, 50:1 and 100:1 (the result of 10:1 actuation was shown in the top of Figure 6.9). The mixtures were kept at room temperature overnight. TEM images show ~30% of nanostructures achieved a rectangle configuration with the 100x actuation staples sample giving higher actuation efficiency relative to the other cases. In order to increase the actuation efficiency, the mixtures were put in a

shaker rotating at 250 rpm and 37 °C for 2 hours. It was found that 100-fold actuation staple over waterbomb base nanostructure have efficiency close to 40%. Even though thermal fluctuation can help the rectangle configuration folding, the efficiency is still less than half.

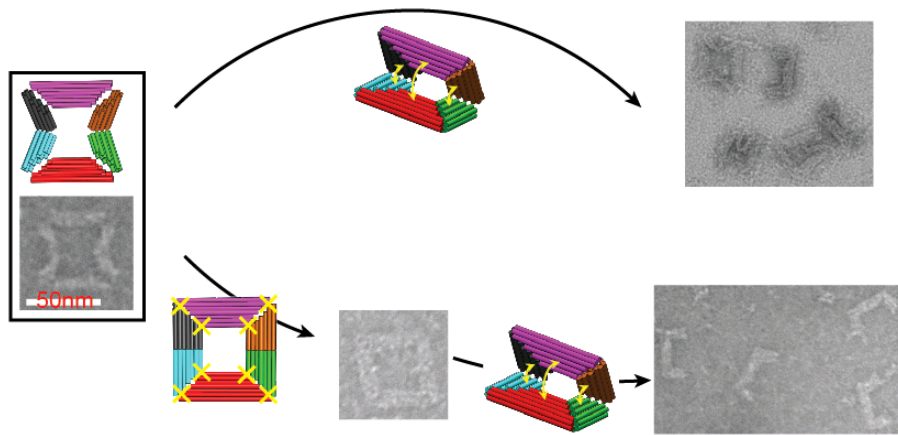


Figure 6.9: Rectangle configuration actuation of waterbomb base.

We tested a similar approach of suppressing other DOFs to improve the actuation of the rectangle configuration. In this case we locked all of four diagonal joints J1, J3, J4 and J6 into the angles corresponding to the flat square configuration leaving only the single DOF corresponding to the waist joint. Four locking staples that bind to the ssDNA strands left at each end of double helix are employed to constraint the rotation of the four diagonal joints. Specifically, each locking staple spans across the back side of the joint

binding to two adjacent ends of double helices on the mating surfaces. This binding constrains the rotation of the diagonal joint forcing it to stay near an angle corresponding to the flat configuration. In addition, lots of waterbomb base nanostructures stay at square configuration when four diagonal joints are locked without rotation angles, which ensure that the locked square waterbomb bases have the only DOF that is transfer to the rectangle configuration. Firstly, 10x actuation staples were added to waterbomb sample with the four diagonal joints locked and incubated on a shaker table rotating at 250 rpm at 37 °C for 2 hours. Quantified from TEM images, 54% waterbomb bases were folded into rectangle configuration quantified from TEM images (bottom of Figure 6.9). Actuation efficiency of rectangle configuration was not as high as the triangle configuration actuation. This is likely because the staple strands added to the diagonal joints were not as efficient in suppressing those degrees of freedom as the base-stacking approach used to suppress the waist joints for the triangle actuation.

6.4.3. Final compact configuration folding at room temperature

Folds of triangle and rectangle configurations of the waterbomb base were achieved with ~50-80% actuation efficiency. This suggests all six of the revolute joints on the nanostructure can effectively fold from 0° to 180°, which indicates the designated final compact configuration should also be achievable. In the macroscopic waterbomb base fold, the final compact configuration requires that the six joints are actuated at the same time and the rotation angles of the four diagonal joints and the two waist joints should be the same, respectively. Our approach used to actuate the joints of adding strands the bind across links does not provide precise control over the actuation timing and symmetry. It

is impossible to ensure the symmetry of rotation of four diagonal joints and two waist joints. Also, thermal fluctuations can introduce undesired transformation when the joints are actuated. Fortunately, the flexibility and clearance of the joints is enough to reduce the geometric constraints of the entire nanostructure so that joints can be actuated separately or individually. In order to stabilize the folding of final compact configuration, four pairs of overhangs were respectively designed on the mating surface of link 2 and link 6 and the mating surface of brown and black links. Including these staples that stabilize the final folded configuration, there are 38 actuation staples in total for folding of final compact configuration.

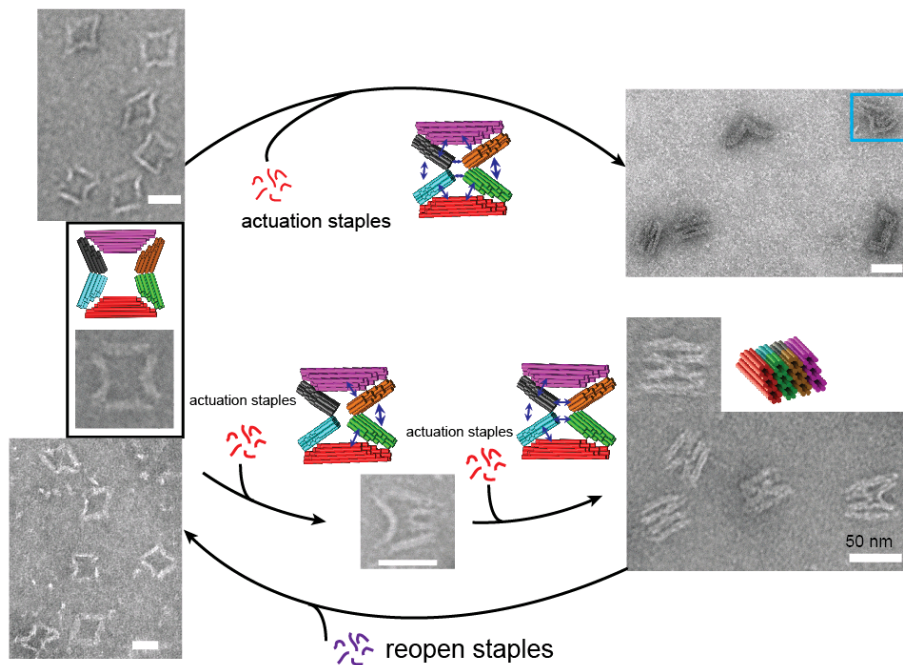


Figure 6.10: Final folded configuration actuation of waterbomb base.

We first tested the approach of adding all the actuation staples of final compact configuration to the gel purified waterbomb base sample all at once. The mixture was kept at room temperature overnight with the actuation staples at 10-fold excess with respect to the structure. Without suppressing any DOFs control, the entire nanostructure has three DOFs, which means many configurations including the triangle, rectangle and others can result from this direct actuation approach. The top right TEM image in Figure 6.10 show that a portion of waterbomb bases stay at triangle configuration, while others stay at rectangle configuration, also some of them actually folded into final compact configuration. Some twist and undesired configuration can also be found on the TEM such as the conformation highlighted in a blue square.

To improve the actuation of the fully compacted state, we pursued a similar approach of controlling individual DOFs control in multiple stages to the fold of final compact configuration. The folding was divided into two steps. First, two diagonal joints J1, J3 and one waist joint J2, all on one side of the waterbomb base were actuated. Since we already know that most of the particles exhibit an intermediate configuration where actuating all the joints along one side should force the waterbomb base towards the compacted state (here, J1 and J3 corresponding to two triangle configuration respectively and J2 corresponding to rectangle configuration). When only these three joints on one side of the structure were actuated, it is expected that most of particles will be at a configuration close to the designated final compact configuration with some flexibility due to the joint compliance, while some of them may already achieve the fully compacted

state. Theoretically, control of these three joints means the entire waterbomb base should have no remaining DOFs. However, the clearance and flexibility of the joints is large enough to enable a relatively small local mobility even when other joints are actuated. The TEM image in the middle bottom of Figure 6.10 showed that the flexibility of joints lower the geometric constraints on the entire structure and results in half of the joints being closed while the others still have some mobility due to the overall flexibility. In the following step, 10-fold actuation staples for the remaining three joints on the other side of the structure were added and the mixture was incubated at room temperature overnight again. With this multi-stage actuation approach, many particles were folded into the designated final compact configuration (bottom of Figure 6.10) yielding an actuation efficiency of 70%.

In addition, we demonstrated the reversability of folding by adding 30x releasing staples to the nanoparticles of fully compacted waterbomb base structures. The mixtures were kept in a shaking table rotating at 250 rpm and 37 °C for 2 hours. TEM images in the bottom of Figure 6.10 show that nearly all particles were released from the final compact configuration and stay at the initial middle configuration.

In general, transformation between initial, square and triangle configurations were achieved with high efficiencies based on the DOFs controlled actuation approach. Directly actuation of multiple DOFs nanostructure, such the waterbomb base shown here, usually obtained low yield and useless secondary results. It is valuable to first fix movable joints or links that are unnecessary for targeted shape transformation

6.5. Actuation of the waterbomb base by thermal annealing

The actuated shape transformations between different configurations are schematically represented in Figure 6.11(A). We tested the ability to perform all of the shape transformations of the waterbomb bases are conducted in a thermal cycler with a low temperature annealing ramp (detailed in following section 6.7) (Figure 6.11).

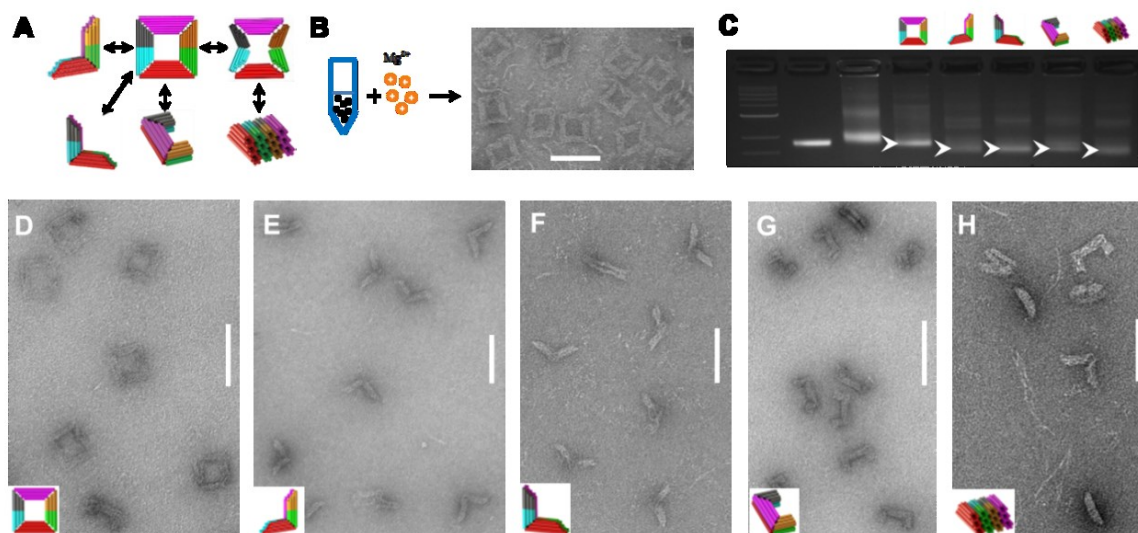


Figure 6.11: Folds of waterbomb base by thermal annealing control. (A) Folding of different configurations. (B) Obtain square configuration by increasing the magnesium concentration and a TEM image shows the result. (C) Gel purification image of the annealing controlled folding of square, triangular, rectangular and compact configuration. (D, E, F, G, H) TEM images of the folded square, triangle, rectangle and compact configurations. Scale bars: 100 nm.

The flat configuration can be obtained by flattening all or at least the four diagonal joints. Our experiment show that when the concentration of magnesium ion was

increased from 10 mM to 15 mM or even higher, such as 20 mM, most of the particles were transformed from the initial intermediate configuration to the square configuration due to base stacking interactions [47] (Figure 6.11(B)). On the other hand, square configuration is obtained by fixing the four diagonal joints via binding staples that connect the extra ssDNA segments at the ends of dsDNA bundles. Most of the waterbomb bases were actuated to the flat configuration via thermal annealing (Figure 6.11(D)).

The annealing approach of folding triangle configurations can also achieve a high yield (~80%)(Figure 6.11(E,F)). Similar to the folding of triangle configurations, rectangle configurations can also be achieved by the annealing actuation with a yield of about 80% (Figure 6.11(G)). Folding of the compact configuration by the anneal control fold with adding folding staples at once obtained similar results as the one conducted at room temperature (Figure 6.11(H)).

6.6. Higher-order DNA origami structures based on polymerization

A key reason for selecting the waterbomb base design was the possibility of making higher order assemblies that undergo drastic shape transitions. We designed DNA origami waterbomb base assemblies by the polymerization of the waterbomb bases via base-pairings of overhangs on specified surfaces. First, as the waterbomb bases were folded to the compact configuration, assembly between individual monomers occurred upon the adding of complementary binding strands that can connect the overhangs on lateral surfaces. Due to the gaps introduced by the connection of overhangs and

construction of joints, both linear and circular higher-order assemblies were observed (Figure 6.12(A)).

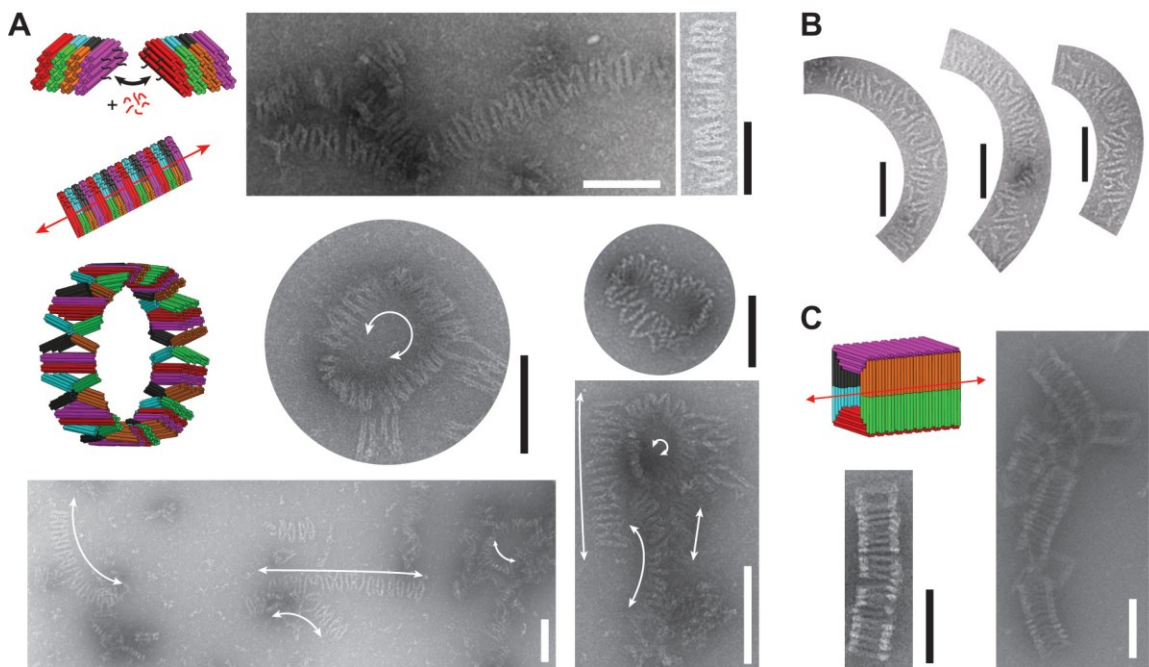


Figure 6.12: Higher-order nanostructures based on waterbomb base. (A) Polymerization based on the folded compact configuration along its lateral sides. Theoretically, straight filament can be obtained if no clearances exist and curved filament or even circular structure can be achieved if the clearances introduced by the design are taken into account, a circular structure has nine folded waterbomb bases is shown as an example. TEM images show the examples of linear, circular and curved structures obtained in the polymerization. (B) TEM images show the re-open example of the polymerized structures based on folded configuration. (C) Polymerization along the normal direction of lateral surface based on square configuration. Scale bars: 100 nm.

As seen from the experiment results, polymerization is achieved even though polymers ranged in size from 2 to 10 individual units, and structures with noticeable curvatures or

even closed circular loops of structures were observed. Then, the reopening strands of the compact configuration were added to release all folded waterbomb bases and more linear high-order structures show a large curvature due to the reduction of structural stiffness (Figure 6.12(B)). In addition, polymerization along the normal direction of the lateral side of the square configuration was achieved by adding the binding strands that connect the overhangs on the surfaces of individual monomers (Figure 6.12(C)).

6.7. Experimental procedure

The design was finished in caDNAno. Scaffold strand that has 8064 bases is clone the single-stranded M13MP18 bacteriophage viral genome and single-stranded staples were ordered from commercial vendors (Eurofins, Huntsville, AL and Integrated DNA Technologies, Inc., Coralville, IA).

Self-assembly: Scaffold strands were mixed at 20 nM with staples at 10-fold excess (each staple at 200 nM) in a buffer (containing 5 mM Tris, 5 mM NaCl, 1 mM EDTA), and a screening of MgCl₂ concentrations from 12, 14, 16, 18, 20, 22, 24, 26 mM was firstly conducted and found 14 mM was good enough for the future self-assembly. The self-assembly was finished during a thermal annealing ramp by increasing the temperature quickly to 65 °C and then slowly cooling down to 4 °C over a timescale of two and half days.

Gels were made with 2% agarose in 0.5× TBE buffer (44.5 mM Tris-borate, 1 mM EDTA) with 11 mM MgCl₂ and 1 μM ethidium bromide. Self-Assembled nanostructures were mixed with 6× loading dye (New England Biolabs, Ipswich, MA) and loaded to the well on the gel and run for approximately 3-4 hours at 70 V. Under UV table, bright

bands that contain nanostructures were excised and put into spin columns (Biorad, Hercules, CA) and then spin in a tabletop centrifuge at 10, 000 g for 10 min.

PEG purification: Mix self-assembled samples (≥ 100 μl) with the same volume 15% PEG8000 in a 1.5 ml tube, spin the mix in a tabletop centrifuge at 16, 000 g for 30 min, remove the liquid carefully and finally suspend the nanostructures in a $1\times$ TBE buffer with 14 mM MgCl_2 at a small volume. The concentration of nanostructure was measured by NanoDrop 1000.

Samples from gel purification can be directly used to prepare TEM grids and samples from PEG purification need to adjust the concentration to be smaller than 4nM before making TEM grids. For making a single grid, about 4 μl purified nanostructure sample was deposited on a plasma treated formvar coated TEM grid stabilized with evaporated carbon film (Electron Microscopy Sciences, Hatfield, PA) and incubated for four minutes. Then the sample was wicked away, and nanostructures were negatively stained by 2% Uranyl formate (SPI, West Chester, PA). The grid-side was firstly immersed into a small stain solution 10 μl droplet that was wicked off quickly and then quickly immersed into a 20 μl droplet and wicked off after incubating for 40 seconds. TEM grids need to dry for at least 30 minutes prior to imaging. Images were taken on a FEI Tecnai G2 Spirit TEM at an acceleration voltage of 80 kV.

Concentration of nanostructure in purified self-assembled sample was firstly measured by NanoDrop 1000. Then folding staples mixed with purified samples at big enough ratios (Table S) and the mixes were kept at room temperature overnight. For the two steps controlled folding, the mixes were kept at room temperature overnight first and the

adding the folding DNA strands and kept the final mixes at room temperature overnight. For the anneal controlled folding, folding DNA strands were added to the self-assembled samples at big enough excess ratios (Table S) and then increasing the temperature quickly to 37 °C and then slowly cooling down to 4 °C over a timescale of about 17 hours and final nanostructures were purified by agarose gel electrophoresis. Polymerizations were also a anneal controlled process by increasing the temperature quickly to 37 °C and then slowly cooling down to 4 °C over a timescale of about two days. Reopen of polymerizations high-order structures were conducted by two approaches: (I) after mixing the reopen strands with the samples, the mix was put in thermal cycler controlled by a anneal ramp which increasing the temperature quickly to 30 °C and then slowly cooling down to 4 °C over a timescale of about 15 hours and (II) keeping the mix at 37 °C for about 2 hours.

6.8. Summary and conclusion

The waterbomb base fabricated by DNA origami here demonstrates for the first time that the design principle of the paper folding art origami can be applied to design DNA nanostructures with multiple controllable configurations via molecular self-assembling. The realization of patterning multiple dynamic waterbomb base nanostructures shows the feasibility of polymerizing high-order origami structures. This novel design approach paves the road to self-assemble reconfigurable materials and systems whose mechanical properties can be programed and tuned via transforming individual monomers [134–136] among several pre-designed configurations.

Chapter 7: Conclusions and Future Work

7.1. Conclusions

The dissertation presents the achievements of research about compliant and rigid-body DNA origami mechanisms, including PRB models application on CDOM, design and fabrication of compliant hinge and four-bar bistable mechanism, projection kinematics analysis of DOM and demonstration of origami of DNA origami nanostructures by the design of a waterbomb base.

Chapter 2 present the PRB models used in compliant mechanism design and analysis. Classic PRB model works well for cantilever beam with uniform cross section cantilever beam. However, in the design of compliant DNA origami mechanisms, all joints or junctions are not perfect as designed. For example, one end of the cantilever beam usually should be fixed on the frame link or ground, but this fixed junction in DNA origami nanostructures can't obtain infinite large stiffness. This can vary parameters used in the classic PRB model, including the characteristic radius factor and stiffness coefficient. In order to overcome this issue, another torsional spring was used to model the junction in the DNA origami nanostructures and the relationship between stiffness of the junction and the parameters used in PRB model were explored. In addition, it is very

common that the beam has several different segments in the DNA origami nanostructures design. Modified PRB models were presented for analysis of three segment beam design. These modified PRB models can provide precise expectations of deformation and stored energy of beam designed by DNA origami.

Chapter 3 showed a compliant hinge designed and fabricated by scaffolded DNA origami. If an external bending load applied on the two ends, the compliant joint can be easily deformed due to the small stiffness of the middle thinner segment. Most of the deformation happened on the compliant segment and most of the strain energy are stored in it. In order to test the deformation ability of the compliant joint, ssDNA strands springs were placed between the two sides at the bottom layer and then the bending angle can be controlled by shifting the length of the ssDNA strands from the loops placed on the side of the rigid segment. The experiment results proved that the strategy of design compliant hinge by DNA origami is feasible and successful. This example also demonstrated that it is a feasible to tune the stiffness of the complaint nanostructures by tuning the geometry parameters. In addition, beam model and PRB model were used to quantify the deformations and stored energies and the models can capture the experiment results very well.

Chapter 4 introduced the design and fabrication of the four-bar bistable linkage by scaffolded DNA origami. There are two positions where there is no deformation on the compliant link. These two stable positions can be easily figured out on the energy curve of the entire bistable mechanism because both of them correspond to the two energy minima points. Experiment results demonstrate that without control, lots of particles stay

at the two stable configurations, close or open, while some particles got stuck at the unstable configuration due to the base-stacking on the joint between the crank and coupler links. In addition, PRB models developed in Chapter 2 were used to quantify the switch behavior between the two stable configurations and its results were close to experiment. This four-bar bistable mechanism brings us great confidence to apply the design methodology of compliant mechanism on the design of DNA origami mechanisms and machines.

Chapter 5 established the conception of projection kinematics analysis and applied it to verify the DNA origami mechanisms based on the 2D TEM images. Started from analysis of projection configuration of basic kinematic joints, including revolute, prismatic, cylindrical and spherical joints, real configuration in space can be obtained by geometrical information of projection configuration, such as link length and the angle between links. Then, four-bar and five-bar mechanisms were chosen as theoretical examples to demonstrate the feasibility of projection kinematics analysis. At last, real configuration of universal joint and Bennett linkage in space were figured out by projection information measured from 2D TEM images. Projection kinematics provides systematical analysis and verification of 3D configurations of DNA origami mechanisms based on their projection configurations.

Chapter 6 demonstrated the origami of DNA origami nanostructures by the design and folding of a waterbomb base. This waterbomb base can lead to four foldable configurations, including square, triangles, rectangle and folded compact shape. The control of the six hinge angles can be achieved by the binding and releasing of over-

hangs. All of the folding configurations can be either achieved at room temperature or by in a thermocycler with annealing control. In addition, higher-order DNA origami nanostructures were obtained by the polymerizations of folded waterbomb base with different configurations. This not only proved that much more complex dynamic DNA origami mechanisms can be fabricated, but also higher-order dynamic nanostructures can be obtained based on the pattern of single nanostructures.

7.2. Future work

With these advances, complex nanostructures and nanomachines can be designed and fabricated by scaffolded DNA origami nanotechnology. In the future, significant challenges must be addressed in order to realize the functional potential of DNA origami nanomachines.

First, general design and fabrication protocol of higher-order dynamic DNA origami nanostructures should be achieved. Right now, the size of DNA origami nanostructure is determined by the length of the scaffold (typically ~7000-8000 nucleotides). As the larger the DNA origami structure is, the lower the yield will be. One strategy is to assemble individual parts one by one, such as the assembly of a table, when the top surface plate is fixed, the four legs can be assembled to it one after another. This method can ensure that all of the parts are assembled, but it always costs lots of time and needs many operations especially when the number of parts is large. Another big issue of this kind of assembly is the assembly interference can be easily caused due to the geometry complexity. It is very often that the former assembled part may obstacle the assembly of the later one or increases the assemble difficulty of the later one.

Second, much more efficient actuation method should be developed. Right now, DNA strand displacement is the most popular approach, which depends on the number and length of overhangs placed on the surfaces of DNA origami structures. The efficiency of this method is a little bit slow and can be dramatically influenced by the ion concentration and temperatures. Also, it is not good to do multiple steps actuations because in each step, new DNA strands need to be added, which will dilute the concentration of the nanostructure. Another issue is extra binding and releasing DNA strands may influence the behavior of dynamic DNA nanostructures.

Third, comparing with computer-aided design tools used in traditional machine design, currently, the design process of DNA origami nanostructures is ad hoc and tedious, design automation is necessary for design optimization. Usually, DNA origami design started from the 2D sheet in caDNAno which is the most popular design tools. In the engineering design, 3D model should be finished first and then 2D design of the scaffold routing and staples can be finished on the 3D geometrical. This can provide good visualization for designers and also make the detection and correction of errors easily.

Moreover, much more efficient and accurate computational models and tools should be developed. As the DNA nanostructure become more and more complex, computational tools should have the ability to provide accurate enough results to quantify the performance with acceptable cost. Right now, computational tools developed based on finite element method and coarse-grain model of DNA can't capture the performance of very flexible elements in DNA nanostructures, such as short ssDNA connections. As molecular dynamic simulation always costs lots of time and computation source, it is not

economic for engineering design of DNA origami. In addition, the computational tool should combine with the design automation to speed the design and analysis process of DNA nanostructures and provide accurate expectations before experiment.

Finally, much more applications, such as targeted drug delivery, drug releasing control and biosensors et al., can be explored. These researches will bring novel techniques for diagnosis, monitoring and therapy of diseases including cancers.

References

- [1] Lund, K., Manzo, A. J., Dabby, N., Michelotti, N., Johnson-Buck, A., Nangreave, J., Taylor, S., Pei, R., Stojanovic, M. N., Walter, N. G., and others, 2010, “Molecular Robots Guided by Prescriptive Landscapes,” *Nature*, **465**(7295), pp. 206–210.
- [2] Mavroidis, C., and Ferreira, A., 2013, “Nanorobotics,” Springer, pp. 3–27.
- [3] McCarthy, J. M., 2006, *Geometric Design of Linkages*, Springer Science & Business Media.
- [4] Chirikjian, G. S., Kazerounian, K., and Mavroidis, C., 2005, “Analysis and Design of Protein Based Nanodevices: Challenges and Opportunities in Mechanical Design,” *J. Mech. Des.*, **127**(4), pp. 695–698.
- [5] Hamdi, M., and Ferreira, A., 2008, “DNA Nanorobotics,” *Microelectron. J.*, **39**(8), pp. 1051–1059.
- [6] Sułkowska, J. I., Noel, J. K., and Onuchic, J. N., 2012, “Energy Landscape of Knotted Protein Folding,” *Proc. Natl. Acad. Sci.*, **109**(44), pp. 17783–17788.
- [7] Yin, P., Yan, H., Daniell, X. G., Turberfield, A. J., and Reif, J. H., 2004, “A Unidirectional DNA Walker That Moves Autonomously along a Track,” *Angew. Chem. Int. Ed.*, **43**(37), pp. 4906–4911.
- [8] Sherman, W. B., and Seeman, N. C., 2004, “A Precisely Controlled DNA Biped Walking Device,” *Nano Lett.*, **4**(7), pp. 1203–1207.
- [9] Yin, P., Choi, H. M. T., Calvert, C. R., and Pierce, N. A., 2008, “Programming Biomolecular Self-Assembly Pathways,” *Nature*, **451**(7176), pp. 318–322.
- [10] Watson, J. D., and Crick, F. H., 1953, *The Structure of DNA*.
- [11] Dill, K. A., Ozkan, S. B., Shell, M. S., and Weikl, T. R., 2008, “The Protein Folding Problem,” *Annu. Rev. Biophys.*, **37**, p. 289.

- [12] Seeman, N. C., 1982, “Nucleic Acid Junctions and Lattices,” *J. Theor. Biol.*, **99**(2), pp. 237–247.
- [13] Seeman, N. C., 2003, “DNA in a Material World,” *Nature*, **421**(6921), pp. 427–431.
- [14] Niemeyer, C. M., and Adler, M., 2002, “Nanomechanical Devices Based on DNA,” *Angew. Chem. Int. Ed.*, **41**(20), pp. 3779–3783.
- [15] Seeman, N. C., 2005, “From Genes to Machines: DNA Nanomechanical Devices,” *Trends Biochem. Sci.*, **30**(3), pp. 119–125.
- [16] Zhang, D. Y., and Winfree, E., 2009, “Control of DNA Strand Displacement Kinetics Using Toehold Exchange,” *J. Am. Chem. Soc.*, **131**(47), pp. 17303–17314.
- [17] Srinivas, N., Ouldridge, T. E., Šulc, P., Schaeffer, J. M., Yurke, B., Louis, A. A., Doye, J. P., and Winfree, E., 2013, “On the Biophysics and Kinetics of Toehold-Mediated DNA Strand Displacement,” *Nucleic Acids Res.*, **41**(22), pp. 10641–10658.
- [18] Yurke, B., Turberfield, A. J., Mills, A. P., Simmel, F. C., and Neumann, J. L., 2000, “A DNA-Fuelled Molecular Machine Made of DNA,” *Nature*, **406**(6796), pp. 605–608.
- [19] Rothmund, P. W. K., 2006, “Folding DNA to Create Nanoscale Shapes and Patterns,” *Nature*, **440**(7082), pp. 297–302.
- [20] Douglas, S. M., Dietz, H., Liedl, T., Högberg, B., Graf, F., and Shih, W. M., 2009, “Self-Assembly of DNA into Nanoscale Three-Dimensional Shapes,” *Nature*, **459**(7245), pp. 414–418.
- [21] Dietz, H., Douglas, S. M., and Shih, W. M., 2009, “Folding DNA into Twisted and Curved Nanoscale Shapes,” *Science*, **325**(5941), pp. 725–730.
- [22] Castro, C. E., Kilchherr, F., Kim, D.-N., Shiao, E. L., Wauer, T., Wortmann, P., Bathe, M., and Dietz, H., 2011, “A Primer to Scaffolded DNA Origami,” *Nat. Methods*, **8**(3), pp. 221–229.
- [23] Ke, Y., Sharma, J., Liu, M., Jahn, K., Liu, Y., and Yan, H., 2009, “Scaffolded DNA Origami of a DNA Tetrahedron Molecular Container,” *Nano Lett.*, **9**(6), pp. 2445–2447.
- [24] Andersen, E. S., Dong, M., Nielsen, M. M., Jahn, K., Subramani, R., Mamdouh, W., Golas, M. M., Sander, B., Stark, H., Oliveira, C. L. P., Pedersen, J. S., Birkedal, V., Besenbacher, F., Gothelf, K. V., and Kjems, J., 2009, “Self-

- Assembly of a Nanoscale DNA Box with a Controllable Lid,” *Nature*, **459**(7243), pp. 73–76.
- [25] Liedl, T., Högberg, B., Tytell, J., Ingber, D. E., and Shih, W. M., 2010, “Self-Assembly of Three-Dimensional Prestressed Tensegrity Structures from DNA,” *Nat. Nanotechnol.*, **5**(7), pp. 520–524.
- [26] Han, D., Pal, S., Nangreave, J., Deng, Z., Liu, Y., and Yan, H., 2011, “DNA Origami with Complex Curvatures in Three-Dimensional Space,” *Science*, **332**(6027), pp. 342–346.
- [27] Inuma, R., Ke, Y., Jungmann, R., Schlichthaerle, T., Woehrstein, J. B., and Yin, P., 2014, “Polyhedra Self-Assembled from DNA Tripods and Characterized with 3D DNA-PAINT,” *Science*, **344**(6179), pp. 65–69.
- [28] Wei, R., Martin, T. G., Rant, U., and Dietz, H., 2012, “DNA Origami Gatekeepers for Solid-State Nanopores,” *Angew. Chem.*, **124**(20), pp. 4948–4951.
- [29] Hernandez-Ainsa, S., Bell, N. A. W., Thacker, V. V., Gopfrich, K., Misiunas, K., Fuentes-Perez, M. E., Moreno-Herrero, F., and Keyser, U. F., 2013, “DNA Origami Nanopores for Controlling DNA Translocation,” *Acs Nano*, **7**(7), pp. 6024–6030.
- [30] Marras, A. E., Zhou, L., Su, H.-J., and Castro, C. E., 2015, “Programmable Motion of DNA Origami Mechanisms,” *Proc. Natl. Acad. Sci.*, p. 201408869.
- [31] E. Castro, C., Su, H.-J., E. Marras, A., Zhou, L., and Johnson, J., 2015, “Mechanical Design of DNA Nanostructures,” *Nanoscale*, **7**(14), pp. 5913–5921.
- [32] Howell, L. L., 2001, *Compliant Mechanisms*, Wiley-Interscience.
- [33] Howell, L. L., and Midha, A., 1995, “Parametric Deflection Approximations for End-Loaded, Large-Deflection Beams in Compliant Mechanisms,” *J. Mech. Des.*, **117**(1), pp. 156–165.
- [34] Howell, L. L., Midha, A., and Norton, T. W., 1996, “Evaluation of Equivalent Spring Stiffness for Use in a Pseudo-Rigid-Body Model of Large-Deflection Compliant Mechanisms,” *J. Mech. Des.*, **118**(1), pp. 126–131.
- [35] Howell, L. L., DiBiasio, C. M., Cullinan, M. A., Panas, R. M., and Culpepper, M. L., 2010, “A Pseudo-Rigid-Body Model for Large Deflections of Fixed-Clamped Carbon Nanotubes,” *J. Mech. Robot.*, **2**(3), pp. 034501-034501-5.
- [36] Shi, H., Su, H.-J., Dagalak, N., and Kramar, J. A., 2013, “Kinematic Modeling and Calibration of a Flexure Based Hexapod Nanopositioner,” *Precis. Eng.*, **37**(1), pp. 117–128.

- [37] Grima, J. N., Gatt, R., Farrugaia, P.-S., Alderson, A., and Evans, K. E., 2005, "Auxetic Cellular Materials and Structures," pp. 489–495.
- [38] Yoo, J., and Aksimentiev, A., 2013, "In Situ Structure and Dynamics of DNA Origami Determined through Molecular Dynamics Simulations," *Proc. Natl. Acad. Sci. U. S. A.*, **110**(50), pp. 20099–20104.
- [39] Zhou, L., Marras, A. E., Su, H.-J., and Castro, C. E., 2014, "DNA Origami Compliant Nanostructures with Tunable Mechanical Properties," *ACS Nano*, **8**(1), pp. 27–34.
- [40] Zhou, L., Marras, A. E., Su, H.-J., and Castro, C. E., 2015, "Direct Design of an Energy Landscape with Bistable DNA Origami Mechanisms," *Nano Lett.*, **15**(3), pp. 1815–1821.
- [41] Zhou, L., Marras, A. E., Castro, C. E., and Su, H.-J., 2016, "Pseudorigid-Body Models of Compliant DNA Origami Mechanisms," *J. Mech. Robot.*, **8**(5), pp. 051013-051013-11.
- [42] Kim, D.-N., Kilchherr, F., Dietz, H., and Bathe, M., 2012, "Quantitative Prediction of 3D Solution Shape and Flexibility of Nucleic Acid Nanostructures," *Nucleic Acids Res.*, **40**(7), pp. 2862–2868.
- [43] Doye, J. P. K., Ouldridge, T. E., Louis, A. A., Romano, F., Sulc, P., Matek, C., Snodin, B. E. K., Rovigatti, L., Schreck, J. S., Harrison, R. M., and Smith, W. P. J., 2013, "Coarse-Graining DNA for Simulations of DNA Nanotechnology," *Phys. Chem. Chem. Phys.*, **15**(47), p. 20395.
- [44] Kauert, D. J., Kurth, T., Liedl, T., and Seidel, R., 2011, "Direct Mechanical Measurements Reveal the Material Properties of Three-Dimensional DNA Origami," *Nano Lett.*, **11**(12), pp. 5558–5563.
- [45] Douglas, S. M., Bachelet, I., and Church, G. M., 2012, "A Logic-Gated Nanorobot for Targeted Transport of Molecular Payloads," *Science*, **335**(6070), pp. 831–834.
- [46] Kuzuya, A., and Komiyama, M., 2009, "Design and Construction of a Box-Shaped 3D-DNA Origami," *Chem. Commun.*, (28), p. 4182.
- [47] Gerling, T., Wagenbauer, K. F., Neuner, A. M., and Dietz, H., 2015, "Dynamic DNA Devices and Assemblies Formed by Shape-Complementary, Non-base Pairing 3D Components," *Science*, **347**(6229), pp. 1446–1452.
- [48] Marras, A. E., Zhou, L., Su, H.-J., and Castro, C. E., 2015, "Programmable Motion of DNA Origami Mechanisms," *Proc. Natl. Acad. Sci.*, **112**(3), pp. 713–718.

- [49] Castro, C. E., Su, H.-J., Marras, A. E., Zhou, L., and Johnson, J., 2015, “Mechanical Design of DNA Nanostructures,” *Nanoscale*, **7**(14), pp. 5913–5921.
- [50] Midha, A., and Howell, L. L., 1994, “A Method for the Design of Compliant Mechanisms With Small-Length Flexural Pivots,” *J. Mech. Des.*, **116**(1).
- [51] Su, H.-J., 2009, “A Pseudorigid-Body 3R Model for Determining Large Deflection of Cantilever Beams Subject to Tip Loads,” *J. Mech. Robot.*, **1**(2), p. 021008.
- [52] Marko, J. F., and Siggia, E. D., 1995, “Stretching DNA,” *Macromolecules*, **28**(26), pp. 8759–8770.
- [53] Tinland, B., Pluen, A., Sturm, J., and Weill, G., 1997, “Persistence Length of Single-Stranded DNA,” *Macromolecules*, **30**(19), pp. 5763–5765.
- [54] Boal, D., and Boal, D. H., 2012, *Mechanics of the Cell*, Cambridge University Press.
- [55] Douglas, S. M., Marblestone, A. H., Teerapittayanon, S., Vazquez, A., Church, G. M., and Shih, W. M., 2009, “Rapid Prototyping of 3D DNA-Origami Shapes with caDNAno,” *Nucleic Acids Res.*, **37**(15), pp. 5001–5006.
- [56] Wolfe, K. C., Hastings, W. A., Dutta, S., Long, A., Shapiro, B. A., Woolf, T. B., Guthold, M., and Chirikjian, G. S., 2012, “Multiscale Modeling of Double-Helical DNA and RNA: A Unification through Lie Groups,” *J. Phys. Chem. B*, **116**(29), pp. 8556–8572.
- [57] Yamakawa, H., 1997, *Helical Wormlike Chains in Polymer Solutions*, Springer Berlin.
- [58] Odijk, T., 1995, “Stiff Chains and Filaments under Tension,” *Macromolecules*, **28**(20), pp. 7016–7018.
- [59] Fu, J., and Yan, H., 2012, “Controlled Drug Release by a Nanorobot,” *Nat. Biotechnol.*, **30**(5), pp. 407–408.
- [60] Elbaz, J., and Willner, I., 2012, “DNA Origami: Nanorobots Grab Cellular Control,” *Nat. Mater.*, **11**(4), pp. 276–277.
- [61] Bath, J., and Turberfield, A. J., 2007, “DNA Nanomachines,” *Nat. Nanotechnol.*, **2**(5), pp. 275–284.
- [62] Cohen, A. E., and Moerner, W. E., 2007, “Principal-Components Analysis of Shape Fluctuations of Single DNA Molecules,” *Proc. Natl. Acad. Sci.*, **104**(31), pp. 12622–12627.

- [63] Culpepper, M. L., DiBiasio, C. M., Panas, R. M., Magleby, S., and Howell, L. L., 2006, "Simulation of a Carbon Nanotube-Based Compliant Parallel-Guiding Mechanism: A Nanomechanical Building Block," *Appl. Phys. Lett.*, **89**(20), pp. 203111–203111.
- [64] Magleby, S. P., Culpepper, M. L., Howell, L. L., Panas, R., and DiBiasio, C. M., 2008, "Comparison of Molecular Simulation and Pseudo-Rigid-Body Model Predictions for a Carbon Nanotube-Based Compliant Parallel-Guiding Mechanism," *J. Mech. Des.*, **130**(4).
- [65] Reckmann, B., Grosse, F., Urbanke, C., Frank, R., Blöcker, H., and Krauss, G., 1985, "Analysis of Secondary Structures in M13mp8 (+) Single-Stranded DNA by the Pausing of DNA Polymerase α ," *Eur. J. Biochem.*, **152**(3), pp. 633–643.
- [66] Dong, F., Allawi, H. T., Anderson, T., Neri, B. P., and Lyamichev, V. I., 2001, "Secondary Structure Prediction and Structure-Specific Sequence Analysis of Single-Stranded DNA," *Nucleic Acids Res.*, **29**(15), pp. 3248–3257.
- [67] Protozanova, E., Yakovchuk, P., and Frank-Kamenetskii, M. D., 2004, "Stacked–Unstacked Equilibrium at the Nick Site of DNA," *J. Mol. Biol.*, **342**(3), pp. 775–785.
- [68] Blanchoin, L., Amann, K. J., Higgs, H. N., Marchand, J.-B., Kaiser, D. A., and Pollard, T. D., 2000, "Direct Observation of Dendritic Actin Filament Networks Nucleated by Arp2/3 Complex and WASP/Scar Proteins," *Nature*, **404**(6781), pp. 1007–1011.
- [69] Hartemink, C. A., 2005, "The Cross-Linking Mechanism of Filamin A in the Actin Cytoskeleton," Thesis, Massachusetts Institute of Technology.
- [70] Endo, M., Yang, Y., and Sugiyama, H., 2013, "DNA Origami Technology for Biomaterials Applications," *Biomater. Sci.*
- [71] Liu, W., Zhong, H., Wang, R., and Seeman, N. C., 2011, "Crystalline Two-Dimensional DNA-Origami Arrays," *Angew. Chem. Int. Ed.*, **50**(1), pp. 264–267.
- [72] Lieleg, O., Claessens, M. M., and Bausch, A. R., 2010, "Structure and Dynamics of Cross-Linked Actin Networks," *Soft Matter*, **6**(2), pp. 218–225.
- [73] Smith, S. B., Cui, Y., and Bustamante, C., 1996, "Overstretching B-DNA: The Elastic Response of Individual Double-Stranded and Single-Stranded DNA Molecules," *Science*, **271**(5250), pp. 795–799.

- [74] Crozier, P. S., and Stevens, M. J., 2003, "Simulations of Single Grafted Polyelectrolyte Chains: ssDNA and dsDNA," *J. Chem. Phys.*, **118**(8), pp. 3855–3860.
- [75] Chi, Q., Wang, G., and Jiang, J., 2013, "The Persistence Length and Length per Base of Single-Stranded DNA Obtained from Fluorescence Correlation Spectroscopy Measurements Using Mean Field Theory," *Phys. Stat. Mech. Its Appl.*, **392**(5), pp. 1072–1079.
- [76] Murphy, M. C., Rasnik, I., Cheng, W., Lohman, T. M., and Ha, T., 2004, "Probing Single-Stranded DNA Conformational Flexibility Using Fluorescence Spectroscopy," *Biophys. J.*, **86**(4), pp. 2530–2537.
- [77] Mandelkern, M., Elias, J. G., Eden, D., and Crothers, D. M., 1981, "The Dimensions of DNA in Solution," *J. Mol. Biol.*, **152**(1), pp. 153–161.
- [78] Baumann, C. G., Smith, S. B., Bloomfield, V. A., and Bustamante, C., 1997, "Ionic Effects on the Elasticity of Single DNA Molecules," *Proc. Natl. Acad. Sci.*, **94**(12), pp. 6185–6190.
- [79] Bustamante, C., Smith, S. B., Liphardt, J., and Smith, D., 2000, "Single-Molecule Studies of DNA Mechanics," *Curr. Opin. Struct. Biol.*, **10**(3), pp. 279–285.
- [80] Manning, G. S., 2006, "The Persistence Length of DNA Is Reached from the Persistence Length of Its Null Isomer through an Internal Electrostatic Stretching Force," *Biophys. J.*, **91**(10), pp. 3607–3616.
- [81] Krishnan, Y., and Bathe, M., 2012, "Designer Nucleic Acids to Probe and Program the Cell," *Trends Cell Biol.*, **22**(12), pp. 624–633.
- [82] Linko, V., and Dietz, H., 2013, "The Enabled State of DNA Nanotechnology," *Curr. Opin. Biotechnol.*, **24**(4), pp. 555–561.
- [83] Saccà, B., Meyer, R., Erkelenz, M., Kiko, K., Arndt, A., Schroeder, H., Rabe, K. S., and Niemeyer, C. M., 2010, "Orthogonal Protein Decoration of DNA Origami," *Angew. Chem. Int. Ed.*, **49**(49), pp. 9378–9383.
- [84] Han, D., Pal, S., Yang, Y., Jiang, S., Nangreave, J., Liu, Y., and Yan, H., 2013, "DNA Gridiron Nanostructures Based on Four-Arm Junctions," *Science*, **339**(6126), pp. 1412–1415.
- [85] Ding, B., and Seeman, N. C., 2006, "Operation of a DNA Robot Arm Inserted into a 2D DNA Crystalline Substrate," *Science*, **314**(5805), pp. 1583–1585.
- [86] Gu, H., Chao, J., Xiao, S.-J., and Seeman, N. C., 2010, "A Proximity-Based Programmable DNA Nanoscale Assembly Line," *Nature*, **465**(7295), pp. 202–205.

- [87] Hung, A. M., Micheel, C. M., Bozano, L. D., Osterbur, L. W., Wallraff, G. M., and Cha, J. N., 2010, "Large-Area Spatially Ordered Arrays of Gold Nanoparticles Directed by Lithographically Confined DNA Origami," *Nat. Nanotechnol.*, **5**(2), pp. 121–126.
- [88] Schreiber, R., Kempter, S., Holler, S., Schüller, V., Schiffels, D., Simmel, S. S., Nickels, P. C., and Liedl, T., 2011, "DNA Origami-Templated Growth of Arbitrarily Shaped Metal Nanoparticles," *Small*, **7**(13), pp. 1795–1799.
- [89] Zadegan, R. M., Jepsen, M. D. E., Thomsen, K. E., Okholm, A. H., Schaffert, D. H., Andersen, E. S., Birkedal, V., and Kjems, J., 2012, "Construction of a 4 Zeptoliters Switchable 3D DNA Box Origami," *ACS Nano*, **6**(11), pp. 10050–10053.
- [90] Bell, N. A. W., Engst, C. R., Ablay, M., Divitini, G., Ducati, C., Liedl, T., and Keyser, U. F., 2012, "DNA Origami Nanopores," *Nano Lett.*, **12**(1), pp. 512–517.
- [91] List, J., Simmel, F. C., Dietz, H., Mayer, M., Langecker, M., Renner, S., Arnaut, V., and Martin, T. G., 2012, "Synthetic Lipid Membrane Channels Formed by Designed DNA Nanostructures," *Science*, **338**(6109), pp. 932–936.
- [92] Kuzuya, A., Sakai, Y., Yamazaki, T., Xu, Y., and Komiyama, M., 2011, "Nanomechanical DNA Origami 'Single-Molecule Beacons' Directly Imaged by Atomic Force Microscopy," *Nat. Commun.*, **2**, p. 449.
- [93] Tintoré, M., Gállego, I., Manning, B., Eritja, R., and Fàbrega, C., 2013, "DNA Origami as a DNA Repair Nanosensor at the Single-Molecule Level," *Angew. Chem. Int. Ed.*, **52**(30), pp. 7747–7750.
- [94] Yan, H., Zhang, X., Shen, Z., and Seeman, N. C., 2002, "A Robust DNA Mechanical Device Controlled by Hybridization Topology," *Nature*, **415**(6867), pp. 62–65.
- [95] Yin, P., Turberfield, A. J., Sahu, S., and Reif, J. H., 2005, "DNA Computing," Springer, pp. 426–444.
- [96] Shen, W., Bruist, M., Goodman, S., and Seeman, N. C., 2004, "A Nanomechanical Device for Measuring the Excess Binding Energy of Proteins That Distort DNA," *Angew Chem Int Ed*, **43**, pp. 4750–4752.
- [97] Pan, K., Kim, D.-N., Zhang, F., Adendorff, M. R., Yan, H., and Bathe, M., 2014, "Lattice-Free Prediction of Three-Dimensional Structure of Programmed DNA Assemblies," *Nat. Commun.*, **5**.

- [98] Plesa, C., Ananth, A. N., Linko, V., Gülcher, C., Katan, A. J., Dietz, H., and Dekker, C., 2013, “Ionic Permeability and Mechanical Properties of DNA Origami Nanoplates on Solid-State Nanopores,” *ACS Nano*, **8**(1), pp. 35–43.
- [99] Masters, N. D., and Howell, L. L., 2003, “A Self-Retracting Fully Compliant Bistable Micromechanism,” *J. Microelectromechanical Syst.*, **12**(3), pp. 273–280.
- [100] Lusk, C. P., and Howell, L. L., 2008, “Spherical Bistable Micromechanism,” *J. Mech. Des.*, **130**(4), p. 045001.
- [101] Schiffels, D., Liedl, T., and Fygenson, D. K., 2013, “Nanoscale Structure and Microscale Stiffness of DNA Nanotubes,” *ACS Nano*, **7**(8), pp. 6700–6710.
- [102] Joanicot, M., and Revet, B., 1987, “DNA Conformational Studies from Electron Microscopy. I. Excluded Volume Effect and Structure Dimensionality,” *Biopolymers*, **26**(2), pp. 315–326.
- [103] Frontali, C., 1988, “Excluded-Volume Effect on the Bidimensional Conformation of DNA Molecules Adsorbed to Protein Films,” *Biopolymers*, **27**(8), pp. 1329–1331.
- [104] Deegan, R. D., Bakajin, O., Dupont, T. F., Huber, G., Nagel, S. R., and Witten, T. A., 1997, “Capillary Flow as the Cause of Ring Stains from Dried Liquid Drops,” *Nature*, **389**(6653), pp. 827–829.
- [105] Vanhecke, D., Petri-Fink, A., Rothe-Ruthishauser, B., Michen, B., and Balog, S., 2014, “Imaging & Microscopy.”
- [106] Gebhardt, J. C. M., Bornschlögl, T., and Rief, M., 2010, “Full Distance-Resolved Folding Energy Landscape of One Single Protein Molecule,” *Proc. Natl. Acad. Sci.*, **107**(5), pp. 2013–2018.
- [107] Dietz, H., and Rief, M., 2004, “Exploring the Energy Landscape of GFP by Single-Molecule Mechanical Experiments,” *Proc. Natl. Acad. Sci. U. S. A.*, **101**(46), pp. 16192–16197.
- [108] Bouvignies, G., Vallurupalli, P., Hansen, D. F., Correia, B. E., Lange, O., Bah, A., Vernon, R. M., Dahlquist, F. W., Baker, D., and Kay, L. E., 2011, “Solution Structure of a Minor and Transiently Formed State of a T4 Lysozyme Mutant,” *Nature*, **477**(7362), pp. 111–114.
- [109] Zang, X., Zhou, Q., Chang, J., Liu, Y., and Lin, L., 2014, “Graphene and Carbon Nanotube (CNT) in MEMS/NEMS Applications,” *Microelectron. Eng.*

- [110] Masduzzaman, M., and Alam, M. A., 2014, “Effective Nanometer Airgap of NEMS Devices Using Negative Capacitance of Ferroelectric Materials,” *Nano Lett.*
- [111] Eigenfeld, N. T., Gray, J. M., Brown, J. J., Skidmore, G. D., George, S. M., and Bright, V. M., 2014, “Ultra-Thin 3D Nano-Devices from Atomic Layer Deposition on Polyimide,” *Adv. Mater.*, **26**(23), pp. 3962–3967.
- [112] Seeman, N. C., 2010, “Nanomaterials Based on DNA.,” *Annu. Rev. Biochem.*, **79**, pp. 65–87.
- [113] Veneziano, R., Ratanalert, S., Zhang, K., Zhang, F., Yan, H., Chiu, W., and Bathe, M., 2016, “Designer Nanoscale DNA Assemblies Programmed from the Top down,” *Science*, p. 4388.
- [114] Marras, A. E., Zhou, L., Koliopoulos, V., Su, H.-J., and Castro, C. E., 2016, “Directing Folding Pathways for Multi-Component DNA Origami Nanostructures with Complex Topology,” *New J. Phys.*, **18**(5), p. 055005.
- [115] Su, H.-J., Castro, C. E., Marras, A. E., and Hudoba, M., 2012, “Design and Fabrication of DNA Origami Mechanisms and Machines,” *Advances in Reconfigurable Mechanisms and Robots I*, J.S. Dai, M. Zoppi, and X. Kong, eds., Springer London, pp. 487–500.
- [116] Bai, X., Martin, T. G., Scheres, S. H., and Dietz, H., 2012, “Cryo-EM Structure of a 3D DNA-Origami Object,” *Proc. Natl. Acad. Sci.*, **109**(49), pp. 20012–20017.
- [117] Zhang, L., Lei, D., Smith, J. M., Zhang, M., Tong, H., Zhang, X., Lu, Z., Liu, J., Alivisatos, A. P., and Ren, G., 2016, “Three-Dimensional Structural Dynamics and Fluctuations of DNA-Nanogold Conjugates by Individual-Particle Electron Tomography,” *Nat. Commun.*, **7**.
- [118] Ruf, A., Martin, F., Lamiroy, B., and Horaud, R., 2000, “Visual Servoing Using Projective Kinematics,” *ROBOTICS RESEARCH-INTERNATIONAL SYMPOSIUM-*, pp. 97–104.
- [119] Lang, R. J., 2003, *Origami Design Secrets: Mathematical Methods for an Ancient Art*, CRC Press.
- [120] Al-Mulla, T., and Buehler, M. J., 2015, “Origami: Folding Creases through Bending,” *Nat. Mater.*, **14**(4), pp. 366–368.
- [121] Chen, Y., Peng, R., and You, Z., 2015, “Origami of Thick Panels,” *Science*, **349**(6246), pp. 396–400.

- [122] Rogers, J., Huang, Y., Schmidt, O. G., and Gracias, D. H., 2016, “Origami MEMS and NEMS,” *MRS Bull.*, **41**(2), pp. 123–129.
- [123] Silverberg, J. L., Na, J.-H., Evans, A. A., Liu, B., Hull, T. C., Santangelo, C. D., Lang, R. J., Hayward, R. C., and Cohen, I., 2015, “Origami Structures with a Critical Transition to Bistability Arising from Hidden Degrees of Freedom,” *Nat. Mater.*, **14**(4), pp. 389–393.
- [124] Dudte, L. H., Vouga, E., Tachi, T., and Mahadevan, L., 2016, “Programming Curvature Using Origami Tessellations,” *Nat. Mater.*, **15**(5), pp. 583–588.
- [125] Felton, S., Tolley, M., Demaine, E., Rus, D., and Wood, R., 2014, “A Method for Building Self-Folding Machines,” *Science*, **345**(6197), pp. 644–646.
- [126] Miyashita, S., Guitron, S., Yoshida, K., Li, S., Damian, D. D., and Rus, D., 2016, “Ingestible, Controllable, and Degradable Origami Robot for Patching Stomach Wounds,” *2016 IEEE International Conference on Robotics and Automation (ICRA)*, pp. 909–916.
- [127] Zirbel, S. A., Lang, R. J., Thomson, M. W., Sigel, D. A., Walkemeyer, P. E., Trease, B. P., Magleby, S. P., and Howell, L. L., 2013, “Accommodating Thickness in Origami-Based Deployable Arrays¹,” *J. Mech. Des.*, **135**(11), pp. 111005–111005–11.
- [128] Bowen, L. A., Grames, C. L., Magleby, S. P., Howell, L. L., and Lang, R. J., 2013, “A Classification of Action Origami as Systems of Spherical Mechanisms,” *J. Mech. Des.*, **135**(11), p. 111008.
- [129] Bowen, L. A., Baxter, W. L., Magleby, S. P., and Howell, L. L., 2014, “A Position Analysis of Coupled Spherical Mechanisms Found in Action Origami,” *Mech. Mach. Theory*, **77**, pp. 13–24.
- [130] Funke, J. J., and Dietz, H., 2016, “Placing Molecules with Bohr Radius Resolution Using DNA Origami,” *Nat. Nanotechnol.*, **11**(1), pp. 47–52.
- [131] Ketterer, P., Willner, E. M., and Dietz, H., 2016, “Nanoscale Rotary Apparatus Formed from Tight-Fitting 3D DNA Components,” *Sci. Adv.*, **2**(2), p. e1501209.
- [132] Zhou, L., Su, H.-J., Marras, A. E., Huang, C.-M., and Castro, C. E., 2017, “Projection Kinematic Analysis of DNA Origami Mechanisms Based on a Two-Dimensional TEM Image,” *Mech. Mach. Theory*, **109**, pp. 22–38.
- [133] Yakovchuk, P., Protozanova, E., and Frank-Kamenetskii, M. D., 2006, “Base-Stacking and Base-Pairing Contributions into Thermal Stability of the DNA Double Helix,” *Nucleic Acids Res.*, **34**(2), pp. 564–574.

- [134] Macfarlane, R. J., Lee, B., Jones, M. R., Harris, N., Schatz, G. C., and Mirkin, C. A., 2011, "Nanoparticle Superlattice Engineering with DNA," *Science*, **334**(6053), pp. 204–208.
- [135] Zhang, Y., Pal, S., Srinivasan, B., Vo, T., Kumar, S., and Gang, O., 2015, "Selective Transformations between Nanoparticle Superlattices via the Reprogramming of DNA-Mediated Interactions," *Nat. Mater.*, **14**(8), pp. 840–847.
- [136] Overvelde, J. T. B., Weaver, J. C., Hoberman, C., and Bertoldi, K., 2017, "Rational Design of Reconfigurable Prismatic Architected Materials," *Nature*, **541**(7637), pp. 347–352.